Title

The Growth of Epitaxial Iron Oxides on Platinum(III) as Studied by X-Ray Photoelectron Diffraction, Scanning Tunneling Microscopy, and Low Energy Electron Diffraction

Author

Kim, Y.-J.

Publication Date

1995-05-01

LBL-37449
UC-401

Lawrence Berkeley Laboratory
UNIVERSITY OF CALIFORNIA

Materials Sciences Division

The Growth of Epitaxial Iron Oxides on Platinum (111) as Studied by X-Ray Photoelectron Diffraction, Scanning Tunneling Microscopy, and Low Energy Electron Diffraction

Y.-J. Kim
(Ph.D. Thesis)

May 1995

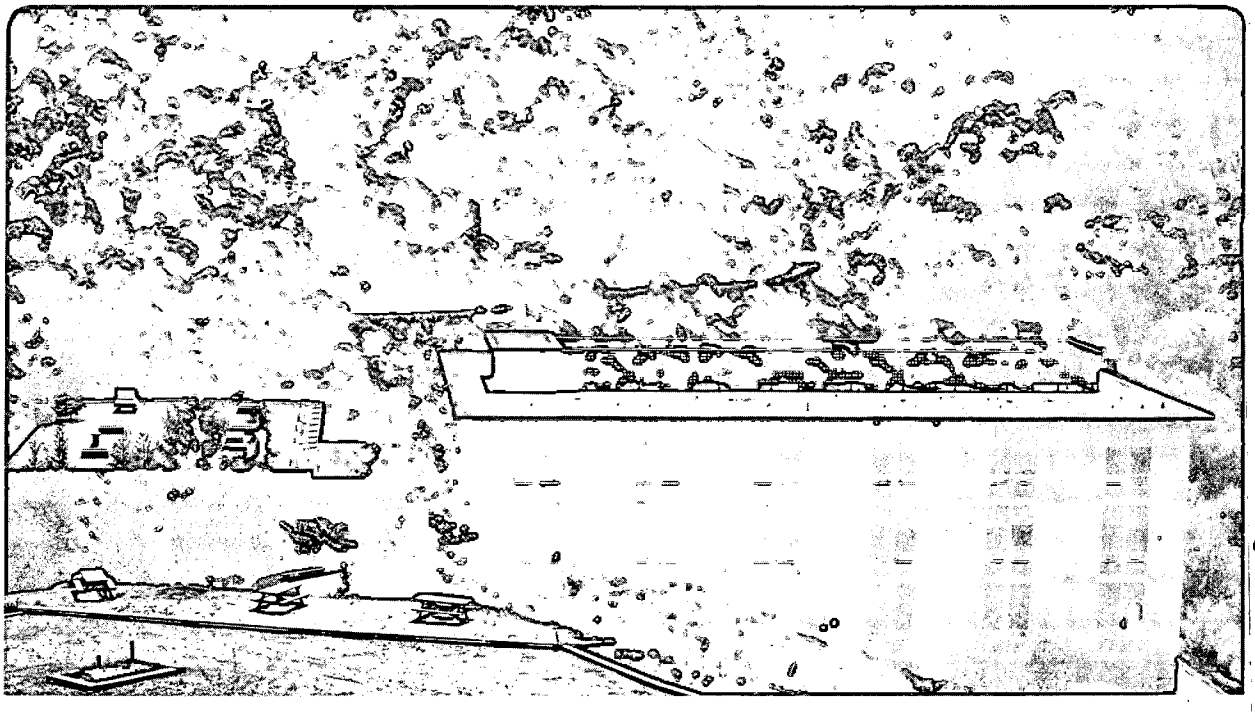

Prepared for the U.S. Department of Energy under Contract Number DE-AC03-76SF00098

DISCLAIMER

LBL-37449
UC-401

The Growth of Epitaxial Iron Oxides on Platinum (111) as Studied by X-Ray Photoelectron Diffraction, Scanning Tunneling Microscopy, and Low Energy Electron Diffraction

Yong-Joo Kim
Ph.D. Thesis

Department of Chemistry
University of Hawaii

and

Materials Sciences Division
Lawrence Berkeley Laboratory
University of California
Berkeley, CA 94720

May 1995

This work was supported in part by the Director, Basic Energy Sciences, Materials Sciences Division, of the U.S. Department of Energy under Contract No. DE-AC03-76SF00098, and by the Office of Naval Research under Contract Nos. N00014-90-5-1457 and N00014-94-1-0162.

LBL-37449

THE GROWTH OF EPITAXIAL IRON OXIDES ON PLATINUM (111) AS STUDIED BY X-RAY PHOTOELECTRON DIFFRACTION, SCANNING TUNNELING MICROSCOPY, AND LOW ENERGY ELECTRON DIFFRACTION

A DISSERTATION SUBMITTED TO THE GRADUATE DIVISION OF THE UNIVERSITY OF HAWAII IN PARTIAL FULFILLMENT OF THE REQUIREMENTS FOR THE DEGREE OF

DOCTOR OF PHILOSOPHY

IN

CHEMISTRY

MAY 1995

By

Yong-Joo Kim

Dissertation Committee:

Charles S. Fadley, Chairperson
George Andermann
Thomas T. Bopp
John D. Head
Klaus D. Sattler

DEDICATION

I dedicate this dissertation to my wife E. H. Park for her love and endurance.

ACKNOWLEDGMENTS

I would like to thank Professor Charles S. Fadley for his valuable advice, guidance, and support over the years. Without his ingenuity in looking ahead of the research projects and his valuable suggestions in data analysis, none of this work would have been possible. I also thank Dr. Kazuyuki Higashiyama and Dr. Carsten Westphal for their valuable assistance in bringing the VG ESCALAB5 spectrometer up to its present excellent working condition after it was moved from Hawaii, and also in incorporating the STM/LEED chamber to the existing spectrometer; Mr. Robert Wright for his assistance with precise machining; Dr. Ajith P. Kaduwela for his assistance in theoretical simulations of experimental data and for late-night drinking sessions; Mr. Ramon X. Ynzunza for his assistance with data analysis; members of the Fadley group for being helpful, understanding, and accommodating; Dr. Michel A. Van Hove for his critically reading of this dissertation and for valuable suggestions throughout this project; Ms. Heather C. Galloway and Dr. Miquel Salmeron for their help with STM and valuable discussions; the Department of Chemistry, University of Hawaii-Manoa for letting me have the opportunity to continue my graduate work with Professor Charles S. Fadley at the Lawrence Berkeley Laboratory.

This work was supported by the Department of Energy, Basic Energy Sciences, Materials Sciences Division (Contract No. DOE-AC03-76SF00098), by the Office of Naval Research (Contract Nos. N00014-90-5-1457 and N00014-94-1-0162), and by the National Energy Research Supercomputing Center.

ABSTRACT

For the first time, three complementary surface structure probes, x-ray photoelectron diffraction (XPD), scanning tunneling microscopy (STM), and low-energy electron diffraction (LEED) have been combined in a single instrument. This experimental system has been utilized to study the structure and growth mechanisms of iron oxide films on Pt(111); these films were formed by first depositing a single overlayer of Fe with a certain coverage in monolayers (ML's), and then thermally oxidizing it in an oxygen atmosphere. For films up to ~1 ML in thickness, a bilayer of Fe and O similar to those in FeO(111) is found to form. In agreement with prior studies, STM and LEED show this to be an incommensurate oxide film forming a lateral superlattice with short- and long-range periodicities of ~3.1 Å and ~26.0 Å. XPD in addition shows a topmost oxygen layer to be relaxed inward by ~0.6 Å compared to bulk FeO(111) , and these are new structural conclusions. The oxygen stacking in the FeO(111) bilayer is dominated by one of two possible binding sites. For thicker iron oxide films from 1.25 ML to 3.0 ML, the growth mode is essentially Stranski-Krastanov: iron oxide islands form on top of the FeO(111) bilayer mentioned above. For iron oxide films of 3.0 ML thickness, x-ray photoelectron spectroscopy (XPS) yields an Fe $2p_{3/2}$ binding energy and an Fe:O stoichiometry consistent with the presence of Fe_3O_4. Our XPD data further prove this overlayer to be Fe_3O_4(111)-magnetite in two almost equally populated domains with a 180° rotation between them. The structural parameters for this Fe_3O_4 overlayer generally agree with those of a previous LEED study, except that we find a significant difference in the first Fe-O interplanar spacing. Overall, this work demonstrates the considerable benefits to be derived by using this set of complementary surface structure probes in such epitaxial growth studies.

TABLE OF CONTENTS

LIST OF TABLES

LIST OF FIGURES

LIST OF ACRONYMS

BE	binding energy
FvM	Frank-van der Merwe
HOPG	highly-oriented pyrolytic graphite
LEED	low energy electron diffraction
ML	monolayer
MS	multiple scattering
MSC	multiple scattering cluster
PD	photoelectron diffraction
QCM	quartz-crystal microbalance
SK	Stranski-Krastanov
SS	single scattering
SSC	single scattering cluster
STM	scanning tunneling microscopy
XPD	x-ray photoelectron diffraction
XPS	x-ray photoelectron spectroscopy
UHV	ultrahigh vacuum
VW	Vollmer-Weber

CHAPTER 1

GENERAL INTRODUCTION

A knowledge of the atomic identities, positions, and bonding mechanisms within the first 3-5 layers of a surface is essential to any quantitative microscopic understanding of surface phenomena, including such technologically important processes as catalytic activity; oxidation and corrosion; adhesion, and overlayer and nanostructure formation in the production of integrated circuits, magnetic storage devices, and other nanoscale devices. This implies knowing bond directions, bond distances, site symmetries, coordination numbers, and the degree of both short- and long- range order present in the "selvedge" region between the true bulk of a material and its surface. A number of surface structure probes have thus been developed in recent years in an attempt to provide this information [1]. Each of these methods has certain unique advantages and disadvantages, and they are often complementary to one another.

In this dissertation, a particularly powerful set of three complementary surface structure probes have, for the first time, been combined in the same experimental instrument and applied to the important general problem of the epitaxial growth of a metal oxide on another metal as substrate. These three methods are: x-ray photoelectron diffraction (XPD), scanning tunneling microscopy (STM), and low-energy electron diffraction (LEED). Fig. 1.1 shows schematic illustrations of the three techniques with the complementary information they provide. In order to illustrate this complementarity, brief descriptions of each technique and its method of theoretical interpretation will be presented.

X-Ray Photoelectron Spectroscopy (XPS) and X-Ray Photoelectron Diffraction (XPD):

In the photoemission process, electrons can be emitted from a sample into the vacuum if radiation of high enough energy is adsorbed by the sample. As first explained by Einstein [2], the photoelectric equation describing energy conservation is,

$E_{kin} = h\nu - E_b^v(i)$,

where E_{kin} is the kinetic energy of the photo-emitted electron, $h\nu$ is the exciting photon energy, and $E_b^v(i)$ is the binding energy of an electron emitted from the i^{th} level as referenced to the vacuum level. In x-ray photoelectron spectroscopy (XPS), soft x-ray radiation is used as the excitation source; for all work reported here the radiation is Al K $\alpha_{1,2}$ from a standard x-ray tube at an energy of 1486.7 eV. These photo-emitted electrons, termed photoelectrons, can come from core or valence levels, but only core level excitations will be considered in this dissertation. Core photoelectron intensities can be used for the quantitative analysis of surface compositions, and we will make use of this aspect of XPS, as described in more detail in Appendix A. A typical experimental geometry with important angular variables is shown in Fig. 1.2. In our experiments, the angle α between photon and electron will be held fixed, and the principle variables will be the direction of electron emission, as given by the polar angle or electron takeoff angle θ (measured with respect to the surface) and the azimuthal angle ϕ (measured with respect to some reference direction in the crystal). The electron binding energies $E_b^v(i)$ can in first approximation be considered as one-electron energy levels for the core shells, provided we neglect corrections for relaxation and other final-state effects. The chemical environment can also cause shifts in the binding energies of the core level electrons and these shifts are termed chemical shifts; we will also make use of these to determine the chemical states of metal atoms in epitaxial oxides.

In x-ray photoelectron diffraction (XPD), a photoelectron is emitted from a core level, and its intensity is measured as a function of its direction or its energy above a single-crystal sample, yielding what can be termed scanned-angle XPD or scanned-energy XPD, respectively. All data in this dissertation are obtained in the scanned-angle mode, with intensities being measured over essentially the full 2π steradians above the sample surface by varying the two electron emission angles: the polar angle θ and the azimuthal angle ϕ. In addition, the measured intensity distribution in direction $I(\theta,\phi)$ was converted to a normalized intensity modulation or chi function $\chi(\theta,\phi)$ for display and analysis. This function is defined in Chapter 3. An important aspect of the core-level excitation is that the measurement is atom-specific: that is, emitters of each atomic number in the sample can be studied separately. Also, both XPS and XPD have high surface sensitivity because the elastically emitted electrons in a given spectral peak have a limited distance they can travel through the bulk before they are inelastically scattered out of the peak [3]. The inelastic scattering length associated with this process is found to be very dependent upon the kinetic energy of the photoelectron, as shown in Fig. 1.3. As will be illustrated in later theoretical considerations of XPD, this technique is a short-range probe of the local environment around a given type of emitter since it is primarily sensitive to the first three to five spheres of neighbors around each emitter.

Photoelectron diffraction (PD) patterns excited by both soft x-rays and lower-energy synchrotron radiation are by now well known and much studied, and have lead to the increasing use of this technique for surface structure studies. Simple single-scattering cluster (SSC) and more complex multiple-scattering cluster (MSC) calculations can be used to determine the surface atomic structure by comparing experiment to calculations for various structures and determining the best fit. The basic process involved in photoelectron diffraction and the important physical variables are indicated in Fig. 1.4. The intensity modulations of the emitted photoelectron with direction are produced by

the interference of the unscattered or direct wave component ϕ_o and the various scattered-wave components ϕ_j. The resulting photoelectron intensity as a function of wave vector can be written in a simple single scattering picture as [4]:

$$I(\vec{k}) \propto \left|\phi_o + \Sigma_j \phi_j\right|^2 \\ \propto \left|\phi_o\right|^2 + \Sigma_j(\phi_o{}^* \phi_j + \phi_o \phi_j{}^*) + \Sigma_j \Sigma_k \phi_j \phi_k{}^* \qquad (1)$$

where ϕ_j and ϕ_k are arbitrary scattered waves. For the illustrative case of photoelectron emission from an s subshell into an outgoing ϕ_o with p character, the individual wave components here can be written out more explicitly in terms of: dipole matrix elements that are for linearly polarized radiation proportional to the dot product of the polarization direction ($\hat{\varepsilon}$) and the relevant emission direction ($\hat{k}$ or $\vec{r}_j / r_j = \hat{r}_j$); inelastic exponential decay factors $\exp(-L/\Lambda_e)$, with L equal to the total length for some path below the surface and Λ_e equal to the inelastic attenuation length for photoelectron intensity; scattering factors $f_j(\theta_j,r_j)$ involving both an amplitude $|f_j(\theta_j,r_j)|$ and a phase shift $\Psi_j(\theta_j,r_j)$ that are functions of the scattering angle θ_j, and, in more accurate spherical-wave scattering, also of the distance r_j to a given scatter; Debye-Waller factors W_j that allow for attenuation of interference due to vibrational effects; and finally, phase shifts due to path length differences of the form $\exp(ikr_j)\exp(-i\vec{k} \cdot \vec{r}_j) = \exp[ikr_j(1-\cos\theta_j)]$. All structural information is contained in this last exponential factor, with the path length difference between ϕ_o and ϕ_j being given by $r_j(1-\cos\theta_j)$. Eq. (1) can for this special case then be rewritten as:

$$I(\vec{k}) = \Big| (\hat{\varepsilon} \cdot \hat{k}) \exp(-L_o / 2\Lambda_e) + \Sigma_j (\hat{\varepsilon} \cdot \hat{r}_j / r_j) \left|f_j(\theta_j,r_j)\right| W_j \cdot \\ \exp(-L_j / 2\Lambda_e) \exp[i\{kr_j(1-\cos\theta_j) + \Psi j(\theta_j,r_j)\}]\Big|^2 \qquad (2)$$

For emission from a subshell other than s (i.e. for $l_{initial} > 0$), the above expressions become more complex due to sums over initial and final magnetic quantum numbers and interference between the two final-state channels $l_{final} = l+1$ and $l-1$ that are allowed by the dipole selection rules [5].

Complete reviews of photoelectron diffraction including descriptions of the detailed photoemission process and experimental as well as theoretical aspects within a more complex multiple scattering picture can be found elsewhere [4,6]. We note here two additional important aspects of this technique that will be used in qualitative and quantitative ways in the analysis of our data: the importance of forward scattering and the dominance of short-range-order. In measurements at photoelectron kinetic energies of about 500 eV or higher that will be relevant to this dissertation, the scattering amplitude $|f_j(\theta_j,r_j)|$ is highly peaked in the forward direction (i.e. near $\theta_j = 0$). In order to illustrate this strong forward scattering, the kinetic energy dependence of atomic scattering factors for plane-wave scattering from atomic Ni are shown in Fig. 1.5 [7]. It is clear that for the highest energies of 505 eV and 1320 eV, strong scattering occurs only along the forward direction. Many studies have shown that such forward scattering or forward focusing peaks can be directly used to determine bond directions for adsorbed molecules or near-neighbor scattering directions in crystals and epitaxial overlayers (the use we will make of it) [4,8]. The second important aspect is that XPD is inherently a short-range order probe because all the waves in Eq. (1) die away rapidly from the emitter. This is because the direct wave has a limiting spherical-wave form [e.g., $\phi_o \propto \exp(ikr)/r$], so that the portion of ϕ_o which passes to the scatterer j to produce ϕ_j decays in amplitude as $1/r_j$. This decay is a principal reason why XPD is a short-range order probe, although the effects of inelastic scattering contribute additionally to this, as shown by the exponentials in Eq. (2).

In order to analyze the experimental XPD data for this dissertation, we have used both single-scattering and multiple-scattering codes developed by Friedman et al. [10] and Kaduwela et al. [11], respectively. These codes make use of the short-range-order sensitivity of XPD by including scatterers in only a finite cluster around the emitter, with the cluster being chosen to include all important scatterers, especially in the forward direction; they can thus be termed SSC and MSC methods, respectively. These programs are based upon a new separable-Green's-function matrix method due to Rehr and Albers [12], in which multiple scattering was included up to the tenth order. These codes automatically incorporate both the forward scattering peaks and all other interference and attenuation effects, including all the physical variables discussed above. They also incorporate the correct spherical nature of the final state photoelectron waves, as well as various angular momenta and interferences involved because of the dipole transition from the initial angular momentum state to the final angular momentum states. Furthermore, the codes also included several additional effects such as instrumental angular averaging, the possible use of either polarized or unpolarized radiation, and refraction of the photoelectrons at the surface due to the inner potential V_0 (a minor effect for all but the lowest electron takeoff angles considered in this work). Further details on the parameters used for the SS and MS calculations are included in the relevant chapters of this dissertation.

Scanning Tunneling Microscopy:

Since its introduction by Binnig and Rohrer in 1982 [13], scanning tunneling microscopy (STM) has become a widely used technique in surface studies. Several reviews of this technique including descriptions of the electron tunneling process and experimental as well as theoretical aspects can be found elsewhere [14]. The basic idea

is that a sharp tip is brought close enough to the surface that, at a convenient operating bias voltage in the approximate range of ±2 mV to ±2V, a tunneling current is measurable. The tip is scanned over/across a surface while the current *I* between the tip and the surface, is sensed. The tunneling current varies exponentially with the gap between the tip and the surface, with a simple expression for this variation being

$I \propto \exp(-2\kappa d)$

where *I* is the current, *d* is the distance between electrodes, and κ is the decay constant for the wave functions in the barrier. In this case of vacuum tunneling, κ is related to the effective local work function ϕ by

$\kappa = \hbar^{-1}\sqrt{2m\phi}$

where m is the electron mass. This current is thus extremely sensitive to the height of the tip above the surface: for a typical barrier potential of 4 eV, a change in tip distance of 1 Å leads to a change in current by a factor of ten. At least two different modes of operation of the STM are possible, and both have been used in this work. In the constant current mode, a feedback network changes the height (z) of the tip using precise piezoelectric control so as to keep the current constant while the tip is scanned over a surface (in x and y); this keeps the tip at a nearly constant height. Calibrating the piezoelectric drivers so as to be able to finally plot the tip height versus the scan position in x and y can then reveal three-dimensional pictures of surfaces at atomic resolution. In the constant height mode, a tip can be scanned across a surface at nearly constant height (z) and constant voltage while the current is monitored. In this case the feedback network responds only rapidly enough to keep the average current constant. Plotting the rapid variations in current due to the tip passing over surface features versus the scan position in x and y also reveals three-dimensional pictures of surfaces at atomic resolution. Both types of three-dimensional STM images provide local real space information that can be at atomic resolution, thus probing both short- and long- range

order, as well as disorder and defects, in the top-most surface layers(s). STM is also primarily sensitive to the outermost surface topography (via the surface density of states that is responsible for electron tunneling).

Low Energy Electron Diffraction:

Low-Energy Electron Diffraction (LEED) can reasonably claim to be the oldest of modern surface techniques, as the first LEED experiment by Davisson and Germer in 1927 [15] also provided the first demonstration of the wave nature of the electron. Complete reviews of this technique including descriptions of the experimental and theoretical aspects can be found elsewhere [16]. The basic process involves impinging an electron beam, typically in the 20 - 300 eV energy range, on the surface and observing the diffraction pattern produced by the elastically scattered and diffracted electrons. Both the very short inelastic mean-free-path Λ_e and the strong backscattering in this energy range (cf. Fig. 1.5) make LEED primarily sensitive to the first few layers of a surface. Because the various surface atom periodicities act as diffraction gratings in the LEED experiment, the most intense diffraction spots in a LEED pattern probe long-range two-dimensional order in these first few layers. More precisely, the condition for Bragg reflection can be written as [16]

$$\mathbf{k'}_{||} = \mathbf{k}_{||} + \mathbf{g}_{hk}$$

with

$$\mathbf{g}_{hk} = h\mathbf{a}^* + k\mathbf{b}^*$$

and

$$\mathbf{a}^* = 2\pi\frac{\mathbf{b}\times\mathbf{n}}{A}\ ,\ \mathbf{b}^* = 2\pi\frac{\mathbf{n}\times\mathbf{a}}{A}\ ,\ A = \mathbf{a}\cdot\mathbf{b}\times\mathbf{n}$$

where **a*** and **b*** are the primitive translation vectors of the reciprocal lattice related to those of the real lattice a, b, **n** is a unit vector normal to the surface, $\mathbf{g}_{hk}$ is a reciprocal lattice vector, and $\mathbf{k}_{||}$ and $\mathbf{k'}_{||}$ are the incident and emerging wave vectors parallel to the surface, respectively. Thus, the LEED pattern will consist of a pattern of spots, each of which can be associated with one of the reciprocal lattice vectors $\mathbf{g}_{hk}$ describing the periodicity of the surface.

The most common way of using LEED patterns in surface science is to record them at a few energies, and analyze the dominant spots or satellites in terms of various possible structures with long-range order. Spot fuzziness or streaking also may be used to detect disorder or limited long-range order. Also, the intensities of different spots can be measured as a function of energy, and these so-called I-V curves then compared to multiple-scattering theory for different possible atomic structures so as to finally yield a best estimate for a given structure. Many surface structures have been determined in this way to date. Beyond this, the detailed profile of the diffraction spots, or the diffuse background between them, can be used to derive information on shorter-range order. In general then, LEED is first a probe of long-range order, but it can be extended to yield information on shorter-range order.

We finally summarize the complementarity of the three surface structure probes used in this thesis: XPD is a near-surface probe of the short- range order in the first 3-5 shells of neighbors around each emitter. STM probes both short- and long- range order, as well as disorder of the top-most surface layers(s), and is primarily sensitive to the outermost surface topography. In this dissertation, only LEED spot patterns at a few energies are interpreted and no current versus voltage curves are measured. Thus for present purposes, LEED is primarily sensitive to long-range two-dimensional order, with a probing depth that is comparable to or somewhat shorter than that of XPD. XPD is atom-specific, as each core level studied is characteristic of a given atomic number,

while STM and LEED are not. Taken together, these methods will thus provide us with a broad and powerful set of information concerning a surface structure, as will become evident in our actual application of them to iron oxide growth on Pt(111) in Chapters 3 and 4.

Instrumentation Development:

Unique instrumentation combining these three techniques has been developed as part of this dissertation, and this will be described in Chapter 2 in detail. This work includes building a new custom-designed long-travel two-axis sample goniometer and designing and building a new sample holder so that the sample can be transferred from one technique to another by means of a specially-modified wobble stick. An additional chamber for LEED, STM, and sample preparation was also added to an existing XPD system. Experimental details including the sample preparation are also presented in Chapter 2.

Application to iron oxide epitaxy on the platinum (111) surface:

This new experimental system has been utilized to study the structure and growth mechanisms of iron oxide films on the (111) surface of single-crystal platinum. The metal oxides constitute a diverse and fascinating class of materials whose properties cover the entire range from metals to semiconductors and insulators. There is an increasing interest in the surface properties of metal oxides, because of their important and varied technological applications [17]. The metal oxides themselves are catalysts for a variety of commercially important reactions, and reducible transition-metal oxides are also used as supporting materials for metal catalysts, for which strong interactions

between the metal and the support can occur that significantly alter the catalytic behavior of the metal [18]. Other important applications of metal oxides are in gas sensors [19] and metal-ceramic bonding for corrosion resistance in high-temperature materials [20]. Furthermore, the magnetic properties of the different oxides of iron are utilized in high-density magnetic recording media [21]. Finally, the transition-metal oxides are an essential ingredient of high-temperature superconductors, an exciting new class of materials that is still poorly understood [17].

For all of their technological importance, the surfaces of metal oxides have not been studied as extensively as those of metal single crystals. Metal oxide single crystals are difficult to obtain with reproducible composition because of their chemical complexity, and this is especially true for transition metal oxides with several oxidation states available to them. Also, the preparation of nearly perfect surfaces of metal oxides is difficult compared to surfaces of elemental solids since the geometric order, as well as the stoichiometry, of the surface can be different from that of the bulk. In addition, the insulating properties of many oxides often make surface characterization difficult using electron-based techniques such as the various electron spectroscopies and STM. However, in some cases, including the iron-oxide/Pt system, the oxide overlayer has been found to grow in an ordered manner [22-25]. Provided that the oxide is not too thick, these systems thus permit studying epitaxial growth using the full array of surface structure probes, since surface conductivities have been found to be sufficient to permit using electron-based probes. These systems thus provide the opportunity for studying oxide epitaxial growth in detail, and we have here chosen to focus on ultra-thin films of iron oxide in average thickness from 0.75 monolayers (ML) to 3.0 ML of Fe as grown on Pt(111).

The iron-oxide/Pt(111) system also has the advantage that it has been studied previously using two of the three techniques to be employed here (STM and LEED in

two separate studies [23-25]), but several important structural questions remained after these studies that it proves possible to answer via the complementarity of our new instrument combining XPD, STM, and LEED. We conclude this introduction by reviewing some of the prior work on this system, and indicating generally what new data we have obtained for it. The first monolayer of iron oxide on Pt(111) has been suggested to grow as a bilayer of Fe and O like that in bulk FeO with the (111) surface exposed. The first observation of an ordered overlayer was made by Vurens et al. in simultaneously applying LEED and ion scattering spectroscopy (ISS), and this led to the proposal of a (111)-type FeO bilayer forming a (10x10) coincidence lattice or lateral superlattice on the Pt(111) substrate [23]. However, these studies did not permit concluding the relative positions of the Fe and O atoms, or in particular whether Fe or O atoms or both occupied surface positions, with the ISS data showing both Fe and O peaks in spite of its high surface sensitivity. A subsequent STM study by Galloway et al. [24] concluded that an incommensurate overlayer or superlattice forms for which the short overlayer periodicity of 3.1 Å in (111)-type FeO is modulated by a large periodicity of ~26 Å that is linked to a more complex superelattice Moiré pattern formed between FeO and Pt (to be discussed in detail below). However, there are still open questions to be answered such as the detailed three-dimensional structure of this first monolayer of iron oxide; these questions cannot be answered by STM, since it is not atom-specific and does not look below the surface layer, nor by LEED, since the unit cell of the superlattice is too large to be modeled quantitatively and an I-V analysis prohibitively difficult at the present time. To address this structure, we have studied two coverages of iron oxide films: 0.75 and 1.0 ML. Our combined XPD, STM, and LEED permits deriving for the first time a detailed three-dimensional atomic picture of this iron-oxide monolayer. The Fe:O stoichiometry for both coverages is found to be very close to 1:1 by XPS quantitative analyses. Our LEED patterns and STM images

well reproduce those of earlier studies, including atomically resolved STM images showing both the short and long periodicities, and verify the correct preparation of the overlayers. Furthermore, core-level XPD patterns for Pt, Fe, and O excitation over essentially the full 2π solid angle above the surface were measured. These XPD experimental results, when compared to single scattering cluster (SSC) calculations, permitted concluding that oxygen is indeed the topmost or terminating atomic layer, that this layer also is relaxed significantly inward by 0.6 Å compared to bulk FeO(111), and that the stacking of the topmost O atoms with respect to the underlying Pt is dominated by one of two structurally very similar possibilities.

For thicker oxide layers corresponding to more than one monolayer of iron on Pt(111), the most relevant prior studies are the recent work by Weiss and co-workers using LEED [25] and by Galloway et al. with STM [24]. These studies taken together permitted concluding that $Fe_3O_4(111)$, as magnetite, can be grown by repeating the monolayer iron oxide growth several times in an oxygen pressure of approximately $5x10^{-5}$ Torr. A further structural detail suggested on the basis of the LEED I-V analysis is that there is an outermost 1/4 ML of Fe terminating the surface. The STM study also indicates that α-$Fe_2O_3(0001)$ can be obtained by growing the oxide at a much higher oxygen pressure ($\approx$ $5x10^{-4}$ Torr). Furthermore, large relaxations in the vertical interlayer spacings of the Fe_3O_4 films compared to bulk $Fe_3O_4(111)$ were also reported in the LEED study, while STM showed the growth mode to be of Stranski-Krastanov type: 3D islands growing on a base monolayer that is in some sort of regular registry with the substrate. We have thus also studied thicker iron oxide films from 1.25 ML to 3.0 ML with our combined techniques in order to better understand the growth mechanism and the internal atomic structures involved. Our STM and XPD data permit concluding that the growth mode of these oxides on Pt(111) is indeed Stranski-Krastanov, at least when grown in a slightly different way from the one-shot oxidation

of a single Fe layer of a given thickness. The first layer in between, and perhaps also underlying, the islands is also found to be the 1 ML FeO lateral superlattice seen at lower coverages. And for the thickest iron oxide (3.0 ML), the Fe:O stoichiometry and Fe $2p_{3/2}$ binding energy as derived from XPS are found to be very close to those expected for Fe_3O_4. XPD also shows for this 3.0 ML film that the internal atomic structure is $Fe_3O_4(111)$ with significant interlayer relaxation and in two types of structural domains that are almost equally populated on the surface. Our results also yield one Fe-O interlayer spacing that is significantly different from a model based on the LEED I-V analysis [25].

The outline of the following chapters is as follows: In Chapter 2, we describe the unique instrumentation that was designed and constructed, as well as certain experimental procedures, including the oxide growth method. Chapter 3 considers our results for oxide coverages up to 1.0 ML. Chapter 4 deals with thicker oxide coverages from 1.25 ML to 3.0 ML. Finally, Chapter 5 presents specific conclusions concerning the iron-oxide/Pt(111) system, some more general remarks concerning the utility of the newly developed instrument combining XPD, STM, and LEED, and some suggestions as to future directions and possible extensions of the work presented in this dissertation. The Appendices contain various details concerning the analysis of our data.

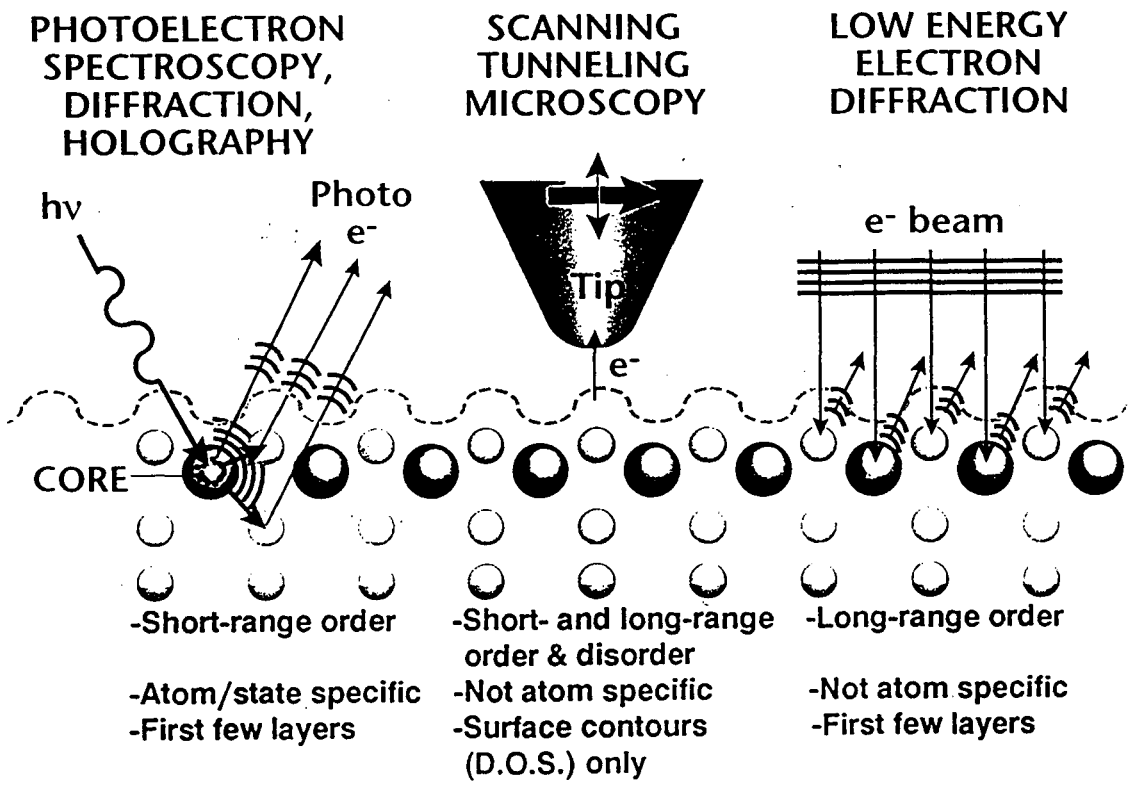

Figure 1.1. A schematic indication of the measurements involved in x-ray photoelectron spectroscopy (XPS) and x-ray photoelectron diffraction (XPD), scanning tunneling microscopy (STM), and low energy electron diffraction (LEED), including the complementary information provided by each technique.

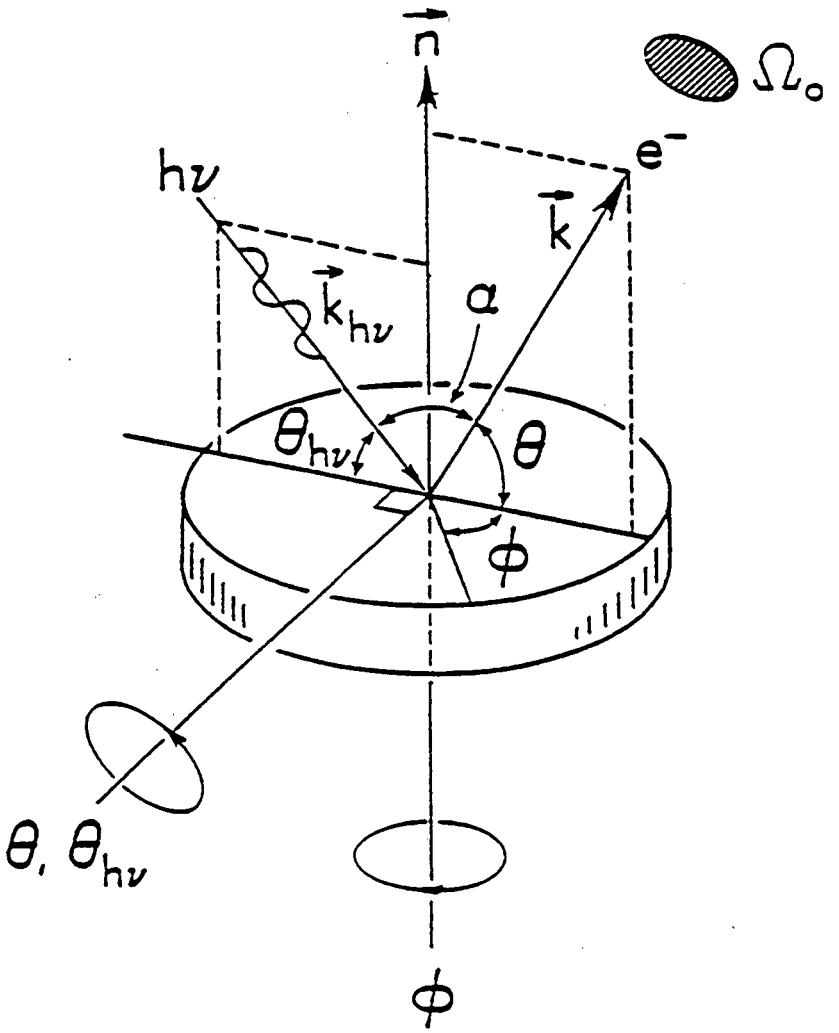

Figure 1.2. Illustration of the basic experimental geometry in the XPD experiment. The polar angle θ of electron emission is measured from the surface. The angle α between the incoming radiation and the outgoing wave vector was fixed in our experiments at 48°.

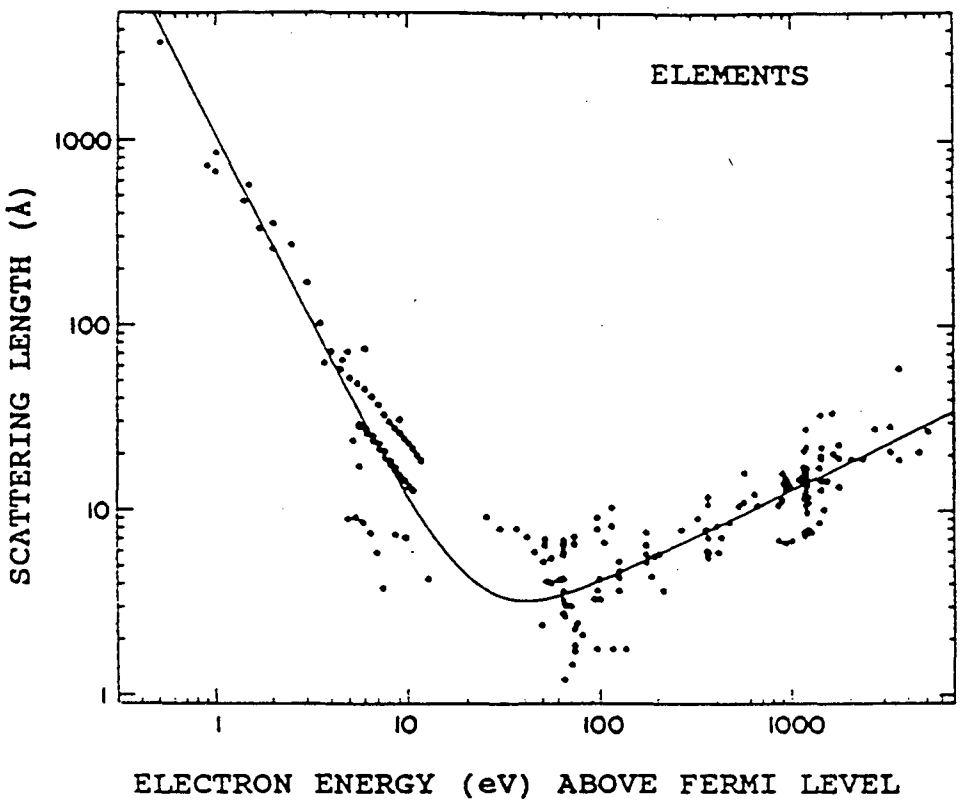

Figure 1.3. Compilation of inelastic attenuation lengths Λ_e for various solid elements. The solid line is the so-called "universal' curve. [From ref. 3.]

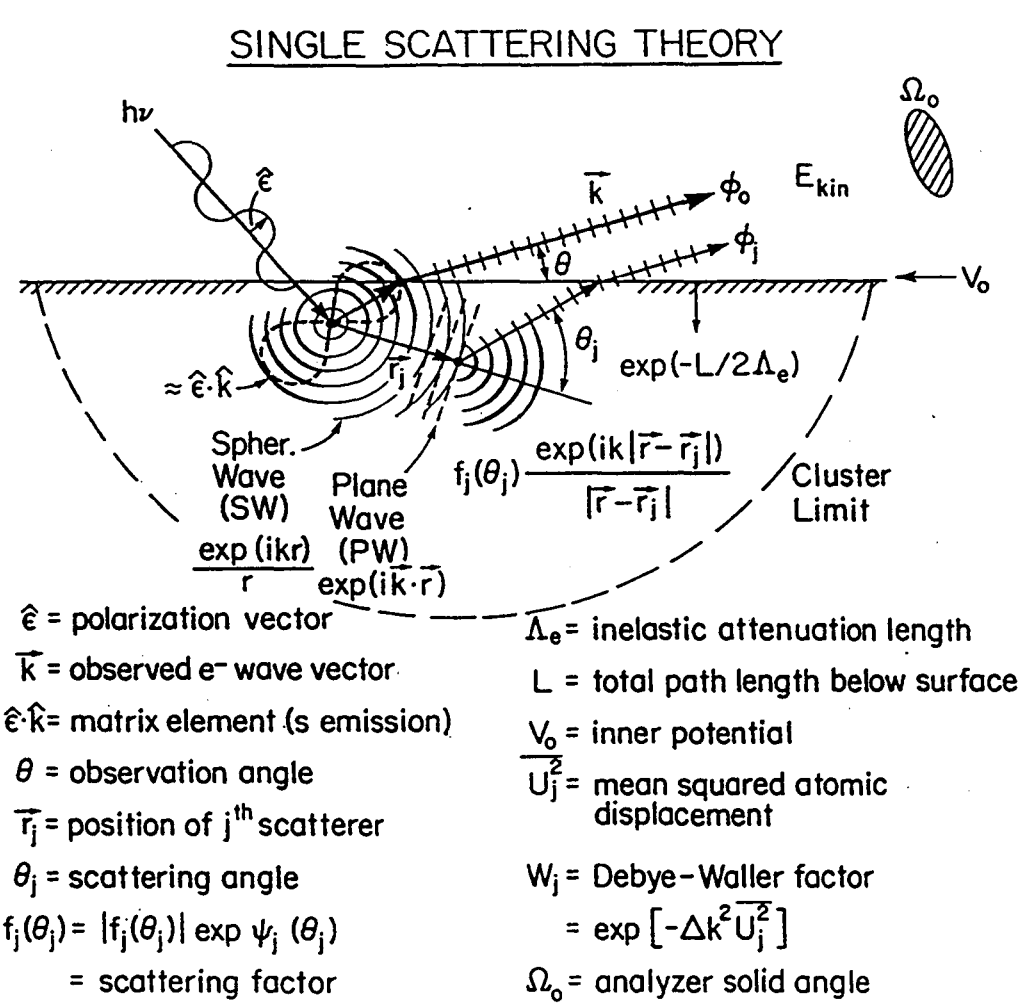

Figure 1.4. The basic process involved in photoelectron diffraction, with important physical variables indicated. Only single scattering is shown for simplicity.

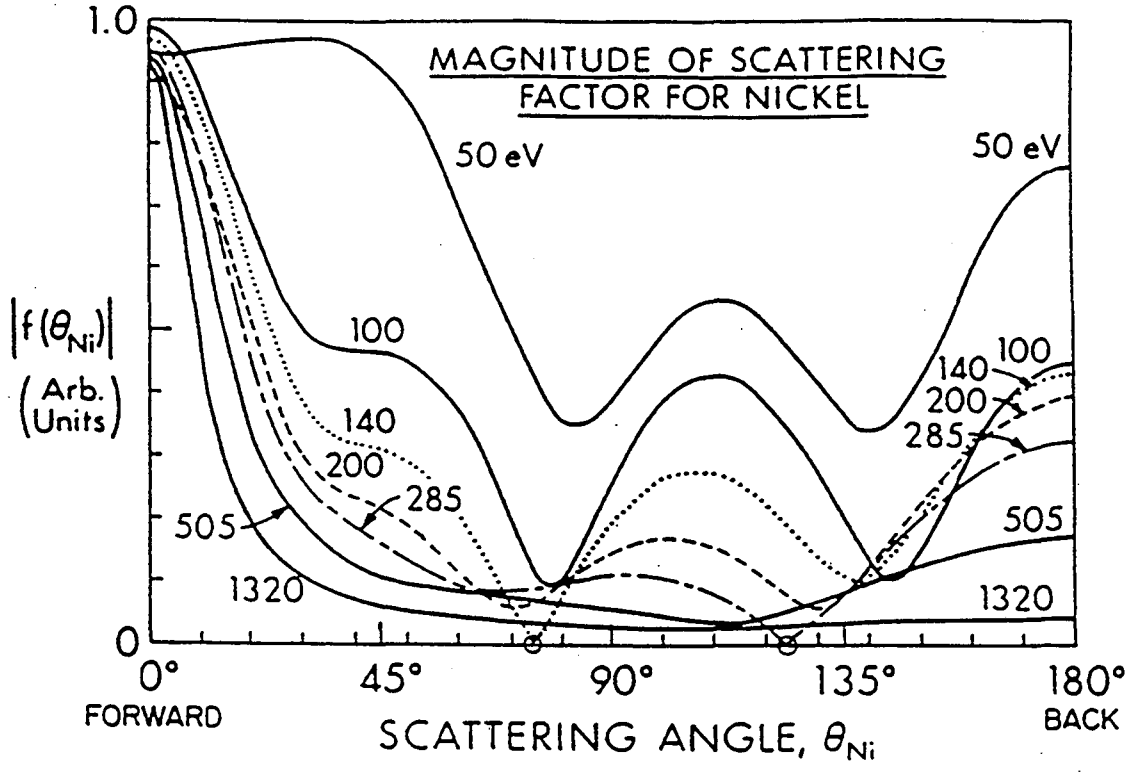

Figure 1.5. Nickel plane-wave scattering factor amplitudes $|f_{Ni}|$ as a function of both scattering angle θ_{Ni} and the photoelectron kinetic energy. [From ref. 7.]

REFERENCES

[1] Excellent summaries of the current status of most of these techniques can be found in the proceedings of two previous International Conferences on Structure of Surfaces: (a) The Structure of Surfaces II (J.F. van der Veen and M.A. van Hove, eds.), Springer Verlag, Berlin (1988); (b) The Structure of Surfaces III (S.Y. Tong, M.A. Van Hove, K. Takayanagi, and X.D. Xie, eds.), Springer-Verlag, Berlin (1991); (c) The Structure of Surfaces IV (X.D. Xie, K. Takayanagi, S.Y. Tong, and M.A. Van Hove, eds.), World Sci., Singapore (1994)

[2] A. Einstein, Ann. Physik 17, 132 (1905)

[3] M.P. Seah and W.A. Dench, Surf. and Interface Anal. 1, 2 (1979)

[4] C.S. Fadley in Electron Spectroscopy: Theory, Techniques, and Applications, C.R. Brundle and A.D. Baker, Eds., Vol. II, Chap.1 (Academic Press, London) (1978); C.S. Fadley, Prog. Surf. Sci. 16, 275 (1984); C.S. Fadley, Physica Script T17, 39 (1987); C.S. Fadley in Synchrotron Radiation Research: Advances in Surface Science, R.Z. Bachrach, Ed. (Plenum, New York) (1992)

[5] C.H. Li and S.Y. Tong, Phys. Rev. Lett. 42, 901 (1979); D.J. Friedman and C.S. Fadley, J. Electron Spectrosc. and Relat. Phenom. 51, 689 (1990); A.P. Kaduwela, D.J. Friedman, and C.S. Fadley, J. Electron Spectrosc. and Relat. Phenom. 57, 223 (1991)

[6] C.S. Fadley in Electron Spectroscopy: Theory, Techniques, and Applications, C.R. Brundle and A.D. Baker, Eds., Vol. II, Chap.1 (Academic Press, London) (1978); C.S. Fadley, Prog. Surf. Sci. 16, 275 (1984); C.S. Fadley, Physica Script T17, 39 (1987); C.S. Fadley in Synchrotron Radiation Research: Advances in Surface Science, R.Z. Bachrach, Ed. (Plenum, New York) (1992), C.S. Fadley, S. Thevuthasan, A.P. Kaduwela, C. Westphal, Y.J. Kim, R. Ynzunza, P. Len, E. Tober, F. Zheng, Z. Wang, S.

Ruebush, A. Budge, and M.A. van Hove, J. Electron Spectrosc. and Relat. Phenom. 68, 19 (1994)

[7] M. Sagurton, E.L. Bullock, and C.S. Fadley, Surf. Sci. 182, 287 (1987)

[8] R.S. Saiki, A.P. Kaduwela, J. Osterwalder, D.J. Friedman, C.S. Fadley, and C.R. Brundle, Surf. Sci. 281, 270 (1993); H.P. Bonzel, Prog. in Surf. Sci. 42, 219 (1993)

[9] S.A. Chambers, Adv. in Phys. 40, 357 (1990); W.F. Egelhoff, Jr. in Critical Reviews in Solid State and Materials Sciences, 16, 213 (1990); D. Naumovic, A. Stuck, T. Greber, J. Osterwalder, and L. Schlapbach, Phys. Rev. B47, 7462 (1993)

[10] D.J. Friedman and C.S. Fadley, J. Electron Spectrosc. and Relat. Phenom. 51, 689 (1990)

[11] A.P. Kaduwela, D.J. Friedman, and C.S. Fadley, J. Electron Spectrosc. and Relat. Phenom. 57, 223 (1991)

[12] J.J. Rehr and R.C. Albers, Phys. Rev. B 41, 8139 (1990)

[13] G. Binnig, H. Rohrer, Ch. Gerber, and E. Weibel, Phys. Rev. Lett. 49, 57 (1982)

[14] J.A. Golovchenko, Science 232, 48 (1986); P.K. Hansma and J. Tersoff, J. Appl. Phys. 61, 1 (1987); G. Binnig and H. Rohrer, Rev. Mod. Phys. 59, 615 (1987); F. Ogletree and M. Salmeron, Prog. Solid St. Chem. 20, 235 (1990)

[15] C.J. Davisson and L.H. Germer, Phys. Rev. 30, 705 (1927)

[16] J.B. Pendry, Low Energy Electron Diffraction, Academic Press, New York (1974); M.A. Van Hove, W.H. Weinbergand, C.-M. Chan, Low Energy Electron Diffraction, Springer Verlag, Heidelberg (1986)

[17] Excellent reviews of the metal oxides can be found in V.E. Henrich and P.A. Cox, The Surface Science of Metal Oxides, Cambridge University Press, Cambridge (1994)

[18] S.J. Tauster, S.C. Fung, and R.L. Garten, J. Amer. Chem. Soc. 100, 170 (1978); G.L. Haller and D.E. Resasco, Adv. Catal. 36, 173 (1989)

[19] M.J. Madon and S.R. Morrison, Chemical Sensing with Solid State Devices, Academic Press, San Diego (1989)] and metal-ceramic bonding for corrosion resistance in high-temperature materials [18. M.J. Bennett, in High Temperature Corrosion, edited by R.A. Rapp (NACE, Houston, TX), 145 (1983)

[20] M.J. Bennett, in High Temperature Corrosion, edited by R.A. Rapp (NACE, Houston, TX), 145 (1983)

[21] S. Yoshii, O. Ishii, S. Hittori, T. Nakagawa, and G. Ishida, J. Appl. Phys. 53, 2556 (1982); E. Kay, R.A. Sigsbee, G.L. Bona, M. Taborelli, and H.C. Siegmann, Appl. Phys. Lett. 47, 533 (1985); S.S.P. Parkin, R. Sigsbee, R. Felici, and G.P. Felcher, Appl. Phys. Lett. 48, 604 (1986); A. Aeschlimann, G.L. Bona, F. Meier, M. Stampanoni, G. Zampieri, and H.C. Siegmann, Appl. Phys. Lett. 49, 824 (1986)

[22] V. Maurice, M. Salmeron, and G.A. Somorjai, Surf. Sci. 237, 116 (1990); M.C. Wu, J.S. Corneille, C.A. Estrada, J.W. He, and D.W. Goodman, Chem. Phys. Lett. 182, 472 (1991)

[23] G.H. Vurens, M. Salmeron, and G.A. Somorjai, Surf. Sci. 210, 129 (1988); G.H. Vurens, V. Maurice, M. Salmeron, and G.A. Somorjai, Surf. Sci. 268, 170 (1992)

[24] H.C. Galloway, J.J. Benitez, and M. Salmeron, Surf. Sci. 198, 127 (1993); H.C. Galloway, J.J. Benitez, and M. Salmeron, J. Vac. Sci. Technol. A12, 2302 (1994)

[25] W. Weiss, A. Barbieri, M.A. Van Hove, and G.A. Somorjai, Phys. Rev. Lett. 71, 1884 (1993); A. Barbieri, W. Weiss, M.A. Van Hove, and G.A. Sormojai, Surf. Sci. 302, 259 (1994)

CHAPTER 2

EXPERIMENTAL

2.1. INSTRUMENTATION

It is clear that no one surface structure probe directly and unambiguously provides all of the desired information on atomic identities, coordination numbers, positions, bond distances, and bond directions within the first 3-5 layers of a surface. The still relatively small number of surface structures for which there is a general consensus in spite of a few decades of careful study on some of them testifies to the need for using complementary information from several methods. In this dissertation, the three complementary surface structure probes, x-ray photoelectron diffraction (XPD), scanning tunneling microscopy (STM), and low-energy electron diffraction (LEED) have for the first time been combined in a single ultrahigh vacuum (UHV) system. This new system has been utilized to study the structure and growth mechanisms of iron oxide films on Pt(111).

A new custom-built UHV specimen preparation and characterization chamber equipped with an STM (McAllister Associates microscope with Digital Instruments Nanoscope II controls and software) and a four-grid LEED optics (Princeton Research, Model 118) were incorporated into an existing Vacuum Generators ESCALAB5 photoelectron spectrometer as shown in Fig. 2.1(a). This VG spectrometer had also in prior work in our laboratory been equipped with a Surface Science Laboratories Model 3390 multichannel detector to increase XPS and XPD data acquisition speed, and with externally-selectable tube arrays for high-accuracy angle definition, as described in detail elsewhere [1,2]. The STM/LEED chamber also provides for *in situ* bombardment with Ar ions for surface cleaning, deposition of Fe by means of a Knudsen cell, and

monitoring of deposition thickness by means of a quartz-crystal microbalance (QCM, Inficon Model 751-001-G1). The STM/LEED chamber can be separated by a gate valve from the XPS/XPD chamber during photoelectron measurements, or to permit the oxidation of deposited iron by backfilling with oxygen and heating, as described further below.

A new custom-built long-travel two-axis sample goniometer was also built as part of this dissertation, and it has special facilities for high temperature heating by electron bombardment and for *in situ* sample transfer between the high-precision two-axis goniometer used for XPS, XPD, and LEED measurements shown in Fig. 2.1(b) and the STM stage. The basic operation of the sample rotation mechanism of Fig. 2.1(b) is described in detail elsewhere [3]. This new sample holder is designed so that the sample can be transferred from one technique to another by means of a specially-modified commercial wobble stick (MDC Model DG-275) as shown in Fig. 2.1(c). The wobble stick has been modified to have both a socket wrench and a right angle pin at its base, in addition to the normal externally-operable clamping jaws that have been custom-cut to mate with the end of the sample holder. The sample transfer from two-axis goniometer to STM stage is done in three steps. First, two screws which fasten the sample barrel to the goniometer (at far right in Fig. 2.1(b)) are loosened by the socket wrench mounted parallel to the jaws of the wobble stick so that the sample and sample holder can be released from the goniometer. The released sample holder assembly, still resting on the goniometer, is gripped by the jaws of the wobble stick and is then put on the intermediate parking stage mounted on the STM stage (just to the left of the STM sled in Fig. 2.1(c)). This second step is necessary because the limited movement of the wobble stick prevented us from putting the sample assembly directly from the goniometer to the STM stage by using only the jaws of the wobble stick. The last step is to lift the sample assembly from the intermediate stage by inserting the pin mounted

perpendicular to the jaws of the wobble stick into a mating hole located at the base of the sample assembly and then to put the sample on the STM stage. The sample transfer from the STM stage to the goniometer was done by simple inverting the steps described above.

Some other features of this instrument are two different sample parking stages, located in the STM/LEED chamber of Fig. 2.1(a). One is for extra rotatable samples, and can hold up to three of them. This stage normally is used for two extra single-crystal samples and a highly-oriented pyrolytic graphite (HOPG) reference sample for the testing and calibration of the STM. These extra samples can be interchanged without breaking vacuum. The other stage holds a simple frame that can rotate only in θ and on which is mounted four reference samples - a full-size Au sample, a Au dot of approximately 1 mm diameter, a full size Cu sample, and a phosphor-coated screen. The first three reference samples allow us to optimize the x-ray photoelectron spectrometer by calibrating the peak positions and finding the optimum sample position. The phosphor screen is also helpful in finding the positions of the x-ray flux and the LEED electron beam.

A final important improvement incorporated into this instrument is a new Windows-based software system developed by H. Xiao in our group. This program permitted automated rotation of both the polar (θ) and the azimuthal (ϕ) angles of emission during XPD data collection, with simultaneous plotting of intensities in a two-dimensional format. This software also added the capability that up to 10 different photoelectron peaks could be measured at each emission direction in order to make sure that the XPD data from each element were obtained for exactly the same sample positions and surface conditions.

This new instrument thus permitted us to study the same surface structure with three complementary probes - XPD, STM, and LEED - and to our knowledge it is the first to

be able to do this. As a first system of study with this instruments, we have chosen FeO_x/Pt(111), and this study serves to illustrate how important this complementarity is, as discussed in the following chapters.

2.2. EXPERIMENTAL PROCEDURE

All the data reported in this paper were taken in the combined XPS/XPD, STM, and LEED system of Fig. 2.1 with base pressures less than $8x10^{-11}$ Torr for the XPS/XPD chamber and $1x10^{-10}$ Torr for the STM/LEED chamber. The Pt(111) sample cleaning and Fe oxidation were done in the XPS/XPD chamber and Fe deposition was done in the STM/LEED chamber.

Platinum single crystal preparation:

The platinum single crystal was cut and oriented within less than 0.2° of the (111) plane, polished by the usual metallurgical procedures, and then mounted onto the special long-travel two-axis goniometer, from which it could also be demounted *in situ* for STM study. The crystal was prepared by B. Petersen of the Shirley group and loaned to us for this study. The misorientation of the Pt(111) was judged by both Laue back diffraction and the step density as seen in typical wide-scan STM images on clean Pt(111). For example, terrace widths of $\geq$ 400 nm were typical from several STM images taken on the clean Pt surface, as shown in Fig. 2.2. However, these monatomic steps tended to bunch together as the number of oxidation and cleaning cycles was increased during the course of this study, as shown in Fig. 2.3; this left even larger flat terraces between the bunched steps. This Pt(111) crystal was mounted on a ceramic goniometer barrel using a Ta clip, and could be heated by electron bombardment from

the back. The alignment of the surface with respect to the azimuthal rotation axis was checked by reflecting a laser from the front surface and rotating the sample in ϕ; this alignment was also checked periodically *in situ* during our measurements. In this way, the surface normal was kept within 0.2-0.5° of the azimuthal rotation axis during all of our measurements. The temperature was measured with an infrared pyrometer that was initially calibrated by a chromel-alumel thermocouple mounted to the top of the Pt crystal. The Pt(111) surface was prepared by repeated cycles of sputtering with 1 KeV Ar^+ ions and subsequent annealing to T = 1500 K in $4x10^{-6}$ Torr oxygen. A final heating to that temperature for about 30 sec without oxygen resulted in a clean surface. This cleaning procedure has been used in previous studies of Pt(111) [5-8]. The cleanliness of the surface was checked by XPS core-level peaks and no detectable contaminant peaks were found. A very well ordered surface was also verified by a sharp (1x1) LEED pattern.

Iron oxide growth:

The iron oxide thin film growth was done in two steps. First, iron was evaporated onto the clean Pt(111) surface using 99.999% pure iron wire wrapped around a resistively heated tungsten wire. The quartz-crystal microbalance was used to adjust the deposition rate to ~1 Å/5 min., for which the maximum pressure during the evaporation was about $4x10^{-10}$ Torr. After depositing the desired amount of iron onto the clean Pt(111) surface, the sample was moved into the XPS/XPD chamber of the VG spectrometer, where it was heated for about 1 minute in $4x10^{-6}$ Torr oxygen to T = 980 K and cooled rapidly down to room temperature afterwards. This again is a recipe that has been shown to provide full oxidation in prior studies of FeO_x/Pt(111) [5-8].

X-ray photoelectron spectroscopy (XPS) and x-ray photoelectron diffraction (XPD):

All photoelectron spectra for XPS and XPD were obtained with Al Kα radiation (1486.7 eV), although either Al or Mg radiation was available in this system from a commercial twin-anode x-ray source. The experimental geometry for the XPS/XPD measurements is described in detail elsewhere [1,2], but Fig. 1.2 defines important angular variables. A typical overall XPS spectrum obtained from a 1.75 ML iron oxide film grown on Pt(111) is shown in Fig. 2.4, with various peaks labelled. The weaker Fe 3s and 3p photoelectron peaks are hidden under the very strong Pt 4f region of the spectrum. All XPD data were obtained with angular resolutions of ± 3.0° using a tube array before the analyzer entry, as described in detail elsewhere [1]. Although this tube array reduced intensities considerably [1], it permitted better defining both angular resolution and the area of the sample surface seen by the electron lens and spectrometer. The latter was important to avoid seeing spurious O 1s signal from parts of the sample holder adjacent to the Pt(111) surface. For each direction of emission in an angle scan, Pt 4f, Fe $2p_{3/2}$, and O 1s XPD intensities were obtained, using the new software system discussed in Section 2.1. These photoelectron peaks correspond to kinetic energies of: Pt 4f--1414 eV, O 1s--956 eV, and Fe $2p_{3/2}$--777 eV, and these energies are high enough to exhibit strong forward scattering effects in photoelectron diffraction [9-11]. Intensities were measured over essentially the full 2π steradians above the sample surface, from 6° above the surface plane to the surface normal. To reduce data collection times, each large-scale XPD intensity set or diffraction pattern was measured over only one third of the hemisphere above the sample and a 2π intensity map then completed by exploiting the threefold symmetry of the crystal in azimuth. The data was accumulated as a set of 120° azimuthal scans. The accuracy of this threefold data folding was justified for each case by comparing the individual 120° intensity scans in

the large data set to selected full 360° azimuthal XPD scans, as described in more detail in Appendix B. The polar emission angle from the surface was first set to $\theta = 6°$ and then increased to 90° in steps of $\Delta\theta = 2°$ after each 120° azimuthal rotation. The azimuthal step size was $\Delta\phi = 2°$ for $\theta = 6°$, and was increased with increasing polar angle θ so as to cut data acquisition times while still giving an almost uniform sampling density in solid angle over the hemisphere, a procedure first introduced by Osterwalder et al. [12,13]. The true θ and ϕ varies from the expected θ and ϕ due to an accumulation of minute errors in setting angles. These total angular discrepancies are estimated to be less than $\pm$ 1.5° for ϕ and $\pm$ 0.2° for θ after completing the full 2π intensity maps. Fig. 2.5 shows Pt 4f emission XPD patterns obtained from clean Pt(111) with the data acquisition method described above.

Scanning tunneling microscopy (STM):

The STM images and other STM data analysis reported in this dissertation were obtained using the standard operating procedures and options of the Nanoscope II software. The only special mechanical modification necessary for using the McAllister STM was the addition of a small "sled" fabricated from the Al-Cu alloy Ampco 18 between the sample holder and the two WC rails along which specimen coarse approach is made. The purpose of this sled was to lower the friction in UHV between the demountable sample holder and the rails so that the inertial piezoelectric jerking motion necessary for coarse approach was fully reliable. Without this sled present, the sample would often stick on these rails, impeding or even preventing the coarse approach. This sled is shown in Fig. 2.1(c).

Two different types of STM tips were used in this study: a diagonally-cut Pt/Ir alloy wire of 0.25 mm overall diameter, and an electrochemically-etched W wire of 0.25 mm

overall diameter. Two Pt/Ir tips and six W tips were loaded into the STM at the start of the experiment, and these could be interchanged *in situ*. Both types of tips gave good atomic images, with no systematic differences in behavior between them. The STM images consist of 400x400 data points, and were obtained in either constant-current or constant-height mode (as defined in Chapter 1), with bias voltages of sample relative to tip and tunneling currents as given below for each case considered. All the dimensions reported here were obtained after accurate calibration of the x, y, and z piezo scales (with x and y being in the surface plane, and z being perpendicular to it). The x and y piezoes were calibrated by measuring the atomic spacings on a reference HOPG sample loaded into the STM/LEED chamber, while the z piezo was calibrated from multiple measurements of the monatomic step heights of the clean Pt(111) surface, as shown in Fig. 2.2.

Low energy electron diffraction (LEED):

LEED patterns were recorded with a Polaroid camera, and obtained at a few energies to verify the types of diffraction patterns seen. No current-versus-voltage curves were measured. Other aspects of analyzing the LEED data so as to derive real-space atomic distances appear in Appendix C.

The long range order of clean Pt(111) and of iron oxide films grown on Pt(111) was checked via LEED patterns and no detectable changes were found before and after XPD data collection and STM studies. All XPD, STM, and LEED data reported in this dissertation were obtained in the single UHV system of Fig. 2.1, and where results from these techniques are compared, they are also from the same preparation of a given surface.

Figure 2.1. (a) The VG ESCALAB5 photoelectron spectrometer that has been modified so as to include STM, LEED, and automated XPD capability in a single UHV system. The major components of this system are indicated in the figure.

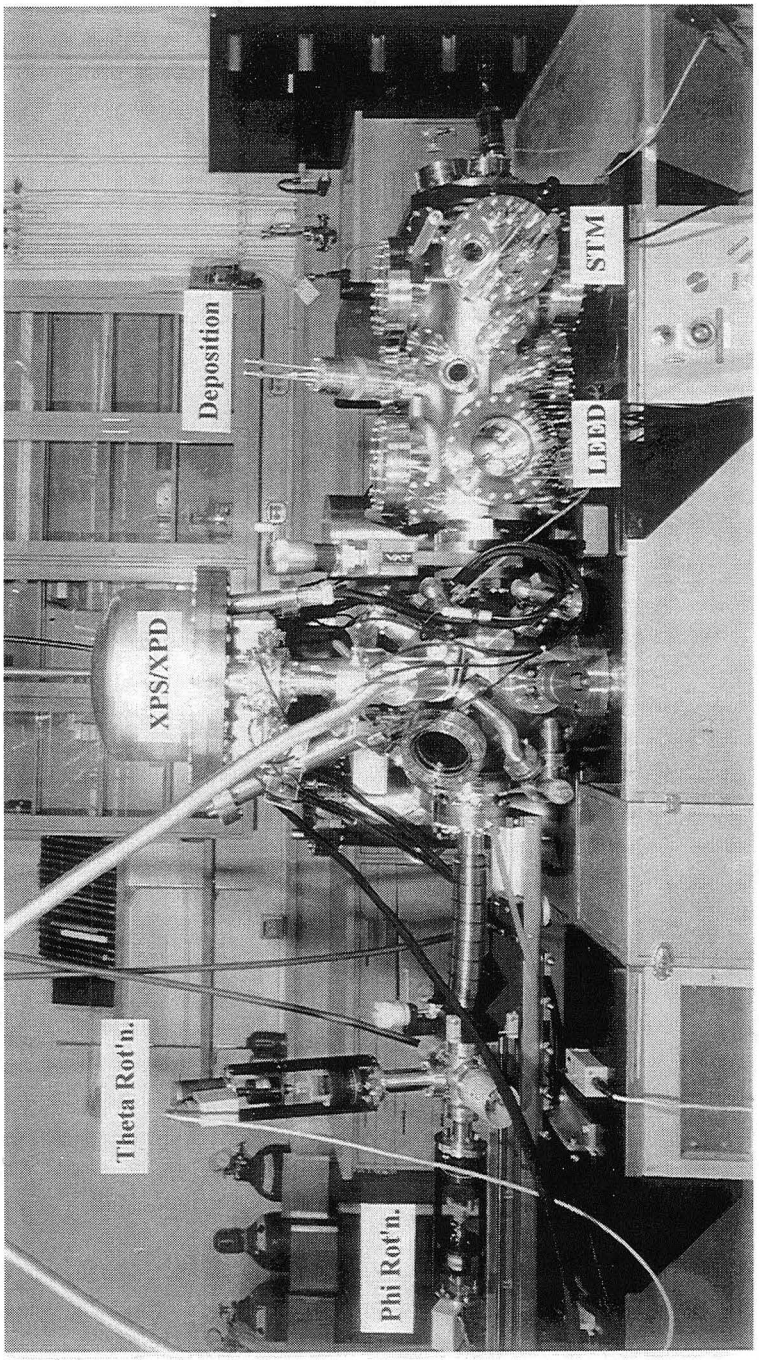
Theta Rot'n.
XPS/XPD
Deposition
STM
LEED
Phi Rot'n.

Figure 2.1. (b) The custom-built sample holder permitting transfer from the variable-temperature goniometer to the STM by means of a commercial wobble stick. The basic mechanism of the two-dimensional goniometer is described in detail elsewhere [4].

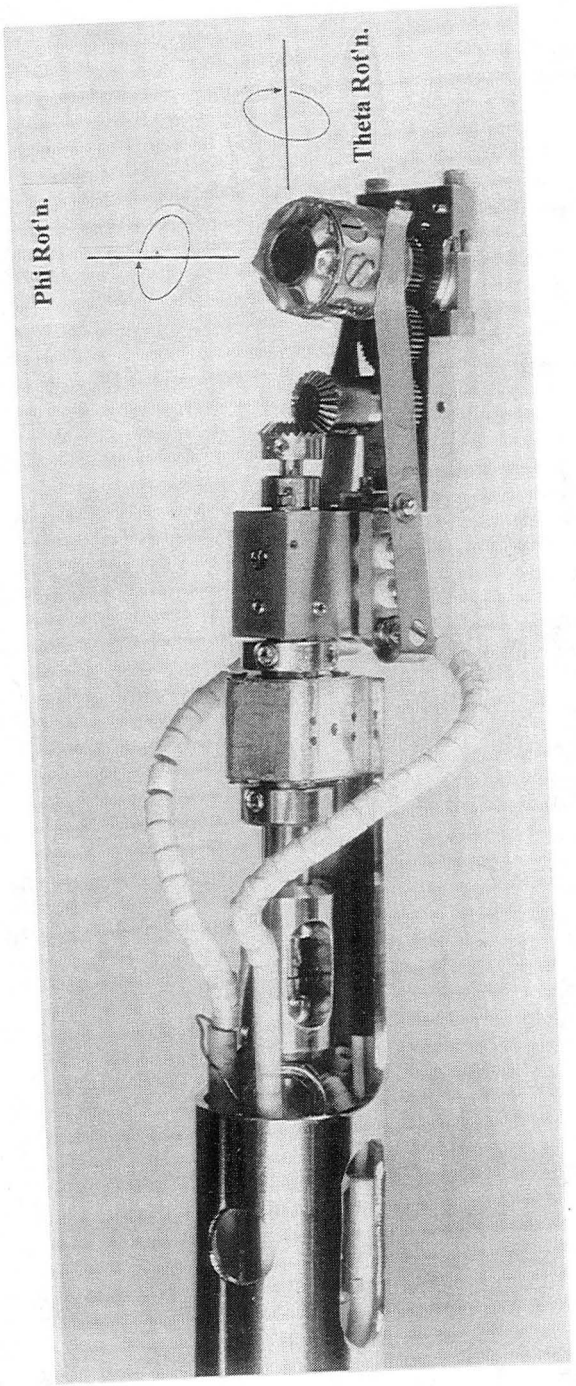
Phi Rot'n.
Theta Rot'n.

Figure 2.1. (c) Photo of the goniometer-STM transfer region, illustrating the second step of sample transfer from the goniometer to STM, as described in the text. Also seen are the STM sled and the specially-modified wobble stick as indicated in the figure.

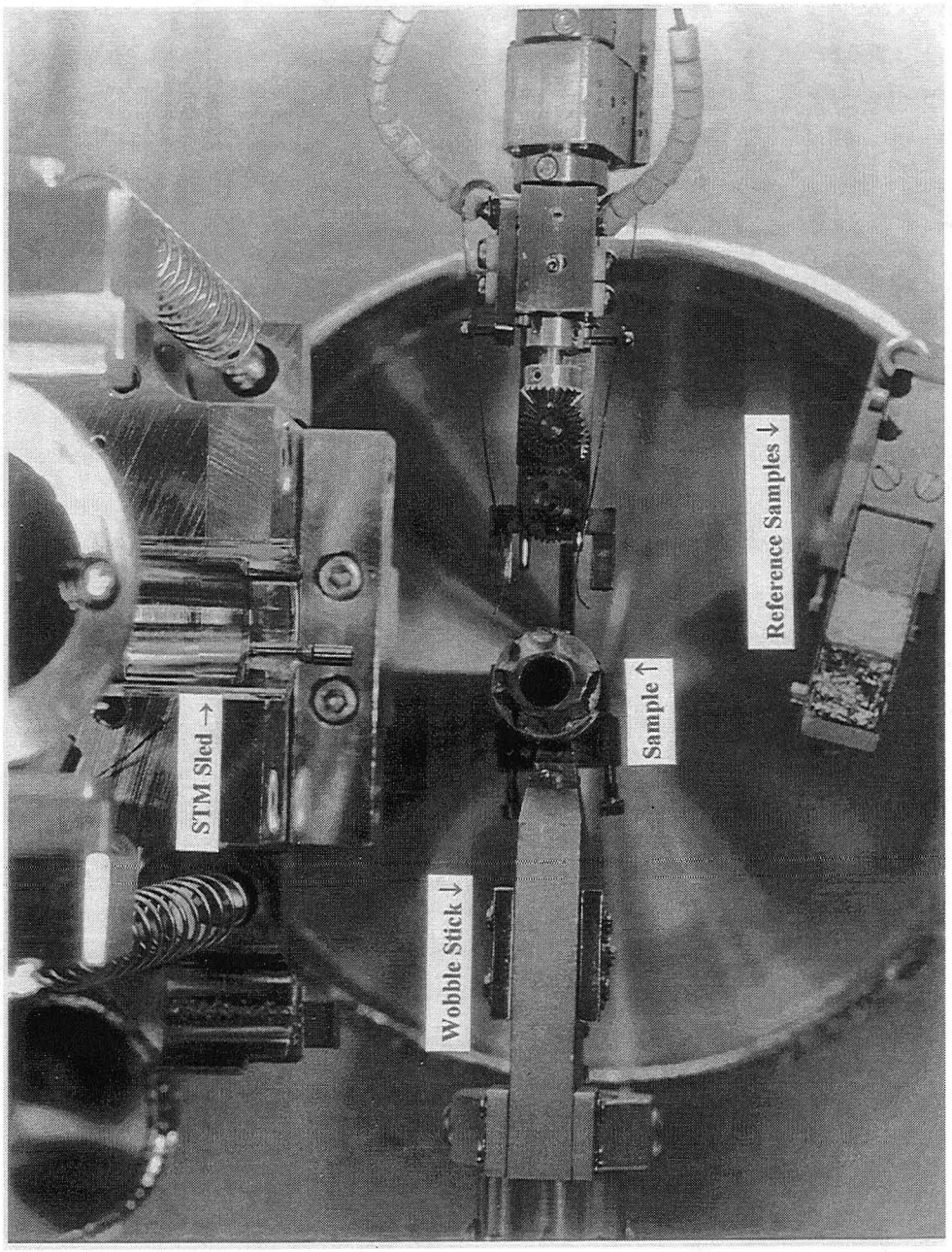
STM Sled →
Wobble Stick ↓
Sample ↑
Reference Samples ↓

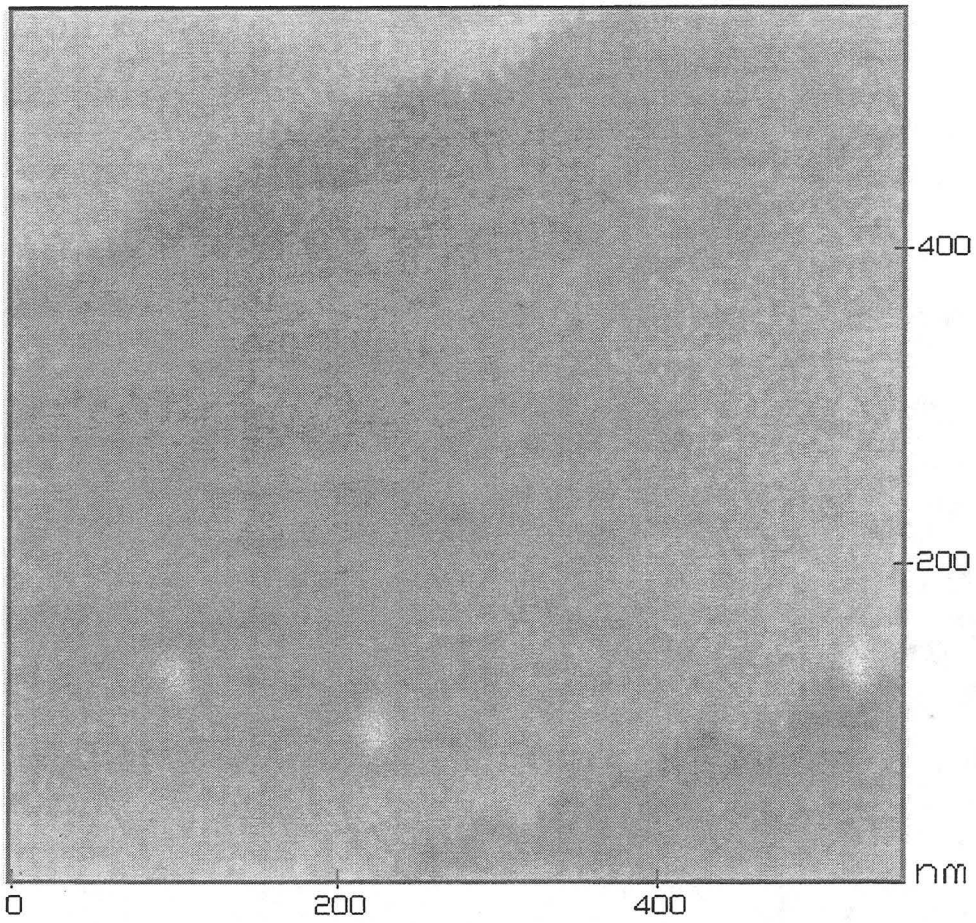

Figure 2.2. A typical STM image on clean Pt(111) taken in constant current mode at the beginning of this study. The 545 x 545 nm image shows two monatomic steps separating a terrace of typical widths of ≥ 400 nm. The current is 2.3 nA and the sample bias voltage is 200 mV.

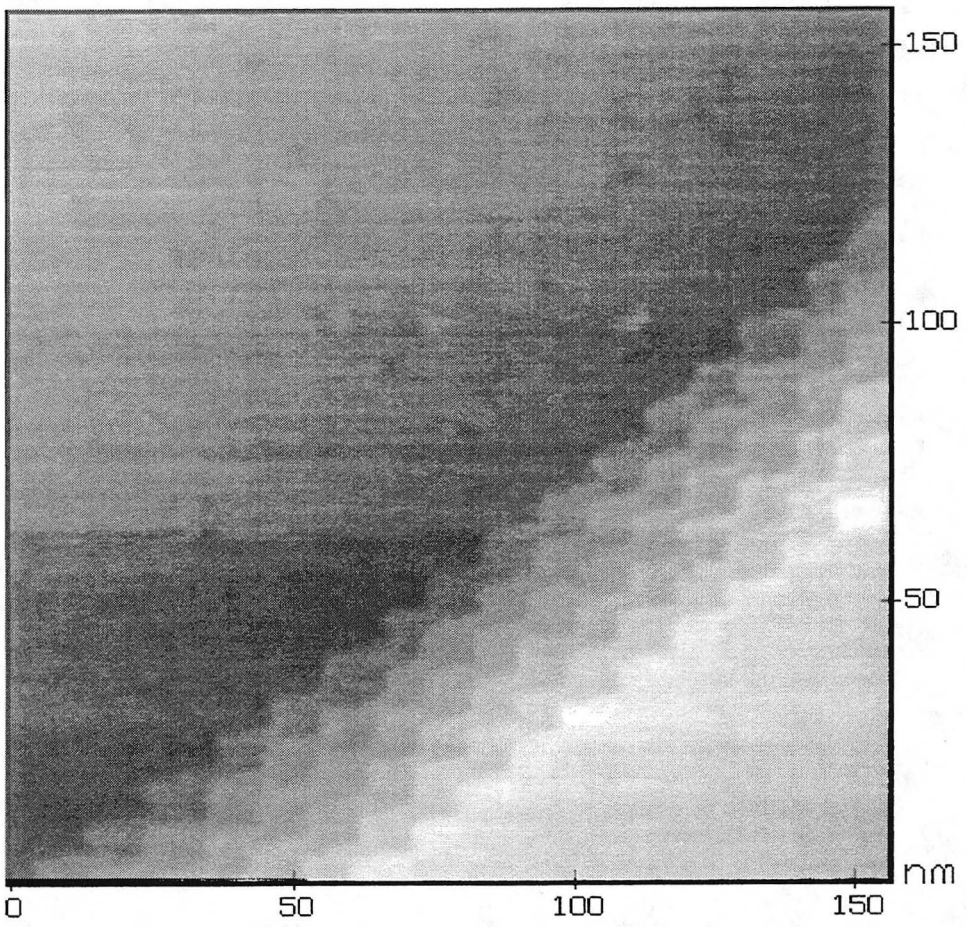

Figure 2.3. An STM of clean Pt(111) taken in constant current mode after several cycles of cleaning, iron deposition, and oxidation. This 156 x 156 nm image shows six monatomic steps bunched together, in a regular herringbone pattern. The current is 2.4 nA and the sample bias voltage is 460 mV.

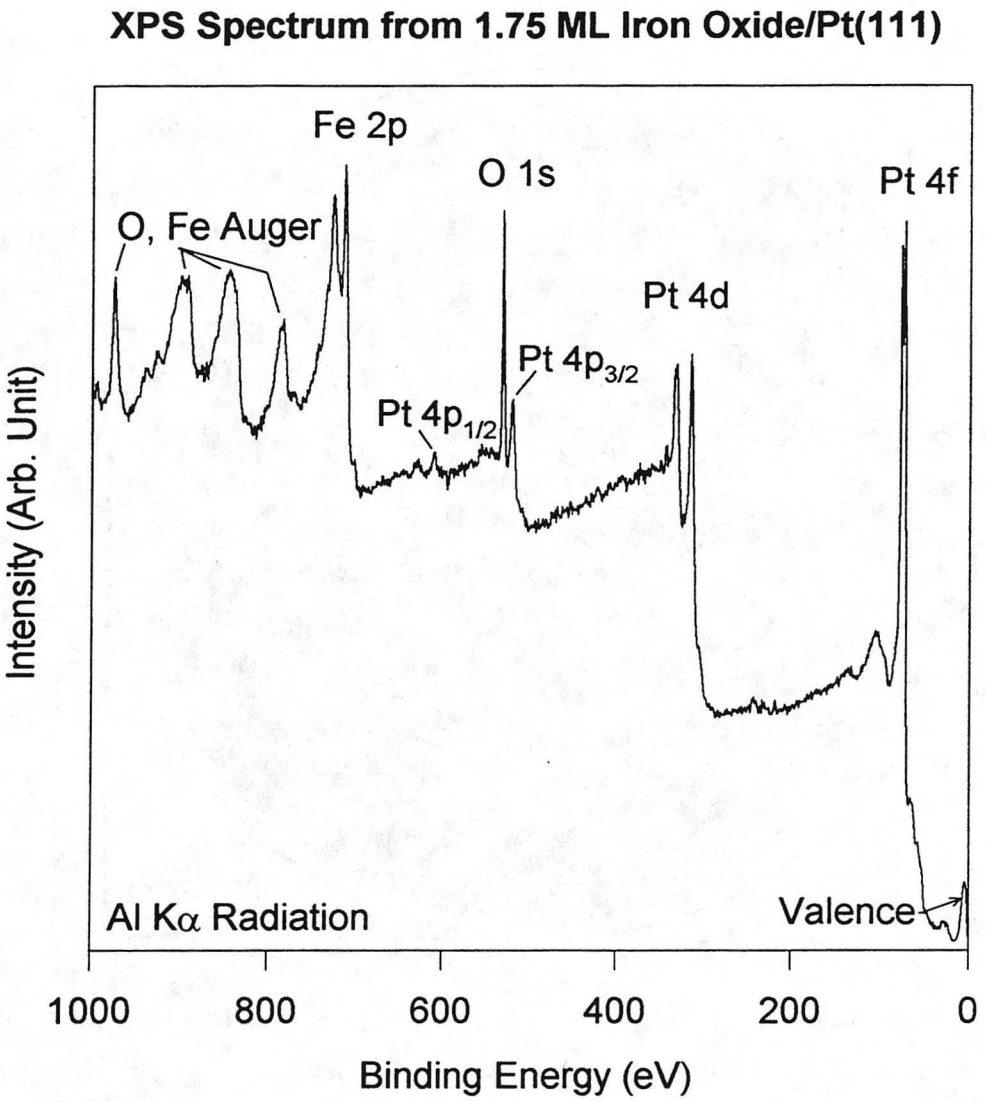

Figure 2.4. A typical XPS spectrum taken from a 1.75 ML iron oxide film on Pt(111) with Al Kα radiation as the excitation source. The core level peaks of Pt, O, and Fe are shown as well as Auger peaks.

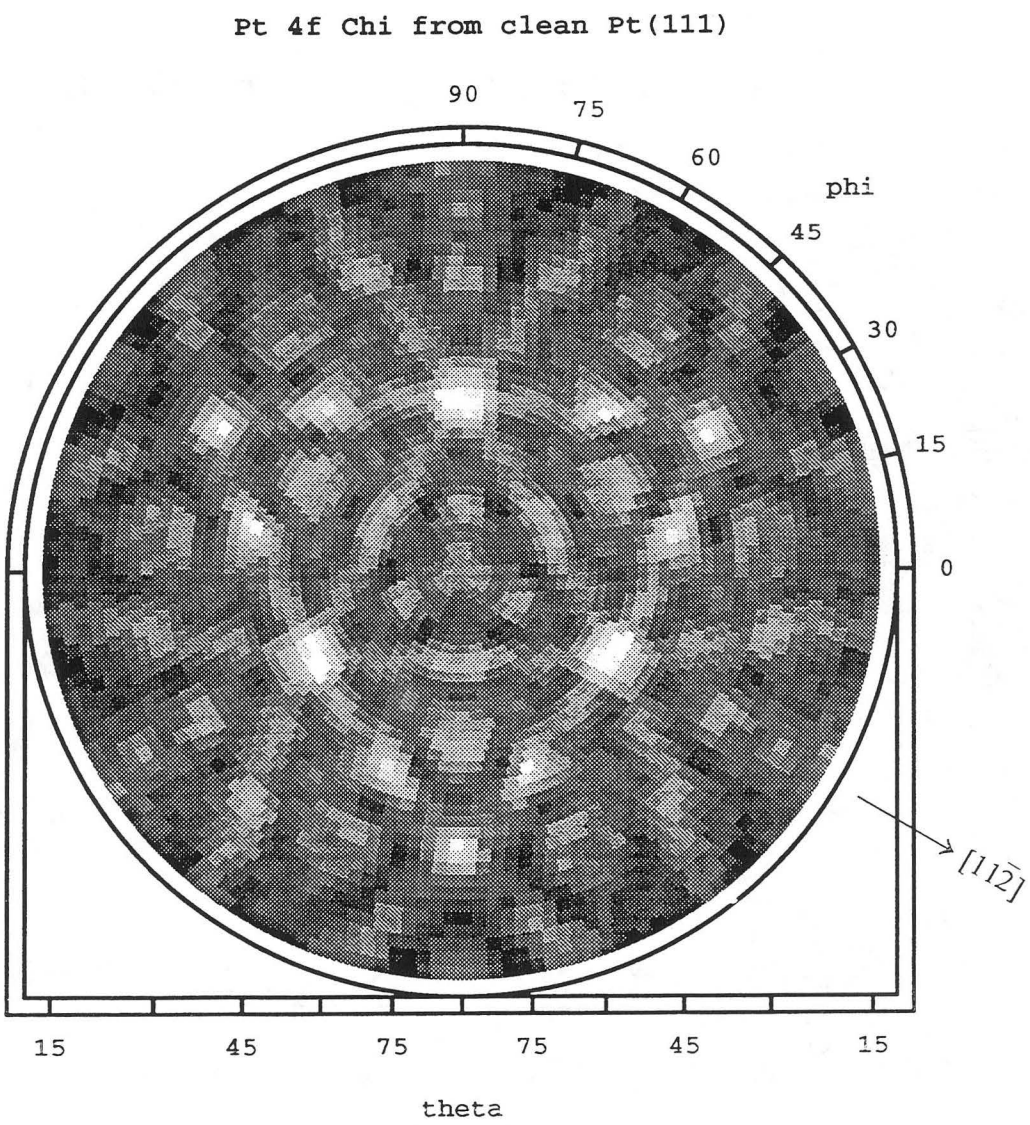

Figure 2.5. The Pt 4f XPD pattern obtained from clean Pt(111). The nearest (next-nearest) neighbor forward scattering peaks are shown at the polar angle of 55° (35°) along <11$\bar{2}$> (<$\bar{1}$2$\bar{1}$>) azimuths.

REFERENCES

[1] R.C. White, C.S. Fadley, R. Trehan, J. Electron Spectrosc. Relat. Phenom. 41, 95 (1986)

[2] J. Osterwalder, M. Sagurton, P.J. Odrers, C.S. Fadley, B.D. Hermsmeier, and D.J. Friedman, J. Electron Spectrosc. Relat. Phenom. 48, 55 (1989)

[3] R.J. Baird and C.S. Fadley, J. Electron Spectrosc. Relat. Phenom. 11, 39 (1977)

[4] G.H. Vurens, M. Salmeron, and G.A. Somorjai, Surf. Sci. 210, 129 (1988)

[5] G.H. Vurens, V. Maurice, M. Salmeron, and G.A. Somorjai, Surf. Sci. 268, 170 (1992)

[6] H.C. Galloway, J.J. Benitez, and M. Salmeron, Surf. Sci. 198, 127 (1993)

[7] W. Weiss, A. Barbieri, M.A. Van Hove, and G.A. Somorjai, Phys. Rev. Lett. 71, 1884 (1993)

[8] H.C. Galloway, J.J. Benitez, and M. Salmeron, J. Vac. Sci. Technol. 12, 2302 (1994)

[9] L.G. Petersson, S. Kono, N.F.T. Hall, C.S. Fadley, and J.B. Pendry, Phys. Rev. Lett. 42, 1545 (1979)

[10] H.C. Poon and S.Y. Tong, Phys. Rev. B30, 6621 (1984).

[11] S.Y. Tong, H.C. Poon, and D.R. Snider, Phys. Rev. B32, 2096 (1985).

[12] J. Osterwalder, T. Greber, A. Stuck, and L. Schlapbach, Phys. Rev. B44, 13764 (1991)

[13] D. Naumovic, A. Stuck, T. Greber, J. Osterwalder, and L. Schlapbach, Phys. Rev. B47, 7462 (1993)

CHAPTER 3

GROWTH OF THE FIRST MONOLAYER OF IRON OXIDE ON Pt(111)

3.1. INTRODUCTION

The surface structure of metal oxides has not been studied as extensively as that of metal and semiconductor single crystals. The surfaces of metal-oxide single crystals are difficult to prepare with the bulk stoichiometry and their insulating properties often make surface characterization difficult using techniques such as the various electron spectroscopies or STM. However, in the case of several metal oxide/metal systems, including iron oxide/platinum, oxide overlayers have been found to grow in an ordered manner on a metal substrate [1-7]. Provided that the oxide is not too thick, these systems thus permit studying epitaxial growth using the full array of surface structure probes. The novel interface created between the metal substrate and the oxide overlayer is also a very important aspect of these systems, with important applications to oxide supported metal catalysts where strong metal support interactions are found [8-11], as well as to metal-ceramic bonding for corrosion resistance in high-temperature materials [12-16]. Furthermore, the magnetic properties of the different oxides of iron are utilized in high-density magnetic recording media [17].

We begin by considering the growth of up to one monolayer (ML) of iron oxide on Pt(111). This system has been studied with a combination of LEED and ion scattering spectroscopy (ISS) [3,4], as well as with STM [5]. Simultaneously applying LEED and ISS to this monolayer growth led to the proposal of a (111)-type FeO bilayer forming a (10x10) coincidence lattice or lateral superlattice on the Pt(111) substrate. However, these results did not permit concluding whether Fe or O atoms or both occupied surface positions, since the ISS data showed both Fe and O peaks. On the other hand, a

subsequent STM study concluded that an incommensurate overlayer lattice forms for which a short overlayer periodicity of 3.1 Å is modulated by a large periodicity of ~26 Å. This was suggested to involve an Fe-O bilayer similar to those in bulk FeO with (111) orientation. In addition, a rotational mismatch between the bilayer and the substrate of about 0.6°, resulting in a 5.2° rotational mismatch of the large periodicity, has been proposed based on the existence of two equivalent domains of the large periodicity in adjacent terraces. This rotational mismatch is illustrated in the proposed structural model by Galloway et al. shown in Fig. 3.1. In this proposed model, two equivalent domains can be obtained by plus and minus rotations by 0.6° of the Fe-O bilayer from the $[1\bar{1}\,0]$ direction of Pt(111), leading to plus and minus rotations by 5.2° of the large periodicity of the overlayer. But these prior studies left several open questions to be answered about this interesting monolayer of FeO, such as the detailed atomic geometry within the iron oxide (whether Fe or O or both occupy surface positions and what the bond lengths and directions are between Fe and O), and the orientation of the topmost layer in the bilayer (which we shall show definitively to be O) with respect to the underlying Pt lattice. The simultaneous study of this system for the first time by XPD, STM, and LEED ultimately permits answering all of these questions.

3.2. RESULTS AND DISCUSSION

3.2.1. Coverage and Stoichiometry

These thin iron oxide films were prepared by depositing 0.75 and 1.0 ML of Fe on clean Pt(111) and then oxidizing the Fe in an oxygen environment, as described in Chapter 2. The Fe $2p_{3/2}$ binding energy (BE) in this 1 ML regime of oxide thickness as

measured by XPS is about 709.6 eV, consistent with prior work suggesting an Fe^{2+} state [18,19]. The iron chemical states and oxide stoichiometry will be discussed in more detail in Chapter 4, together with those for the thicker oxide layers for which the same question as to chemical state arises.

The coverages of Fe as initially deposited before oxidation were determined using the QCM, and then cross-checked using a standard XPS quantitative analysis method for the case of a semi-infinite substrate with an overlayer of uniform thickness [20,21]. The details of quantitative XPS analyses for this case as well as the Fe:O stoichiometry analysis after oxidation are discussed in Appendix A. With the XPS quantitative analysis method as described in Appendix A, the Fe coverages as determined by QCM and XPS before oxidation are in good agreement, showing differences of less than ±20 %. In addition, relatively wide scan STM images after oxidation also provide an independent coverage determination for this system, since regions of the surface with the monolayer structure of FeO are clearly distinguishable from coverages less than or more than 1 ML, as will be discussed later for each case considered. The results of three independent methods (QCM, XPS, and STM) for determining the coverages of these iron oxide films are thus in good agreement with one another, as shown in Table 3.1 together with results for thicker oxide layers that will be discussed in more detail later.

For the Fe:O stoichiometry analysis of the final iron oxide films, Fe $2p_{3/2}$ and O 1s peak intensities for each film were obtained by analyzing the full 2π intensity maps in order to avoid previously discussed scattering and diffraction effects [22,23]: azimuthally-averaged data for both peaks were fit with a smooth spline curve using a program written by S. Ruebush in our group, and a θ-dependent peak ratio then derived. The peak intensities over the most reliable range of the 2π intensity maps near the surface normal of $60° \leq \theta \leq 90°$ that are known to minimize spurious effects due to

surface refraction and surface roughness [25] were used for Fe:O stoichiometry analysis. The 2π intensity maps and the method for averaging intensities at each θ will be discussed later as we consider the XPD data in detail. With these averaged intensities for both O and Fe, the Fe:O stoichiometry of both coverages are found to be $FeO_{1.07-1.08}$, which is very close to the 1:1 expected for FeO.

In order to further confirm our results for the XPS quantitative analysis of the Fe:O stoichiometry, XPS Fe $2p_{3/2}$ and O 1s peak intensities were also measured for pressed pellets of various freshly-crushed high-purity iron oxide powders: FeO = $Fe_{1.0}O_{1.0}$, $Fe_3O_4 = Fe_{1.0}O_{1.33}$, and $Fe_2O_3 = Fe_{1.0}O_{1.5}$. Even though the absolute core level BE's of these powder samples cannot be used in a quantitative way due to possible surface charging, the XPS peak intensities were measured in exactly the same way as for the epitaxial iron oxides on Pt(111), as described in Appendix A. The resulting experimental XPS O 1s:Fe $2p_{3/2}$ peak intensity ratios for these oxides were 0.79, 0.85, and 1.03 respectively. If we choose Fe_2O_3, the most stable form of oxide in air, as a reference, the bulk stoichiometry dictates that these ratios should be 0.68, 0.91, and 1.03, respectively. The experimental ratios for FeO and Fe_3O_4 thus track reasonable well with bulk stoichiometry: 16% off FeO and 7% off for Fe_3O_4. Such small deviations are not suprising, since the surfaces of these powders might well have had altered compositions relative to the bulk. Especially for the case of FeO, it is well known that FeO is easily oxidized in air, resulting in a higher O:Fe peak ratio as shown in our data. In any case, the peak ratio for both 0.75 ML and 1.0 ML iron oxide films grown on Pt(111) is about 0.64 which is slightly lower than that of powder FeO, but within 6% of it. This slightly higher O:Fe peak ratios for the powder FeO sample can thus easily be explained by the presence of adsorbed H_2O or CO from the residual gas in our vacuum system. The results of XPS relative peak intensity analyses on different iron oxide powder samples thus support the results of our XPS quantitative analysis,

and leading to the conclusion that the Fe:O stoichiometry is 1:1. The theoretical simulations of full 2π XPD patterns to be discussed in the next chapter also provide an indirect way of determining Fe:O stoichiometries, since the cluster models used for the calculations have compositions implicitly assumed in them. Comparisons between experiment and these simulations further confirm that oxide layers with 0.75 - 1.0 ML initial Fe coverage are formed with the FeO stoichiometry.

3.2.2. Atomic Structure

Here we will first present and discuss our results from LEED (a non-atom-specific probe of surface structures with long-range order when the most intense diffraction spot intensities are analyzed), then from STM (a non-atom-specific probe of both short-range and long-range order, as well as disorder), and finally from XPD (an atom-specific probe of short-range order). This was also the temporal sequence in which the methods were applied after the preparation of a given iron oxide film, to be certain that only fully characterized overlayers were studied by XPD.

LEED:

The LEED patterns shown in Figs. 3.2(a) and (b) , taken with a beam energy of 54 eV for 0.75 ML and 1.0 ML iron oxide films are essentially identical, which implies that the long-range atomic order in the films is basically the same. These patterns exhibit a nearly hexagonal pattern that is in fact three-fold symmetric; each of the six main spots is surrounded by a rosette of six satellite spots. Even though these six rosettes appear to lead to six-fold symmetry, they are three-fold symmetric if the detailed intensities of the six satellite spots are considered. The outermost six satellite spots as viewed from the

(0,0) spot, which coincide with spots from the underlying Pt, show differences in intensities, with three of them being brighter than the other three. This LEED pattern has been observed and discussed in previous studies on this system [4,5]. However, something appearing in our results that has not been commented on before is that the inner three satellite spots among each set of six that are closest to the (0,0) beam are more streaked than the other three. These streaked spots, and in fact the entire rosette pattern, we observe to become sharper and more symmetric as the initial Fe coverage is increased somewhat above 1.0 ML, as will be discussed in Chapter 4. The brightest six spot positions reveal a lateral lattice constant of ~3.1 Å, which is ~12 % larger than the lateral periodicity of Pt(111), which is 2.77 Å. Due to this lattice mismatch, an incommensurate structure and lateral superlattice like that in Fig. 3.1 is formed in which approximately 8 interatomic spacings of the overlayer fit onto about 9 interatomic spacings of the Pt(111) surface, thus generating the satellite spots. Figure 3.2(c) shows the lateral structure proposed for this superlattice by Galloway et al. [5], in which the two overlapping atomic lattices (small periodicity) are rotated with respect to one another by 0.6°, and the resulting Moiré pattern shows atomic coincidence points (the large periodicity) that are rotated by ~5°, here in the second sense of rotation opposite to that in Fig. 3.1. This interference pattern clearly shows both short and long periodicities which are responsible for the main spots and the satellite spots in the LEED pattern, respectively. The atomic structure proposed also involves only a slight expansion of the FeO(111) lateral lattice constant (3.10 Å) relative to that in the bulk, with the lattice constant of bulk FeO(111) in the cubic wustite phase having the NaCl structure being 3.04 Å. In fact, we will show below that the vertical Fe-O interplanar distance is significantly contracted in this overlayer, something which is consistent with an expansion of the lateral lattice constant.

STM:

After the XPS and LEED check on the iron oxide films, the crystal was allowed to cool down fully to room temperature before STM images were acquired. We will first present STM images of fairly large scanning ranges in order to discuss overall growth morphology and the influence of coverage on morphology, and then consider smaller-range atomically resolved images.

STM images for 0.75 ML and 1.0 ML iron oxide coverages with fairly large scanning ranges (~300-800 nm) are shown in Figs. 3.3(a) and 3.3(b), respectively. These are constant-current images with sample biases and tunneling currents given in the figure captions. In Fig. 3.3(a), the oxide has grown across two steps of monatomic height in the upper left of the image; and in Fig. 3.3(b), across two monatomic steps in the middle of the image. These images also provide information on the oxide coverage, since they are fairly large scale and were found to be typical over several images in different regions. As might be expected for a submonolayer coverage, the image for 0.75 ML in Fig. 3.3(a) shows some darker = lower, presumably empty, regions, and these occupy about 25% of the terraces, in good agreement with our QCM and XPS coverage measurements. More interesting in Fig. 3.3(a) is the observation that this submonolayer oxide appears to grow in a columnar fashion. As measured relative to the dark areas, these oxide columns furthermore have a height of about 2 Å, which is about the same as the ~2.6 Å estimated thickness of a (111) bilayer of FeO arrived at by considering the ionic radii of Fe^{2+} and O^{2-} and the vertical interlayer relaxation to be discussed in a later section. The 1.0 ML image in Fig. 3.3(b) generally shows smooth terraces, with some small islands here and there indicative of second-layer growth, and there is no more evidence of columnar growth. For this surface, the islands and a few small empty

"defect" regions occupied less than 10 % of the total area, suggesting a nearly perfect monolayer of FeO.

Figure 3.4(a) now shows a 5.8 nm x 5.8 nm constant-height image of 1.0 ML of FeO on Pt(111) recorded with a sample bias voltage of 454 mV and an average current of 1.36 nA. The low-index direction shown here was determined from full 2π Pt 4f XPD data on clean Pt(111). In agreement with prior STM work on this system by Galloway et al. [5], it is clear that 1 ML of FeO on Pt(111) can be imaged by STM, even though bulk FeO is an insulator with a 2.4 eV band gap [24]; in fact, the prior study made use of even lower bias voltages that are typical for tunneling on metal surfaces. The image in Fig. 3.4(a) clearly shows the existence of two periodicities with small and large unit cells, as indicated by the outlines. The large unit cell is drawn at the approximate center of a region that is brighter on the average. The small unit cell is of atomic dimensions, 3.0 Å ± 0.1 Å on each side, as derived most quantitatively from a Fourier transform analysis of the STM image using a standard feature of the Nanoscope II software (highest frequencies at 3.1 Å), while the larger unit cell measures 26 Å ± 2 Å on each side, as more clearly shown in the much larger scale image of Fig. 3.4(b). Fig. 3.4(b) is a 79.2 nm x 79.2 nm constant height image taken with a sample bias voltage of 459 mV and an average current of 1.4 nA. Only the large unit cell periodicity is visible in this image, although it is defected, thus creating different domains of sixfold symmetry that are difficult to distinguish. These larger unit cells are thus responsible for the satellite spots shown in the LEED pattern in Fig. 3.2(b), as discussed previously by Galloway et al [5]. This prior STM study also reported that there is about a ± 5° rotational mismatch between two domains of the long-range periodicity on adjacent terraces. We have also observed this rotational mismatch of two domains on a single terrace, as shown in the lower image of Fig. 3.4(b). This difference in results might be because our

Pt(111) surface had a lower step density than in this prior study (about a 0.4° miscut from (111) here, compared to the 1.0° miscut used previously [5]).

XPD-Experimental Results:

We have so far discussed results from two surface structure probes that are not atom specific. The remainder of this section will discuss atom-specific XPD data obtained from Pt, Fe, and O simultaneously for these iron oxide overlayers, with the goal of determining their internal atomic structure. The measured Pt, Fe and O XPD intensity maps with no correction for instrumental response, which in general makes intensity fall off to zero as θ goes to zero (i.e., for emission parallel to the surface) [25], are corrected in two steps. First, in order to smooth out the diffraction features in the 2π intensity maps, azimuthally-averaged intensities at each θ were fit with smooth spline functions [26]. This fitted curve $I_0(\theta)$ provides an estimate of the intensity in the absence of photoelectron scattering at each θ. Then the normalized XPD intensity modulation function $\chi(\theta,\phi) = [I(\theta,\phi) - I_0(\theta)]/I_0(\theta)$ is calculated for display and analysis, and this is what is shown in Fig. 3.5. Here, $I(\theta,\phi)$ is the total photoemission intensity and $I_0(\theta)$ is the "primary" intensity which would result in the absence of scattering from neighboring atoms. These chi functions put equal fractional anisotropies on the same footing regardless of polar angle, resulting in automatic incorporation of corrections for instrumental response. Fig. 3.5 shows stereographic projections of the experimental 2π χ maps for Pt 4f (kinetic energy = 1414 eV), O 1s (956 eV), and Fe $2p_{3/2}$ (777 eV), with oxide coverages of 0.75 ML (left panels in (a)) and 1.0 ML (right panels in (b)). Intensities are given in a linear gray scale representation, with brighter meaning higher intensity. Each intensity map was measured over only one third of the hemisphere above the sample and then symmetry-reflected by exploiting the threefold symmetry of

the crystal to give the full 360° in azimuth. The total collection time for a set of data for Pt, O, and Fe was about 4-1/2 days for each coverage, with this time being significantly lengthened primarily due to using a ±3.0° tube array to better define angles and effective sample area. All three intensities were measured in sequence at each direction so that the final intensity maps are in exactly the same crystallographic orientation. The threefold data folding was justified for each case by comparing selected 360° azimuthal scans in the 2π intensity maps to full 360° experimental azimuthal scans at the same polar angles [Appendix B]; also of course, the LEED patterns showed threefold symmetry. These selected full azimuthal scan data and LEED patterns taken before and after XPD data collection also permitted us to verify that there were no noticeable changes in either the short-range or long-range order of the films, respectively, during the XPD data collection. Relative XPS peak intensities for each element taken before and after XPD measurements also did not show any noticeable change. Thus, both the composition and the structure of these oxide films were stable over the rather long times needed for the XPD data collection, even though bulk FeO is relatively easily oxidized in air.

The LEED patterns taken for 0.75 ML and 1.0 ML coverages are almost identical implying the same long-range order, while STM images taken for both coverages show marked topographic differences, going from a columnar structure with defects to a smooth overlayer with a lateral superlattice as discussed before. Even though XPD is a short-range atomic order probe, the Pt, O, and Fe XPD patterns are almost identical for these coverages, in qualitative similarity with the LEED results. This includes the actual degree of anisotropy in the pattern, as measured by $\Delta I/I_{max} \equiv (I_{max} - I_{min})/I_{max}$ in %, which is found to be essentially the same for all patterns between 0.75 ML and 1.0 ML. For example, these values for the polar angle of 20° passing through the three strongest peaks for Fe $2p_{3/2}$ are ~50 % for both coverages. Thus, XPD implies that the

internal short-range structure in these two overlayers is the same, even though STM shows a quite different long-range structure. In the following discussion, we will focus on the XPD data for 1.0 ML coverage, as it represents a more ordered structure, although any conclusions concerning short-range structure will also apply to the 0.75 ML case.

The Pt 4f XPD patterns in Figs. 3.5(a) and 3.5(b) are dominated by the strong forward-scattering and interference effects that are well-known in single-crystal substrates [27-30]. These patterns are rich in structure, with for example, maxima along <110> near-neighbor directions at a polar angle of 55°. Also, strong forward scattering peaks are clearly shown at a polar angle of 35° and azimuthal angles rotated by 60° from the $<11\bar{2}>$ directions, corresponding to the $<\bar{1}\,2\bar{1}>$ directions. Additional lines of intensity and fine structure are also seen, and these also are familiar in high-energy emission from single crystals [31]. The relatively narrow bands of higher intensity across the Pt diffraction patterns are again due to forward-scattering along planes of atoms, and have been shown to be related to Kikuchi bands at energies above about 1 keV [32,33]. The Pt 4f XPD patterns of ~ 1 ML iron oxides on Pt(111) in Fig. 3.5 also do not show any noticeable changes compared to the pattern for clean Pt(111) (cf. Fig. 2.5) because the intensity modulation is dominated by scattering and diffraction in the bulk platinum.

The Fe $2p_{3/2}$ XPD results in Fig. 3.5 show a much simpler diffraction pattern, with only three strong forward-scattering peaks along the $<11\bar{2}>$ azimuths lying in the Pt(111) surface, but at a much different polar angle of 20° with respect to the surface. These three strong forward-scattering peaks are found within experimental error exactly along the $<11\bar{2}>$ azimuths. These peaks are not expected to show the 0.6° rotational mismatch with the substrate shown in both previous [5] and this STM studies because the angular resolution of our XPD data is only ~± 3.0°, and because there are in any

case two domains rotated by ±0.6° whose effects on peak rotation should cancel out if they are equally present on the surface. The azimuthal anisotropy of these peaks at θ = 20° furthermore has a large value of $\Delta I/I_{max} \approx 50$ % that indicates a highly ordered surface with a very high percentage of Fe atoms in the same bonding geometry leading to this forward scattering. These XPD data for Fe thus directly imply that there are atoms sitting above the Fe atoms along Pt $<11\bar{2}>$ azimuths with a bond angle of 20° from the surface. These Fe results thus suggest that the O layer terminates the surface.

Finally, the O 1s XPD patterns in Fig. 3.5 are featureless and do not show any strong forward-scattering peaks. There are very weak and broad features, with the overall shape of a hexagonal ring, at polar angles between 16° and 24°, but these show anisotropies of only ~12% or less. The O 1s data thus permit the final definite conclusion that the O atoms comprise the outermost layer of the oxide bilayer, with no scatterers between them and the detector.

XPD-Theoretical Simulations:

To test more quantitatively the validity of these qualitative conclusions based on the XPD data, we have carried out theoretical simulations within the single scattering cluster (SSC) model [34] of the Fe and O diffraction patterns. These calculations were carried out for the structural model of one ML of FeO(111) shown in Fig. 3.6. Here, we assume that the bilayer of FeO with (111) orientation consists of an outermost layer of O atoms and a second layer of Fe atoms, and that this is placed on top of the Pt(111) surface in a registry so that three strong forward scattering peaks in Fe emission data lie in exactly Pt $<11\bar{2}>$ azimuths, as required by the Fe data in Fig 3.5. The additional structural parameters of this model can be easily deduced from a combination of the STM data and the Fe and O XPD data. For example, the atomically-resolved STM

image shown in Fig. 3.4(a) shows that the topmost atoms have a nearest-neighbor distance of ~3.1 Å. On the other hand, the XPD data of Fe and O indicate that there are scatterers above the Fe atoms with bond angles of 20° from the surface. Simple trigonometry then leads to an estimated distance between the Fe and O layers in the oxide of 0.65 Å. In the SSC calculations, the Pt atoms were not included due to the weakness of backscattering at such high kinetic energies [35,36], and planar Fe and O layers were assumed for simplicity (i.e., we neglect any rumpling that might be expected over the superlattice). A single scattering approximation should be adequate for these XPD simulations (as compared to the more accurate multiple scattering), since there are only two effective layers of atoms involved, and thus no significant multiple forward scattering pathways over the range of emission angles studied here. The experimental and calculated Fe $2p_{3/2}$ patterns are shown in Figs. 3.7(a) and 3.7(b). The calculated XPD χ patterns are obtained the same way as the experimental ones to permit an one-to-one comparison. The agreement between experimental and theoretical XPD patterns is remarkably good, and extends even to the weaker dark bands around each stronger peak in intensity, and other aspects of the diffraction fine structure. The calculation thus reproduces both the dominant forward-scattering peaks, as well as various higher-order diffraction features. For comparison, we also show in Fig. 3.7(c) a calculated diffraction pattern for Fe $2p_{3/2}$ in which the separation between the O and Fe layers has been kept at that between adjacent (111) planes in bulk FeO: 1.25 Å. The forward scattering peaks here move to much higher angles with respect to the surface ($\theta \approx 35°$), and the agreement with experiment is much reduced. This demonstrates the high sensitivity of such XPD patterns to epitaxial surface structures.

In Fig. 3.8, we finally show experimental and theoretical diffraction patterns for O 1s emission from the geometry of Fig. 3.6, and there is again excellent agreement, with

theory reproducing the overall hexagonal shape seen in experiment at polar angles between 16° and 24°, and neither pattern showing any significant diffraction structure.

The XPD data have thus permitted clearly resolving the short-range-order structure of 1.0 ML of iron oxide on Pt(111) as follows: The nearest-neighbor distances of ~3.1 Å are the same for both Fe-Fe and O-O, and these are responsible for the six main spots in the LEED pattern. Oxygen occupies the topmost layer of the bilayer, but it is relaxed vertically inward by about 0.6 Å compared to the (111) plane of cubic FeO with the NaCl structure.

Although these combined XPD, STM, and LEED results have served to further clarify the structure of this monolayer of FeO, there is still one question to be answered regarding the binding sites of O with respect to the underlying Fe and Pt. Even though Fe does not have preferred binding sites with respect to Pt because of the incommensurate overlayer formed on Pt(111) (i.e. within the large unit cell, Fe sits approximately on hollow sites in some areas, on bridge sites in other areas, and is close on-top sites in another areas), O can have two different binding sites with respect to Fe while having the same atomic geometry as FeO(111). These two possible structures are shown in Figs. 3.9(a) and 3.9(b). In both figures, an FeO bilayer sits on top of Pt(111) with a 0.6° rotational mismatch so as to produce the Moiré pattern and superlattice, as first proposed by Galloway et al [5]. However, as viewed from each Fe atoms, trimers of O sit along Pt $<11\bar{2}>$ azimuths in Fig. 3.9(a) (see lower right corner of unit cell), while these trimers of O sit along azimuthal angles rotated by 60° from the Pt $<11\bar{2}>$ directions in Fig. 3.9(b) (again see lower right corner of unit cell). Figure 3.9(a) is in fact the structure first proposed by Galloway et al., but these two different structures cannot be differentiated by STM, since both would lead to the same kind of superlattice images. From the excellent agreement between our experimental and theoretical XPD data discussed earlier, we can conclude with certainty that the structure of Fig. 3.9(a) is

completely dominant, with negligible admixture of the structure of Fig. 3.9(b). The large unit cell and many different types of O-Pt geometries involved make it difficult to say definitively why the structure of Fig. 3.9(a) is so strongly favored. But one possible explanation is that some of the oxygen atoms within the large unit cell of Fig. 3.9(a) sit directly on top of atoms in the topmost Pt layer (again see lower right corner of unit cell), thereby providing extra interactions between them and leading to a lower total surface energy. For the structure of Fig. 3.9(b), oxygen atoms sit on top of second-layer Pt atoms in the corner of the unit cell, with less attractive interaction expected. More detailed quantum-chemical calculations would be needed to make this conjecture more quantitative. Whatever the reason, the difference in the total surface energy between the two structures must be large enough to strongly favor one of them near the 1 ML regime; however, this difference could be small enough to favor the other structure at higher coverages involving some oxide islands in subsequent layer(s), and we will see evidence for this for the case of a 1.50 ML oxide to be discussed in the next Chapter.

We finally discuss the possible growth mechanism of these thin oxide layers on Pt(111) in terms of the columnar structures seen in the STM image for the 0.75 ML oxide. We propose the following explanation of the columnar growth of the oxides: The iron oxide growth starts where the Fe sits in the lowest energy sites, probably threefold-hollow sites of Pt with maximum coordination numbers that occur between the corners of the large unit cell in Fig. 3.2(c). The oxide then continues to grow to the higher energy sites such as the bridge sites just adjacent to the threefold-hollow sites, and can grow along a column in a zigzag fashion that oscillates between threefold and bridge. The highest-energy sites would probably be the on-top sites at the corners of the unit cell, with these perhaps being occupied last along the edges of a column. It is also interesting to note that the oxide columns in Fig. 3.3(a) have widths of approximately 35 Å, which is about 1.5 units cells in width, making it appear that this is the basic

growth unit. In this model, the oxides could grow in a columnar fashion with three different orientations of equal probability 120° degrees apart, perhaps explaining the streaked satellite spots in the LEED patterns of Fig. 3.2(a). One of the three possible columnar orientations is shown in the STM image of Fig. 3.3(a). We have also carried out model single-scattering calculations of the LEED patterns expected for this FeO superlattice, including a reduction in the diameter and width of its domains so as to finally simulate the columnar growth. The methodology and results of this LEED analysis are presented in Appendix C, and they qualitatively support the model proposed here. However, a more detailed investigation of submonolayers of iron oxides are needed to determine the growth mechanism and its influence on the streaked LEED satellite spots.

In summary, our structural model for 1 ML of FeO on Pt(111) fundamentally agrees with the FeO bilayer superlattice proposed by Galloway et al. [5], but adds to this picture that oxygen forms the outermost layer, that the Fe-O interlayer distance is significantly contracted, and that the oxygen atoms sit along Pt $<11\bar{2}>$ directions as viewed from their nearest-neighbor Fe atoms. In fact, several previous studies [37] have reported the existence of a monolayer of FeO either at a surface or at an interface between a metal and an oxide before growing Fe_3O_4 or Fe_2O_3 , even though bulk FeO is not an equilibrium crystal at room temperature according to the Fe-O bulk phase diagram [38]. In the present case, it seems quite reasonable that one ML of FeO/Pt(111) can be stabilized by reducing its polar surface instability due to the net electric dipole moment perpendicular to the surface, through both a slight lateral expansion of ~0.06 Å in its unit cell dimensions and a rather large inward relaxation by about 0.6 Å. These relaxations result in an Fe-O bond length of ~1.90 Å that is ~0.25 Å shorter than that of bulk FeO (2.15 Å), but very close to that of the octahedrally-coordinated atoms in bulk

Fe_3O_4 (1.88 Å). Thus, from the point of view of both FeO(111) polarity and Fe-O bond length, the structure we have found for this FeO monolayer is perfectly reasonable.

3.3. CONCLUSIONS

For the first time, three complementary surface structure probes, LEED, STM, and XPD, have been combined in a single instrument. This system has been utilized to study the structure of thin iron oxide films grown on Pt(111). We have demonstrated the complementary nature of these three techniques for providing a complete picture of the three-dimensional structure of this epitaxial oxide. We conclude that 0.75 ML and 1.0 ML iron oxide films on Pt(111) show essentially identical short-range atomic structure, even though the long-range order as judged by STM is different for the two, with STM revealing columnar growth and some empty regions for the 0.75 ML oxide. XPS quantitative analysis, as well as comparisons to standard XPS spectra, show that the Fe:O stoichiometry of these thin oxides is 1:1, and that the Fe $2p_{3/2}$ binding energy also is consistent with FeO. For both coverages, XPD also shows a topmost oxygen layer relaxed significantly inward by 0.6 Å compared to bulk FeO(111), while STM and LEED show an incommensurate oxide film with short-range and long-range periodicities of 3.1 Å and 26 Å, in agreement with prior work. We have also shown that the oxygen stacking in the FeO(111) bilayer is dominated by one of two possibilities, and this is the first time that this particular feature of the structure has been discussed.

Table 3.1. The results of XPS quantitative analysis.

Initially deposited Fe coverages determined by QCM and XPS before oxidation and Fe:O stoichiometry after oxidation determined by XPS quantitative analysis.

Fe (ML) by QCM	Fe(ML) by XPS Before Oxidation	Fe:O Stoichiometry After Oxidation
0.75	0.67	1 : 1.07 (=$FeO_{1.07}$)
1.00	0.93	1 : 1.08
1.25	1.25	1 : 1.12
1.50	1.62	1 : 1.16
1.75	1.82	1 : 1.25
3.00	3.64	1 : 1.39 (=$Fe_3O_{4.13}$)

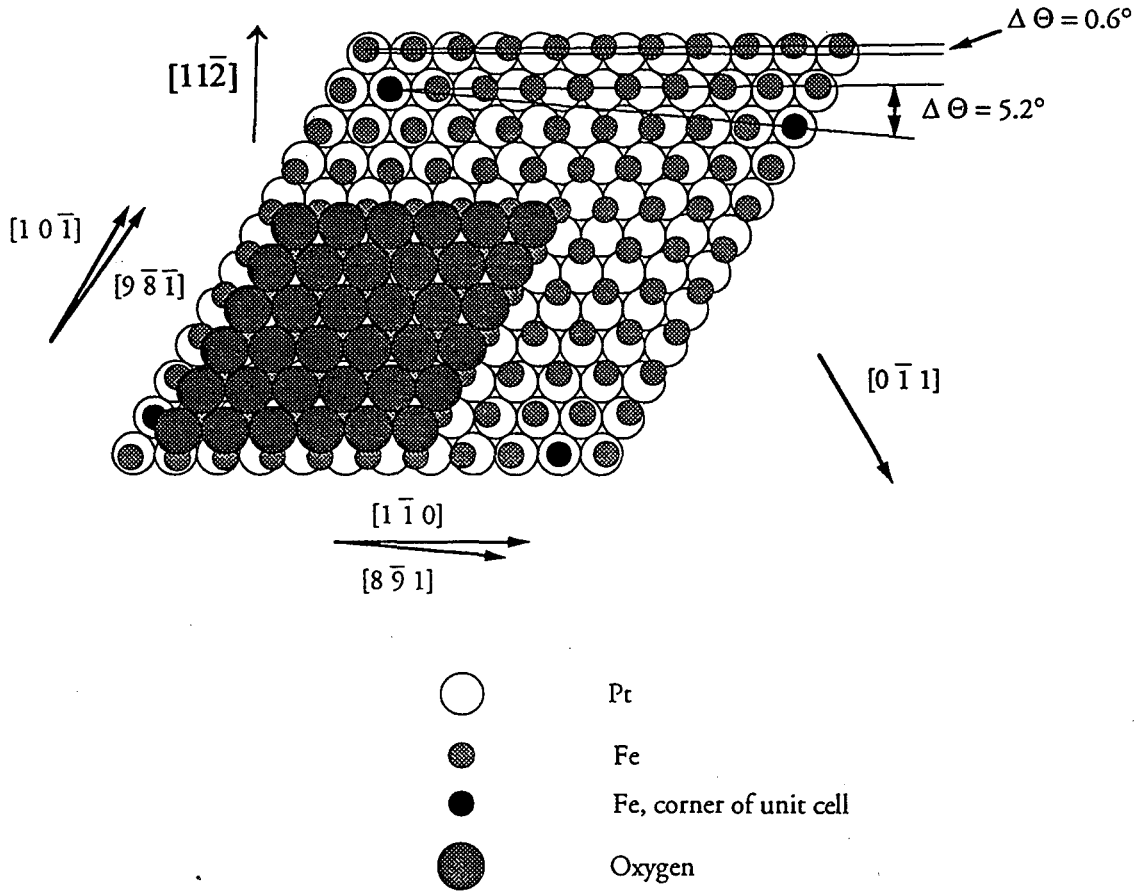

Figure 3.1. Structural model for the bilayer of FeO(111) on Pt(111) proposed in ref. [5]. Only a portion of the oxygen atoms in the top layer are shown for clarity. The oxygen termination of the surface was suggested in this study, but could not be experimentally verified. Also notice the 0.6° rotational mismatch between the overlayer and the Pt substrate, which in turn leads to a 5.2° mismatch between the lateral superlattice and the substrate.

Figure 3.2. (a) and (b) LEED patterns taken at 54 eV incident energy for 0.75 ML and 1.0 ML of FeO on Pt(111). These patterns are almost identical for both coverages, implying almost the same long-range atomic geometries for both films. Each one shows a three-fold symmetric pattern where each of the six principal "hexagonal" spots is surrounded by a rosette of six satellite spots. (c) The suggested atomic geometry for this FeO monolayer [From ref. 5.], with the Moiré pattern resulting from the overlay of the Pt(111) surface and the first atomic layer of an FeO(111) bilayer on top of it. This superlattice of FeO(111) on top of Pt(111) is thought to be responsible for the satellite spots in the LEED pattern.

(a) 0.75 ML

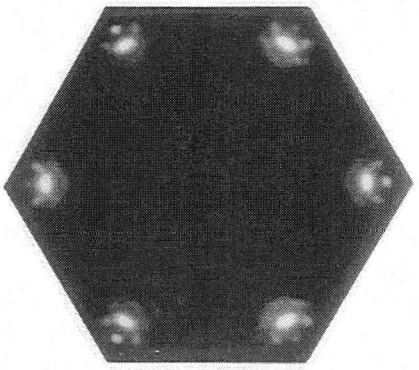

(b) 1.00 ML

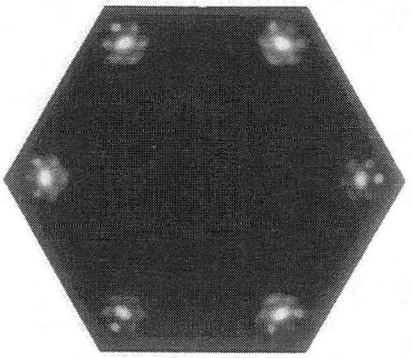

(c)

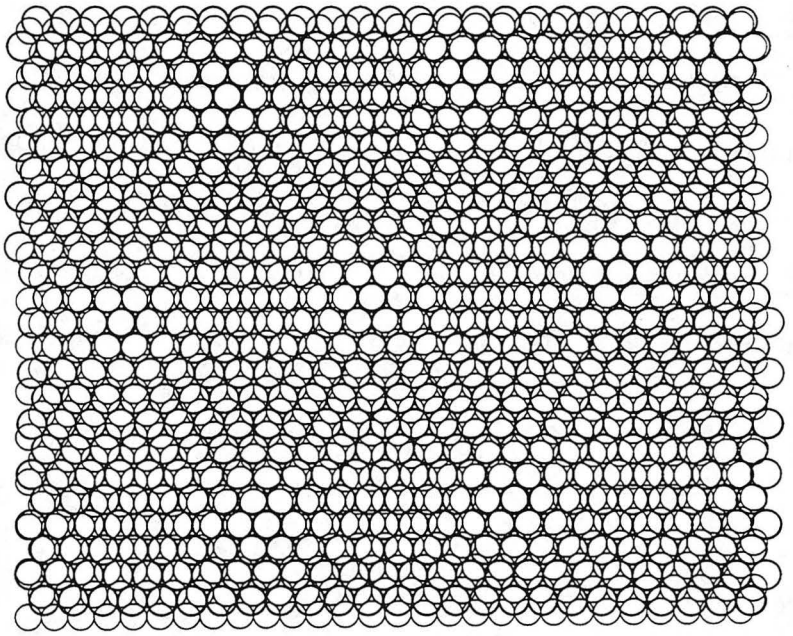

Figure 3.3. Large-area STM images taken in constant current mode for both 0.75 ML and 1.0 ML FeO/Pt(111): (a) A 320 nm x 320 nm image taken for 0.75 ML FeO shows some empty regions of about 25 % of the total area, and columnar oxide growth. The current is 2.0 nA and the sample bias voltage is 200 mV. (b) An 800 nm x 800 nm image taken for 1.0 ML FeO shows smooth terraces without any more evidence of columnar growth. The current is 2.46 nA and the sample bias voltage is 460 mV.

(a) 0.75 ML

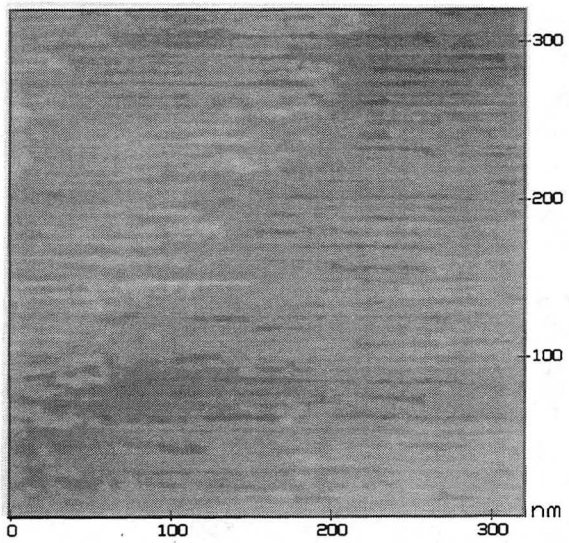

(b) 1.00 ML

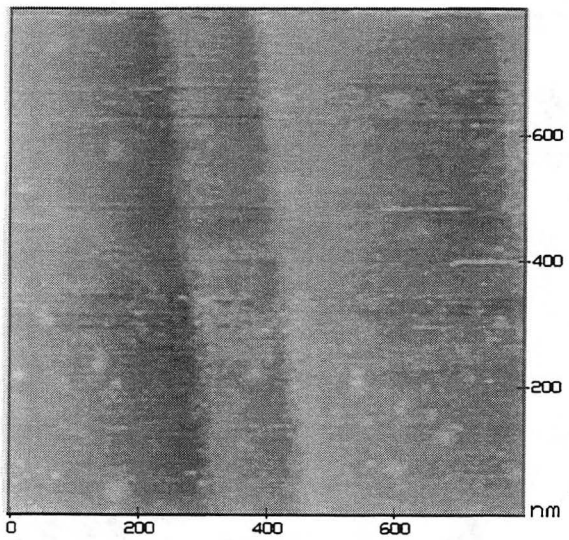

Figure 3.4. STM images for 1.0 ML FeO/Pt(111): (a) A 5.8 nm x 5.8 nm image taken in constant height mode and showing a hexagonal atomic periodicity of 0.31 nm = 3.1 Å that is further modulated with the larger periodicity of 2.6 nm = 26 Å. The average current is 1.36 nA and the sample bias voltage is 453 mV. (b) A 79.2 nm x 79.2 nm image taken in constant height mode and showing the periodicity of the large unit cell (~26 Å). The average current is 2.5 nA and the sample bias voltage is 436 mV.

(a)

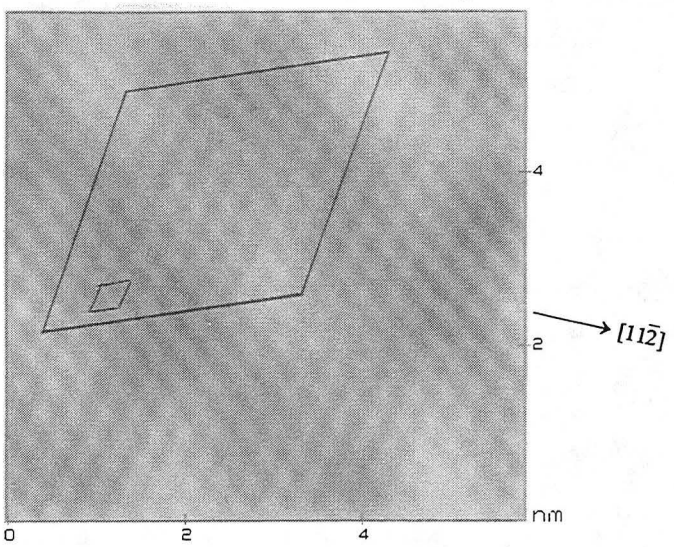

(b)

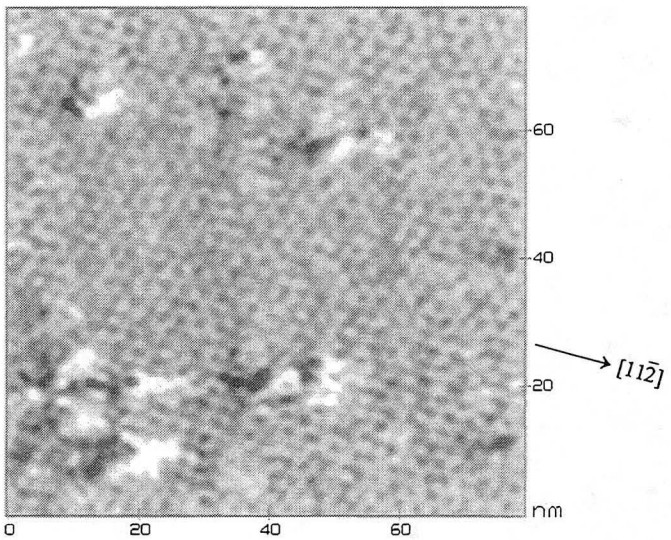

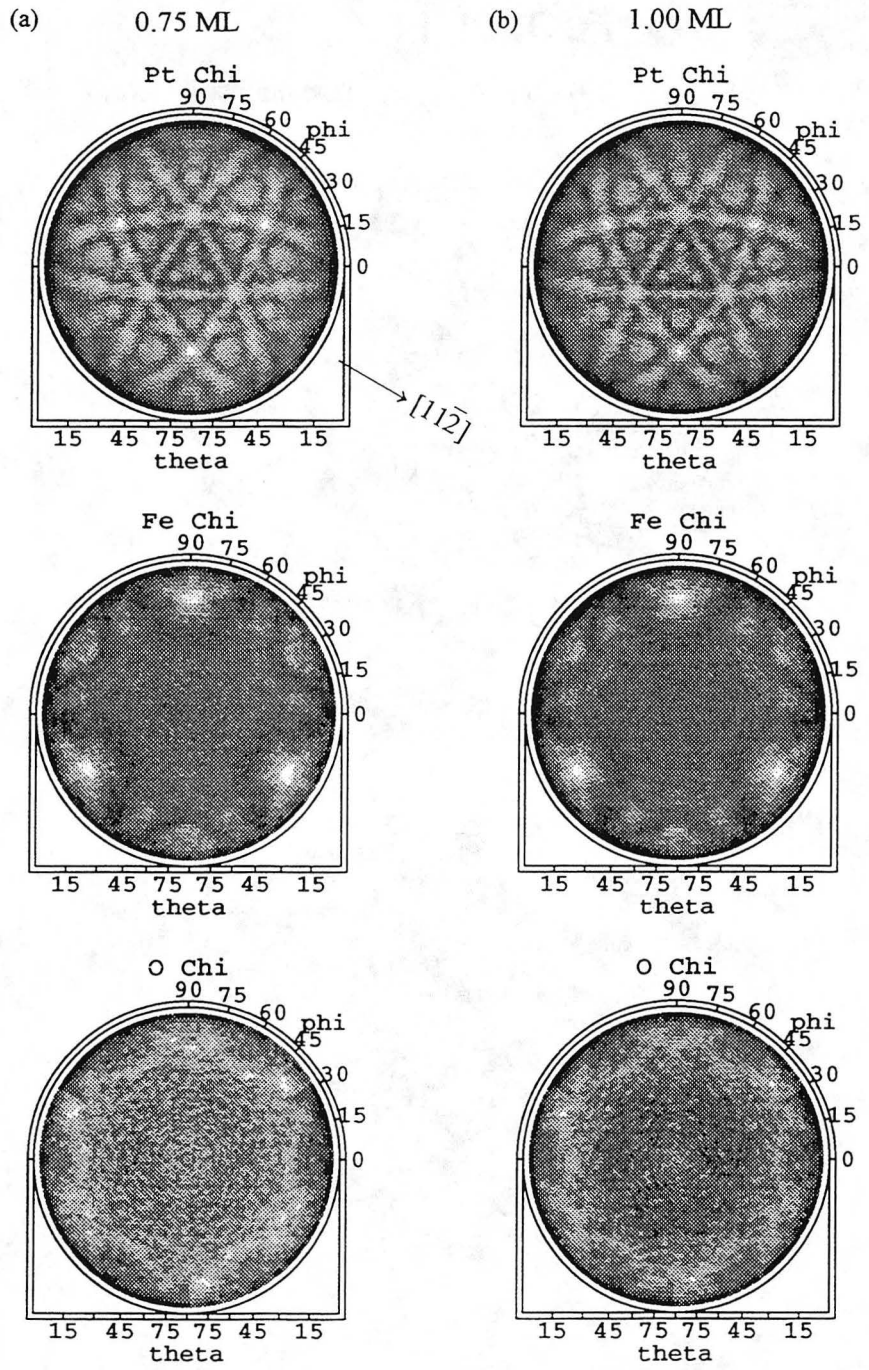

Figure 3.5. Stereographic projections of full 2π XPD chi patterns for Pt 4f, Fe $2p_{3/2}$, and O 1s emission from 0.75 ML (left panel, 5(a)) and 1.0 ML (right panel, 5(b)) of FeO on Pt(111). The nearly identical XPD patterns for both coverages imply that both oxides have the same short-range atomic geometries. Al Kα radiation (1486.7 eV) was used for excitation.

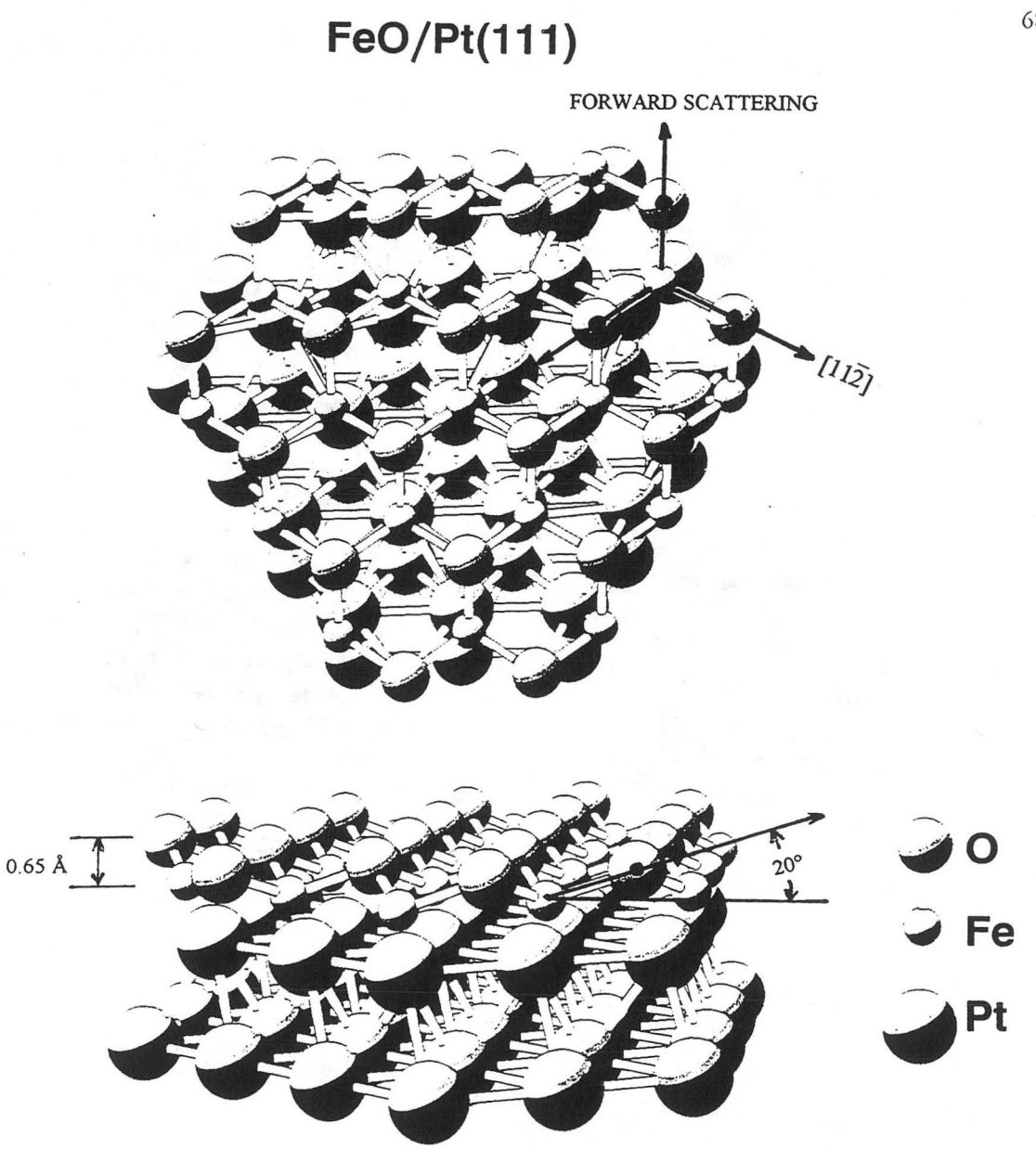

Figure 3.6. The atomic cluster used to theoretically model XPD data for 1.0 ML FeO/Pt(111). The topmost O layer is assumed to be relaxed inward by 0.6 Å compared to bulk FeO(111) to yield the forward scattering peak positions found for Fe in Fig. 3.5, and the FeO(111) bilayer to have a lateral hexagonal periodicity of 3.1 Å.

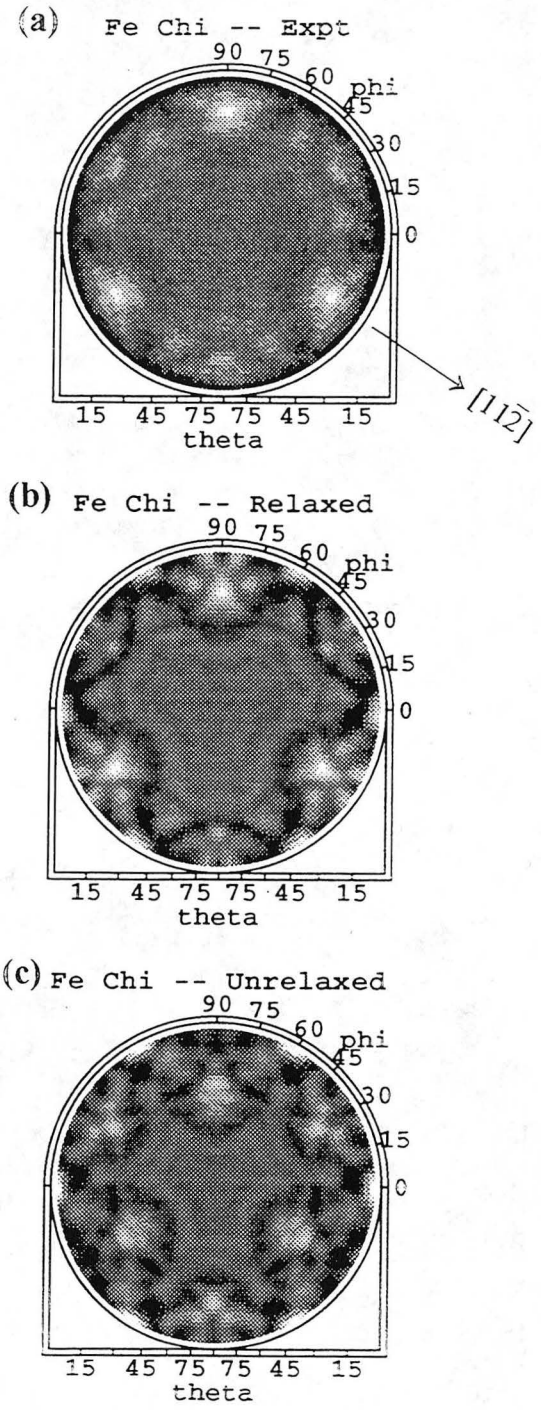

Figure 3.7. 2π XPD chi pattern for Fe $2p_{3/2}$ emission from 1.0 ML FeO/Pt(111), again in stereographic projection. (a) Experimental data. (b) Theoretical calculation using the cluster of Fig. 3.6. (c) Theoretical calculation using the cluster of Fig. 3.6, but with an Fe-O bilayer spacing of 1.25 Å such as that in bulk FeO.

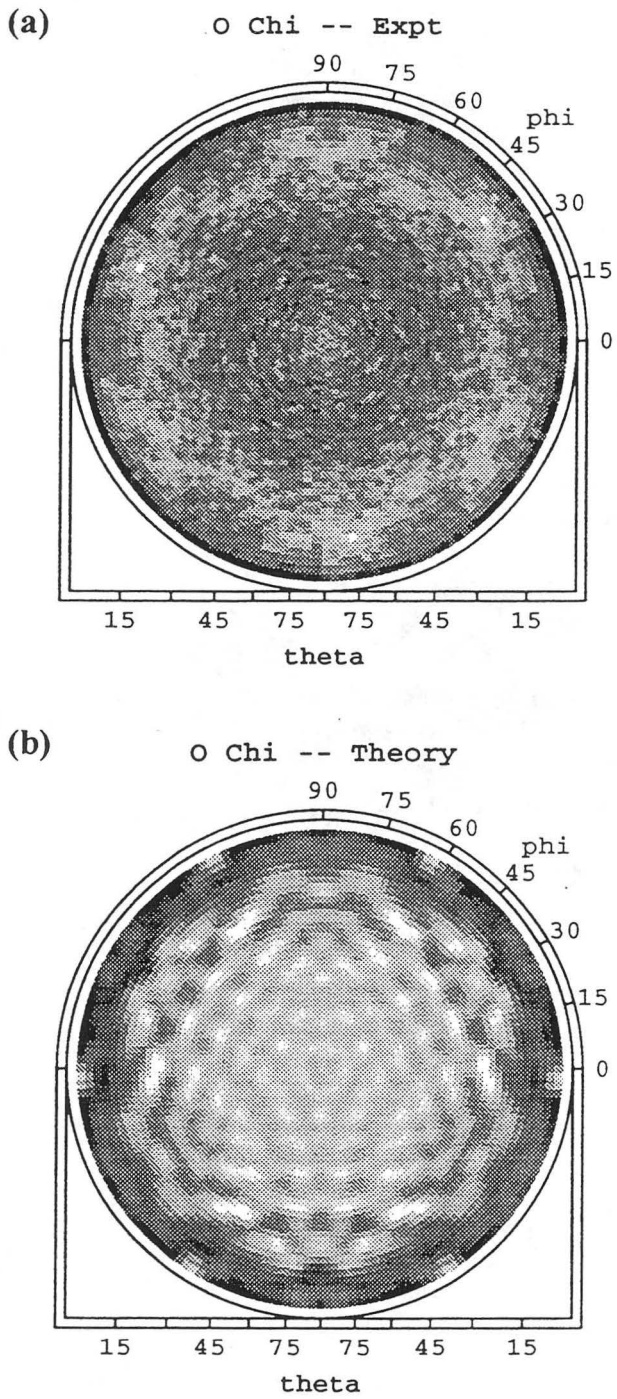

Figure 3.8. 2π XPD chi pattern for O 1s emission from 1.0 ML FeO/Pt(111), again in stereographic projection. (a) Experimental data. (b) Theoretical calculation using the cluster of Fig. 3.6.

(a)

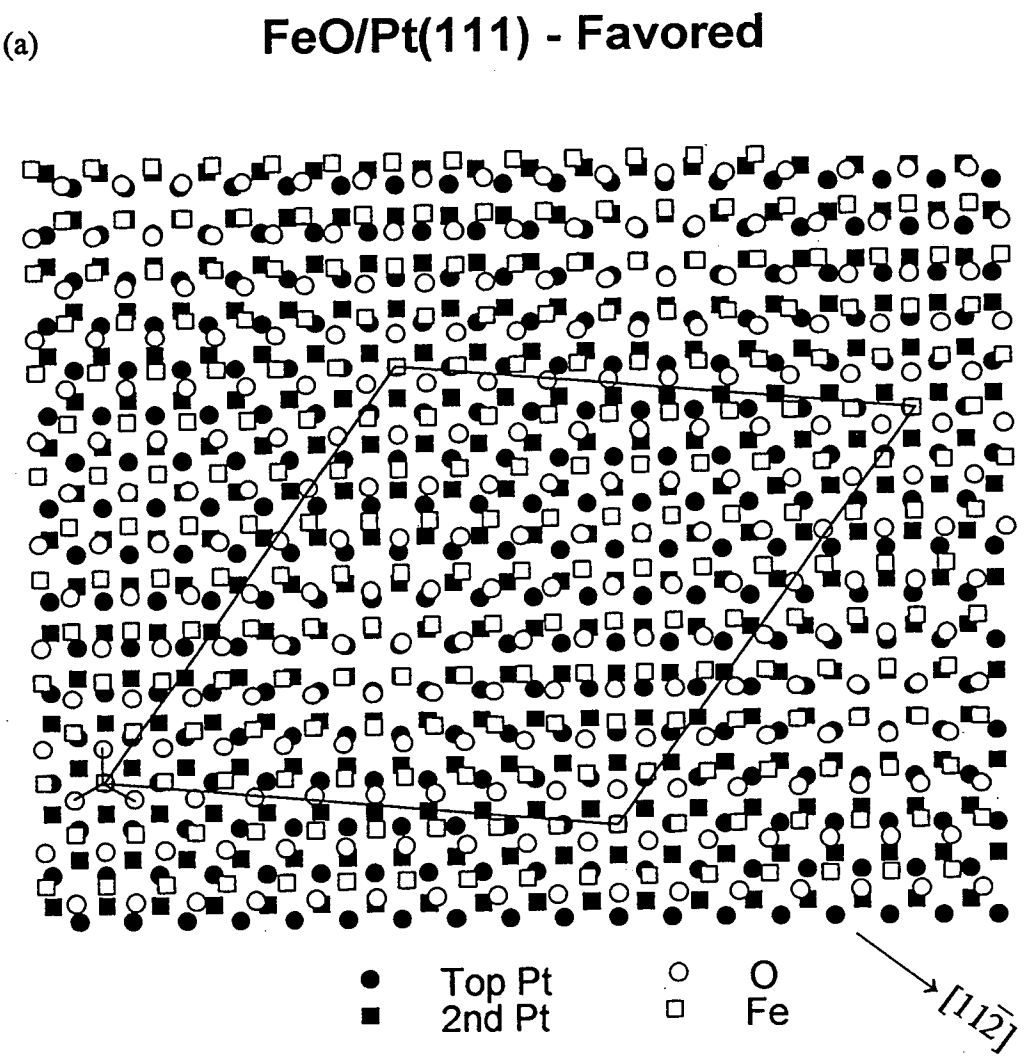

Figure 3.9. (a) The two different FeO bilayer structural models caused by the two different possibilities for stacking O with respect to Fe: As viewed from a nearest-neighbor Fe atom, O trimers sit along Pt <11$\bar{2}$> directions. Note that some O atoms sit on top of topmost Pt atoms near the corners of the large unit cell in 3.9(a), while there is no such coincidence in the large unit cell of 3.9(b).

(b) FeO/Pt(111) - Unfavored

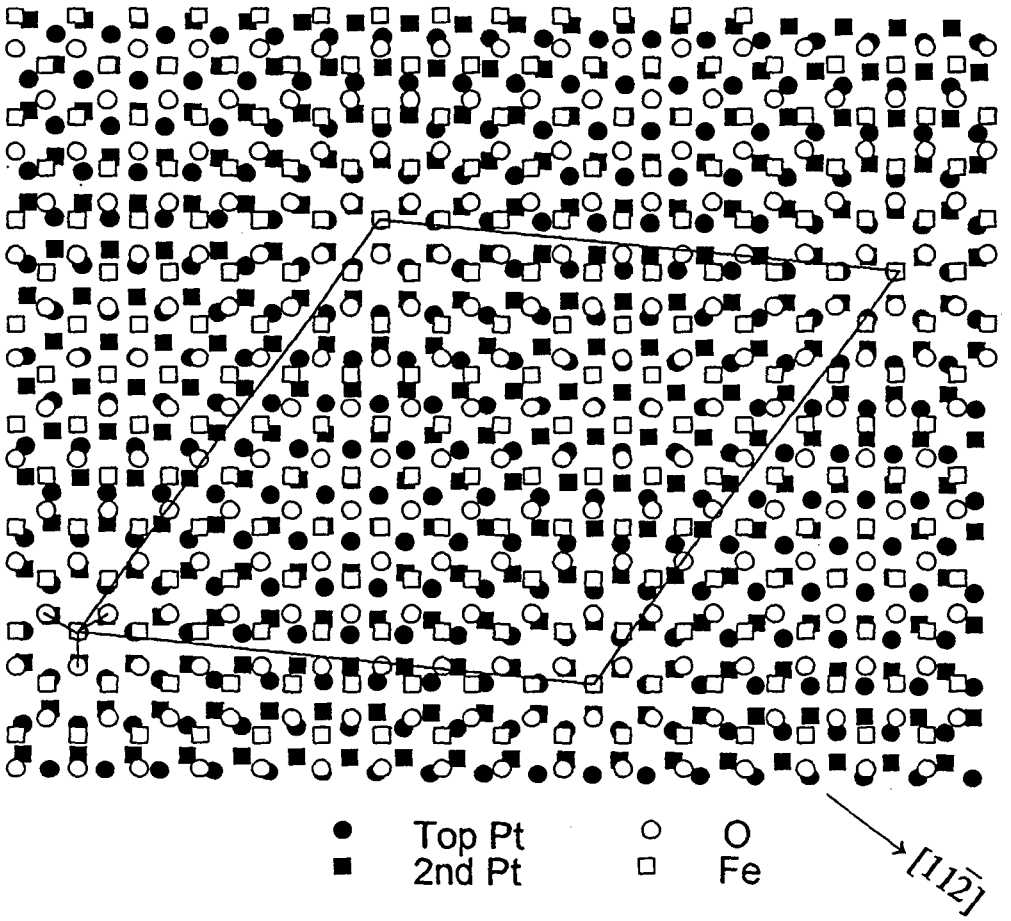

Figure 3.9. (b) The two different FeO bilayer structural models caused by the two different possibilities for stacking O with respect to Fe: As viewed from a nearest-neighbor Fe atom, O trimers sit along azimuthal angles rotated by 60° from the Pt <11$\bar{2}$>. Note that some O atoms sit on top of topmost Pt atoms near the corners of the large unit cell in 3.9(a), while there is no such coincidence in the large unit cell of 3.9(b).

REFERENCES

[1] V. Maurice, M. Salmeron, and G.A. Somorjai, Surf. Sci. 237, 116 (1990)

[2] M.C. Wu, J.S. Corneille, C.A. Estrada, J.W. He, and D.W. Goodman, Chem. Phys. Lett. 182, 472 (1991)

[3] G.H. Vurens, M. Salmeron, and G.A. Somorjai, Surf. Sci. 210, 129 (1988)

[4] G.H. Vurens, V. Maurice, M. Salmeron, and G.A. Somorjai, Surf. Sci. 268, 170 (1992)

[5] H.C. Galloway, J.J. Benitez, and M. Salmeron, Surf. Sci. 198, 127 (1993)

[6] W. Weiss, A. Barbieri, M.A. Van Hove, and G.A. Somorjai, Phys. Rev. Lett. 71, 1884 (1993)

[7] H.C. Galloway, J.J. Benitez, and M. Salmeron, J. Vac. Sci. Technol. A12, 2302 (1994)

[8] S.J. Tauster, Acc. Chem. Res. 20, 389 (1987)

[9] G.L. Haller and D.E. Resasco, Adv. Catal. 36, 173 (1989)

[10] K.J. Williams, A.B. Boffa, J. Lahtinen, M. Salmeron, A.T. Bell, and G.A. Somorjai, Catal. Lett. 5, 385 (1990)

[11] H.C. Wang, D.F. Ogletree, and M. Salmeron, J. Vac. Sci. Technol. 9, 853 (1991)

[12] M.J. Bennett, in High Temperature Corrosion, edited by R.A. Rapp (NACE, Houston, TX), 145 (1983)

[13] R.F.C. Farrow, G.R. Harp, R.F. Marks, T.A. Rabedeau, M.F. Toney, D. Weller, and S.S.P. Parkin, J. Cryst. Growth 133, 47 (1993)

[14] B.A. Pint, Mat. Res. Soc. Bull. 19, 26 (1994)

[15] S. Taniguchi, T. Shibata, and K. Takeuchi, Mat. Trans. JIM 32, 299 (1991)

[16] F.S. Ohuchi and M. Kohyama, J. Am. Ceram. Soc. 74, 116 (1991)

[17] S. Yoshii, O. Ishii, S. Hittori, T. Nakagawa, and G. Ishida, J. Appl. Phys. 53, 2556 (1982); E. Kay, R.A. Sigsbee, G.L. Bona, M. Taborelli, and H.C. Siegmann, Appl. Phys. Lett. 47, 533 (1985); S.S.P. Parkin, R. Sigsbee, R. Felici, and G.P. Felcher, Appl. Phys. Lett. 48, 604 (1986); A. Aeschlimann, G.L. Bona, F. Meier, M. Stampanoni, G. Zampieri, and H.C. Siegmann, Appl. Phys. Lett. 49, 824 (1986)

[18] C.R. Brundle, T.J. Chuang, and K. Wandelt, Surf. Sci. 68, 459 (1977)

[19] K. Asami, K. Hashimoto, and S. Shimodaira, Corrosion Sci. 16, 35 (1976)

[20] W.A. Fraser, J.V. Florio, W.N. Delgass, and W.D. Robertson, Surf. Sci. 36, 661 (1973)

[21] C.S. Fadley, Prog.in Surf. Sci. 16, 275 (1984)

[22] R.E. Connelly, C.S. Fadley, and J. Orders, J. Vac. Sci. Technol. A 2, 1333 (1984)

[23] P. Alnot, J. Olivier, and C.S. Fadley, J. Electron Spectorsc. Relat. Phenom. 49, 159 (1989)

[24] H.K. Bowen, D. Adler, and B.H. Auker, J. Solid State Chem. 12, 355 (1975)

[25] C.S. Fadley in Electron Spectroscopy: Theory, Techniques, and Applications (C.R. Brundle and A.D. Baker, eds), Vol. 2, Chap. 1, Academic Press, London (1978)

[26] P. Dierckx, J. Comput. Appl. Math. 1, 165 (1975), and program written by S. Ruebush in our group to apply this method to XPD data.

[27] S. Kono, C.S. Fadley, N.F.T. Hall, and Z. Hussain, Phys. Rev. Lett. 41, 117 (1978)

[28] S. Kono, S.M. Goldberg, N.F.T. Hall, and C.S. Fadley, Phys. Rev. Lett. 41, 1831 (1978)

[29] W.F. Egelhoff, Phys. Rev. B30, 1052 (1984); M. Sagurton, E.L. Bullock, and C.S. Fadley, Phys. Rev. B30, 7332 (1984)

[30] H.C. Poon and S.Y. Tong, Phys. Rev. B30, 6211 (1984)

[31] J. Osterwalder, T. Greber, A. Stuck, and L. Schlapbach, Phys. Rev. B44, 13764 (1991)

[32] R. Trehan, J. Osterwalder, and C.S. Fadley, J. Electron Spectrosc. Relat. Phenom. 42, 187 (1987)

[33] N. Naumovic, A. Stuck, T. Greber, J. Osterwalder, and L. Schlapbach, Phys. Rev. 47, 7462 (1993)

[34] D.J. Friedman and C.S. Fadley, J. Electron Spectrosc. Relat. Phenom. 51, 689 (1990)

[35] M. Sagurton, E.L. Bullock, and C.S. Fadley, Phys. Rev. B30, 7332 (1984)

[36] M. Sagurton, E.L. Bullock, C.S. Fadley, Surf. Sci. 182, 287 (1987)

[37] V.S. Smentkowski and J.T. Yates, Jr., Surf. Sci. 232, 113 (1990); and references therein

[38] A. Muan, AM. J. Sci. 256, 171 (1958)

[39] V.E. Henrich and P.A. Cox, The Surface Science of Metal Oxides, Cambridge University Press, Cambridge, 1994

CHAPTER 4

THICKER LAYERS OF FeO_x ON Pt(111)

4.1 INTRODUCTION

In this section, we now consider the growth of thicker layers of iron oxide on Pt(111), up to a total coverage corresponding to 3.0 ML of Fe before oxidation. For such growth of thicker epitaxial layers, three classic growth modes have been discussed depending on the types of two-dimensional and three-dimensional order present. The Frank-van der Merwe (FvM) mode designates systems where layers grow one at a time in perfect two-dimensional order. The Stranski-Krastanov (SK) mode corresponds to the formation of a first monolayer with good two-dimensional order followed by three-dimensional cluster or island growth on top of this. Finally, the Vollmer-Weber (VW) mode describes systems that form three-dimensional clusters or islands from the start [1]. By now, these categories have been shown to be oversimplified descriptions of the actual growth modes when compared to the varieties of structures that are actually seen (e.g., in STM). There are a variety of techniques that can give information about the surface structure of thin films, but STM and XPD are particularly well suited because of the complementary local real space information that they provide. STM is especially useful for resolving issues of growth topography and island size, while XPD can provide the internal atomic structure of the overlayer. We have thus applied these two methods, together with LEED, to the present problem.

The iron oxides vary in stoichiometry from FeO = $Fe_{1.0}O_{1.0}$ to Fe_3O_4 = $Fe_{1.0}O_{1.33}$ to Fe_2O_3 = $Fe_{1.0}O_{1.5}$. Bulk FeO (wustite) forms in the NaCl structure with Fe^{2+} cations octahedrally coordinated to oxygen anions. However, it is always found to be deficient in iron, due to defect formation which is believed to be related to the easy oxidation of

Fe^{2+} ions, so the actual bulk stoichiometry is $Fe_{1.0}O_{1.05}$ (=$Fe_{0.95}O_{1.0}$). In addition, FeO is not in fact an equilibrium phase at room temperature in the Fe-O bulk phase diagram [2,3]. However, it has been shown that the stable surface structure of an oxide can be different from the stable bulk structure for some cases [4] including FeO, with one special case already being discussed in Chapter 3. The stable room-temperature phase of Fe_2O_3 is α-Fe_2O_3, which forms in the corundum structure with Fe^{3+} cations located in distorted oxygen octahedra of a rhombohedral lattice [3]. While FeO and Fe_2O_3 are anti-ferromagnetic, bulk Fe_3O_4, or magnetite, is ferromagnetic and has the cubic inverse spinel structure. In the structure of magnetite, the oxygen anions approximately form an fcc lattice and the iron cations occupy tetrahedrally-coordinated interstices (A-sites) and octahedrally-coordinated interstices (B-sites). The valence structure is $[Fe^{3+}]_{tet}[Fe^{3+}Fe^{2+}]_{oct}(O^{2-})_4$, where half of the Fe^{3+} are located on A-sites and the other half together with the Fe^{2+} ions are on B-sites. The electron spins of the A- and B-sublattices couple anti-ferromagnetically, leading to a net magnetization because of the different total magnetic moments of the two sublattices. A rapid exchange of valence electrons between localized states of octahedrally-coordinated Fe^{2+} and Fe^{3+} cations is believed to be responsible for the relatively high bulk electrical conductivity at room temperature [5]. Upon cooling, magnetite undergoes a Verwey transition at a temperature in the range of 115 - 124 K, where the electron hopping is frozen out and the crystal becomes insulating.

In spite of the very different crystal structures of the three iron oxides, they all can be viewed to a very good approximation as a stacking of close-packed oxygen layers with Fe occupying interstitial sites along [111] directions for both FeO and Fe_3O_4, and interstitial sites along [0001] directions for α-Fe_2O_3. The oxygen stacking is thus cubic ABCABC stacking in the cases of FeO and Fe_3O_4, and hexagonal ABAB stacking in the case of α-Fe_2O_3. Possible bulk arrangements with Fe layer terminated of these iron

oxide structures are shown in Fig. 4.1, in which a close-packed oxygen layer (open circles) and the iron cations on either side of it (shaded circles) are indicated. The exposed surfaces are here (111) for both FeO and Fe_3O_4 and (0001) for α-Fe_2O_3. The bulk O-O distance is only slightly different for the three crystals: 3.04 Å for FeO, 2.97 Å for Fe_3O_4, and 2.90 Å for α-Fe_2O_3. The bulk Fe-O distances are 2.15 Å in FeO, 1.88 Å for A-sites and 2.07 Å for B-sites in Fe_3O_4, and 1.68 - 1.99 Å for α-Fe_2O_3. Due to the different positions of the iron cations, three different two-dimensional cells for these oxides are formed provided surface reconstruction can be ruled out: (1x1) for FeO, (2x2) for Fe_3O_4, and $(\sqrt{3}x\sqrt{3})R30°$ for α-Fe_2O_3; these are indicated in Fig. 4.1. Even though these three different unit cells would give rise to different LEED patterns if the surface were terminated in the bulklike way shown in the figure, they all have overall threefold symmetric structures like the underlying Pt(111) surface (cf. the XPD pattern in Fig. 2.5).

Several studies of bulk iron oxides have shown that they can be converted from one to another by heating in different partial pressures of oxygen, especially in the near-surface layers [6-8]. Studies on bulk single crystals of α-Fe_2O_3(0001) indicate that this surface forms different structures depending on the annealing temperature [9,10]. In particular, prolonged annealing produces a surface structure thought to be Fe_3O_4(111) [11,12]. Studies of bulk Fe_3O_4(001) do not report surface phases of different stoichiometry, but still show three different surface reconstructions [13]. Thus, the thin layers of epitaxial oxides under consideration here might be expected to show facile interconversion of structure type.

For thicker iron oxide layers grown on Pt(111), both LEED [12,14] and STM [15] studies report that Fe_3O_4 can be grown on Pt(111) by repeating the process of 1 ML iron oxide growth at an oxygen pressure of ~$4x10^{-6}$ Torr discussed in Chapter 2 several times (up to about 5 ML for the STM study and about 10 ML for LEED study). Both LEED

and STM studies further reported the structure of these thick iron oxide films to be Fe_3O_4 with (111) orientation and an outermost layer that is terminated with 1/4 ML of Fe. Furthermore, fairly large changes in the vertical interlayer spacings of these films compared to bulk Fe_3O_4(111) were also suggested from a LEED structural analysis, with STM also suggesting a Stranski-Krastanov growth mode. However, it has also suggested from STM results that α-Fe_2O_3(0001) can be grown if the oxygen pressure is raised to ~$5x10^{-4}$ Torr, illustrating the high sensitivity of the system to oxygen pressure [15].

We thus extended our study to thicker layers of iron oxide grown in the same manner on Pt(111) as discussed in Chapter 3. FeO_x film thicknesses from ~0.75 ML to ~1.75 ML in steps of ~0.25 ML, as well as ~3.0 ML were investigated using XPD, STM, and LEED in order to better understand the growth mechanism of these iron oxides, as well as their internal crystal structures.

4.2. EXPERIMENTAL

All experimental procedures are the same as described in Chapter 2. However, our growth method was different from those of prior LEED and STM studies [12,14,15] in being a single-step approach: we deposited the full thickness of Fe for a desired coverage, and then annealed at 980 K for about 1 minute in $4x10^{-6}$ Torr oxygen, rather than repeating this process for each ML of oxide several times as done previously.

4.3. RESULTS AND DISCUSSION

4.3.1. Chemical State, Coverage, and Stoichiometry

Figure 4.2 shows Fe $2p_{3/2}$ XPS spectra taken from iron oxide films with total Fe coverages of 1.0 ML to 3.0 ML. Pt 4f XPS spectra were also recorded for each coverage to avoid spurious shifts in the Fe $2p_{3/2}$ peak positions, and there were no detectable changes in these Pt binding energies (spectra not shown here). Binding energies are expressed relative to the Fermi energy. Both the inherently broad Fe $2p_{3/2}$ peak and our lack of high instrumental resolution (full width half maxima on Pt $4f_{7/2}$ = 1.7 eV with an analyzer pass energy of 100 eV) prevents us from resolving the Fe^{2+} and Fe^{3+} species present clearly. Indeed, even in prior higher-resolution studies of the iron oxides (e.g., with monochromatized Al Kα radiation on Fe_3O_4 powder), it has not been possible to distinguish these two species [16]. The Fe $2p_{3/2}$ peak maximum for 1 ML FeO is positioned at a binding energy (BE) of 709.6 eV, in agreement with that for an Fe^{2+} species reported earlier [16]. Furthermore, the Fe $2p_{3/2}$ peaks move toward higher BE as coverage increases. This shift is about 1.1 eV from 1.0 ML to 3.0 ML of iron oxide, and is somewhat less than the 1.5 eV which is reported between Fe^{2+} in FeO and Fe^{3+} in α-Fe_2O_3 by Brundle et al [16]. Our BE results for Fe are thus consistent with the expected coexistence of Fe^{2+} and Fe^{3+} in thicker iron oxide films on Pt(111), with Fe^{3+} increasing in relative amount, but probably not reaching the 100% of α-Fe_2O_3. This coexistence of two different iron chemical states will be further supported by XPS quantitative analysis, STM images, and the results of theoretical simulations of XPD results for 3.0 ML films. The corresponding BE's in O 1s XPS spectra over the same oxide coverage range (not shown here) show only very small and non-systematic shifts of $\leq \pm 0.1$ eV, consistent with prior observations on oxides of several transition metals

including Fe that O 1s BE's [16-19] are not sensitive to the oxidation state of the cations present.

The coverages of Fe as initially deposited before oxidation determined by QCM and by XPS quantitative analysis using Fe $2p_{3/2}$: Pt 4f intensity ratios are in good agreement with each other ($\leq \pm$ 20 %), and this agreement also extends to the final oxide-layer coverages determined by STM, as will be discussed later as each case considered. The coverages of initially deposited Fe as determined by QCM and XPS analysis and the Fe:O stoichiometries from XPS after oxidation are shown in Table 3.1. The final Fe:O stoichiometry of the oxide films as determined from XPS ranges from $Fe_{1.0}O_{1.1}$ = $Fe_3O_{3.4}$ at 1.25 ML to $Fe_{1.0}O_{1.4}$ = $Fe_3O_{4.1}$ at 3.0 ML, with the former suggesting FeO (as noted in the last section) and the latter Fe_3O_4. These changes in Fe:O stoichiometry as the coverages increase will also prove to be consistent with our STM and LEED data for these surfaces.

As discussed in Chapter 3, we compare O 1s:Fe $2p_{3/2}$ peak intensity ratios obtained from oxide films by analyzing the full 2π intensity maps to those of different iron oxide powder samples in order to determine stoichiometry. The θ-dependent O:Fe peak intensity ratios of 1.0 ML and 3.0 ML are shown in Appendix D. The ratio over the most reliable range near the surface normal of $60° \leq \theta \leq 90°$ is 0.67 for 1.25 ML, 0.69 for 1.50 ML, 0.74 for 1.75 ML, and 0.82 from 3.0 ML. The O:Fe peak intensity ratio for 3.0 ML (0.82) is very close to that of powder Fe_3O_4 (0.85) and much below that of powder Fe_2O_3 (1.03). The slightly higher value for Fe_3O_4 can easily be explained via adsorbed oxygen-containing species on the powder samples, as discussed in Chapter 3. Thus, as the Fe coverage increases, three different aspects of our XPS results indicate that the oxide goes from FeO to Fe_3O_4 in stoichiometry: the binding energies move toward but do not quite reach those expected for Fe^{3+} (consistent with the expected mixture of Fe^{3+} and Fe^{2+} in Fe_3O_4), there is a continuous increase in the O 1s:Fe $2p_{3/2}$ intensity ratio,

and this ratio also yields in the limit of the 3.0 ML oxide a stoichiometry that is very close to that of Fe_3O_4 powder by both standard XPS quantitative analysis and O:Fe peak intensity ratio comparisons to various iron-oxide powder samples. This conclusion concerning the evolution of the oxide stoichiometry with coverage will be further supported by our STM and XPD data to be discussed below. A more precise determination of the degree of Fe^{2+}:Fe^{3+} mixing present in thicker layers of iron oxide would be helpful, but would require much higher-resolution XPS spectra, for example, using synchrotron radiation for excitation.

4.3.2. Atomic Structure

LEED:

Fig. 4.3 shows LEED patterns of FeO_x films grown on Pt(111) for iron oxide coverages from ~1.25 ML to ~3.0 ML. Up to 1.75 ML, these LEED patterns are very similar to those shown previously in Fig. 3.2 for ≤ 1.00 ML of FeO, with the exception that the hexagonal superlattice satellite spots actually get sharper and more uniform in shape for coverages above 1 ML. These LEED patterns thus imply that the dominant long-range structure of the iron oxide films is almost the same up to about 1.75 ML coverage as that of 1 ML FeO/Pt(111). Interpreting these LEED data in a qualitative way further suggests that the FeO superlattice structure might actually be more ideal when the coverage is increased somewhat above 1.0 ML. For the thickest iron oxide film we studied (3.0 ML), the superlattice satellite spots disappear, and a fuzzy (1x1) LEED pattern suggestive of reasonable order developed. This LEED pattern for 3.0 ML thus indicates that the incommensurate 1 ML FeO superlattice is no longer present, and that there is diminished long-range order compared to lower coverages. In addition, we

also observed very faint and streaked (2x2) LEED spots at this maximum coverage, even though they do not show in the photograph reported here. Such (2x2) LEED spots are consistent with previous LEED and STM studies [12,14-15] of what has been suggested to be an $Fe_3O_4(111)$ overlayer; Fig. 4.1 in fact shows one termination of this surface that would lead to (2x2) features. The LEED patterns obtained previously for a total 8 ML coverage by Barbieri et al. [12] and with a multiple deposition and oxidation procedure starting with 1 ML of Fe each time in fact gives sharper principle spots, and a better defined (2x2) pattern.

STM:

STM now permits confirming some of our prior conclusions and adding other dimensions to what we can say about the structure of these oxide layers. Large-scan STM images of FeO_x/Pt(111) for each of the coverages studied are shown in Fig. 4.4. The scan size, bias voltage, and data acquisition mode is given in each figure caption. Although the LEED patterns from 0.75 ML to 1.75 ML are almost identical, the STM images show marked new features as the coverage is increased even slightly above 1 ML. For example, the STM image in Fig. 4.4(a) of a 1.25 ML oxide film shows small islands growing on a generally flat base layer; these small oxide islands have grown preferentially near a step that is monatomic in height and oriented along the diagonal in the image. This image also shows small darker regions suggesting that the Pt surface is not completely "wetted" by the oxide for this coverage.

On the other hand, STM images for higher coverages 1.50 ML and 1.75 ML shown in Figs. 4.4(b) and 4(c), respectively, develop larger islands on the flat base layer, and these begin to coalesce for 1.75 ML. For 1.5 ML, the oxide has grown across one monatomic step in the middle of the image and no more empty regions are observed, indicating a

complete wetting of the Pt surface by the base layer of oxide at this coverage. The image for 1.75 ML also clearly shows multilayer growth, with islands of at least two levels being visible; by contrast, mostly one level of islands is observed for 1.50 ML. For 1.50 ML, the heights of the islands are about 4.6 Å and the area occupied by them is found to be about 26 % of the total area as computed from several large-area images. [Further details of our STM data analysis are given in Appendix E.]. For 1.75 ML, the oxide has grown with what are imaged in the STM as two different heights of the islands: a topmost set about 5.0 Å in height as measured from the islands just below and occupying about 5.5 % of the total area, and a lower set about 9.7 Å in height as measured from the flat base layer and occupying about 58 % of the total area. The vertical line along the right quarter of the image appears to be a set of four bunched monatomic steps, perhaps linked to the initial substrate topology. Step bunching in fact was found to increase on the clean Pt(111) surface as the number of oxidation and cleaning cycles was increased during the course of this study, even though only monatomic steps separating large terraces were seen for a fresh sample at the beginning of the experiments (cf. Figs. 2.2 and 2.3). Such step bunching could be due to surface roughening induced by the repeated cycles of oxidation and annealing of the Pt crystal and/or residual impurities present on the surface below the limit of about 1 % ML (for the case of C) that can be detected in our XPS analysis [20].

The fact that the LEED patterns for 1.75 ML are almost the same as those for 1 ML of FeO(111) also indicates that the flat base layer seen by STM for higher coverages is still the incommensurate oxide overlayer, and not the underlying Pt surface. This coexistence of the base FeO(111) bilayer and the overlying oxide islands is also confirmed by STM, as illustrated in the image obtained for a 1.75 ML oxide film shown in Fig. 4.5. Although slightly noisy in the upper half, the lower half of this image shows the larger unit cell about 26 Å on an edge that is characteristic of the superlattice (cf. the

image for 1 ML coverage in Fig. 3.4(b)), just adjacent to bright areas that are due to oxide islands formed above 1.0 ML coverage.

Thus, we see islands of about 4.6 Å and 9.7 Å height for these two cases as measured with respect to the base layer of oxide. These heights can be compared to the significantly smaller bulk repetition distances between (111) planes in FeO of 2.5 Å, and in Fe_3O_4 of 2.38 Å. Thus, the 4.6 Å islands have an apparent height that is about two interplanar distances, and the "double-height" 9.7 Å islands have an apparent height of four interplanar distances, with each distance corresponding to one bilayer of Fe and O in FeO for example. Changes in surface electronic densities of states and effective conductivity with lateral island size (the average diameters of islands are ~25 nm and ~70 nm approximately for 1.50 ML and 1.75 ML, respectively) and/or internal crystal structure (e.g. FeO versus Fe_3O_4) from one region of the surface to the other could cause these STM heights to differ from actual surface heights however. As one indication that the actual heights of these islands correspond to in the simplest choice of 1 bilayer and 2 bilayers of FeO, we have calculated the total Fe coverage on the surface by measuring the fractional areas covered by islands. Considering the islands height of ~5 Å as 1 bilayer of FeO islands (or 2 bilayers of FeO islands), the actual coverages of 1.50 ML and 1.75 ML are found to correspond to estimates from STM of 1.26 ML (~1.52 ML) and 1.63 ML (~3.43 ML), respectively. The STM-derived coverages for 1.50 ML are within typical error ranges for XPS analysis using either assumption, while the coverage of 1.75 ML is in reasonable agreement with the XPS results only if the 9.7 Å height islands are considered to consist of 2 bilayers of FeO_X, but deviate significantly from the XPS analysis by about 88 % if these islands are taken to be 4 bilayers in height. We thus conclude that both types of islands are probably bilayer in height, and that the anomalously high 9.7 Å value for 1.75 ML is due to changes in the surface density of states and local conductivity on these islands, as well as possible effects due to the tip

shape or atomic composition. Corroborating evidence for this conclusion comes from the fact that multiples of 4.8 Å step heights have been reported in a prior STM study of α -Fe_2O_3(0001) in which repeated cycles of Ar^+ bombardment and subsequent high temperature annealing were carried out [11]. In this study, these step heights were assigned to 2 bilayers of Fe-O in Fe_3O_4(111) , with the conclusion that α-Fe_2O_3(0001) has been reduced to Fe_3O_4(111) in the selvedge region by repeated cycles of ion bombardment and annealing. In summary, with this assumption concerning the oxide island heights, the total Fe coverages we have estimated from STM are found to be within ±10-15 % of those expected from QCM and XPS for all cases except 1.75 ML.

Finally, we consider the STM image for a 3.0 ML film shown in Fig. 4.4(d). This image is different from the others in showing even more marked multilayer growth and many smaller islands in the topmost layers. There are several levels of islands spanning at least four levels, with the topmost islands being about 26 Å from the lowest layer as measured in line-cut profiles using the STM software. The lowest (dark area) layer consists of small patches with sizes of about 10 nm in diameter, and is consistent with a Pt surface that is fully "wetted" by the oxide, as seen above for the 1.50 ML and 1.75 ML coverages. Measuring island heights is even more difficult for this multilayered structure, but it appears that all of the island heights are not exactly multiples of about 5 Å. However, the islands just on top of the lowest layer (darkest in the image), which have the largest total area, are found to have heights of about 5 Å as measured at several places in the image: this we again suppose be 2 bilayers of Fe-O. No patches with the base FeO bilayer were resolvable in this image, consistent with the absence of any superlattice spots in the LEED pattern, although we cannot rule out very small areas with insufficient extent to be visible in either STM or LEED. Thus, thicker oxides layers of 1.75 ML and 3.0 ML grow via multilayer stacks of oxide islands instead of layer-by-layer.

The wide-scan and narrow-scan STM images we have presented also permit better understanding the continuous increase in the O:Fe ratio and the shift of the Fe binding energy as Fe coverage increase (as seen in XPS), as well as the streaked satellite spots at 1 ML coverage or less (as seen in LEED). First, STM shows island growth on top of a 1 ML FeO base layer and these islands occupy more and more of the surface as coverage increases. These islands are expected to have a different atomic structure from the base layer, since the stoichiometry changes and there is also evidence of an increase in the fraction of Fe^{3+} species present. The final stoichiometry at 3.0 ML is also consistent with Fe_3O_4. Thus, we can postulate a change in the overall composition and structure of the oxide film from FeO to a mixture of FeO and Fe_3O_4 as thickness increases, with Fe_2O_3 being less likely on the basis of both stoichiometry and binding energy. We will later discuss the internal atomic structure of the islands in detail when XPD results are considered for each case. Second, we can qualitatively comment on the streaky LEED satellite spots shown in the 0.75 - 1.25 ML regime as follows. Fairly large STM images show some empty regions up to 1.25 ML coverages resulting in long-range structure less ordered compared to the higher coverages. Such incompletely wetting iron oxide overlayers up to 1.25 ML may cause the streakier satellite spots shown in Figs. 4.3 and 3.2. Going to higher coverages of 1.50 ML and 1.75 ML thus fully fills and orders the first-layer FeO superlattice and sharpens the LEED satellite spots, even though at the same time, significant oxide island growth on top of this superlattice has occurred.

Overall, we thus propose that the growth mechanism of iron oxide on Pt(111) for Fe coverages from 0.75 ML to 3.0 ML is Stranski-Krastanov in nature: iron oxide islands form on top of a 1 ML FeO bilayer that forms a superlattice. The same sort of growth mode for iron oxide grown on Pt(111) was also reported in prior STM studies in which the preparation procedure was varied so as to involve successive one-ML oxidations on top of one another instead of the one-shot procedure used here [15]. However, we

cannot from our STM data only determine whether the superlattice persists underneath the islands. The internal structure of the islands will be considered next using XPD experimental data and comparing them to theoretical simulations.

XPD-Experimental Results:

Fig. 4.6 shows stereographic projections of full-2π experimental XPD data: Pt 4f in (a), Fe $2p_{3/2}$ (b), and O 1s (c) for the same four Fe coverages from 1.25 ML to 3.0 ML. The data collection mode, threefold data folding, and method of calculating normalized chi functions from measured intensities are the same as described in Chapter 3.

As might be expected, the Pt 4f emission patterns up to 1.75 ML are almost identical and do not show any noticeable changes, since the intensity modulation from the bulk platinum diffraction is dominant. The six strongest peaks are due to two sets of three low-index forward scattering directions: nearest-neighbor scattering along [110] at a polar takeoff angle of 55° and in the $[11\bar{2}]$ azimuth, and next-nearest neighbor scattering along [010] at a polar angle of 35° and in an azimuth rotated by 60° with respect to the first. For a 3.0 ML oxide coverage, the basic patterns are the same as those of lower coverages, showing the strong nearest- and next-nearest- neighbor scattering features. However, all features are reduced in relative amplitude due to scattering in the overlying oxide, and for $\theta \leq 20°$ this is particularly pronounced, due to the longer path length for escape and the resulting enhanced inelastic attenuation and surface sensitivity.

By contrast, the Fe and O XPD data in Figs. 4.6(b) and 4.6(c) show pronounced changes as coverage is increased, going from relatively simple diffraction patterns at lower coverages to more complex ones at higher coverages. The diffraction patterns for 1.25 ML are essentially identical to those of 0.75 ML and 1.0 ML FeO, showing for Fe the three strong forward-scattering peaks along the same emission directions at a polar

angle of 20° and the same dark bands and fine structure around these peaks, and for O, the same weak and diffuse hexagonal ring at polar angles between 16° and 24° (cf. Fig. 3.5). The diffraction anisotropy for Fe for 1.25 ML, as measured at $\theta = 20°$ for the three strongest peaks, is $\Delta I/I_{max} \approx 48$ %, and agrees very well with the 50 % found at ~ 1.0 ML, implying that the relatively small islands developed at 1.25 ML as seen by STM have the same internal structure and/or are not numerous enough or well-ordered enough to contribute significantly to the overall XPD patterns. The Fe diffraction pattern for 1.50 ML coverage still shows the three strongest forward scattering peaks at the same polar angles of 20°, but the strongest of these peaks are rotated from the former Pt $<11\bar{2}>$ azimuths by 60° and the diffraction pattern starts to show additional features at higher polar angles (e.g., a sixfold set of peaks at the polar angle of ~ 58° with a lower anisotropy of ~ 12 % which were not present at 1.25 ML). For 1.75 ML, the strongest peaks in the Fe chi data rotate back to their original position in azimuth but remain at the same polar angle originally associated with the FeO bilayer superlattice, and the additional fine structure at higher polar angles continues to intensify. The rotated positions of the strongest peaks for 1.50 ML cannot be due to any mistake in plotting or data analysis, since the Pt, O, and Fe XPD data are simultaneously obtained along the same emission direction, with unchanging Pt diffraction pattern thus providing an unambiguous internal reference for azimuth. These rotated peaks furthermore appear to originate from the same FeO base layer seen by STM, because their polar angle is exactly the same as in the 1 ML case, corresponding to the O layer relaxing inward by 0.6 Å. One possible explanation for these results is that the increase in coverage from 1.25 ML to 1.50 ML causes through the interaction of the islands with the base layer a shift in the type of base layer formed from that favored at 1 ML (Fig. 3.9(a)) to that unfavored at 1 ML (Fig. 3.9(b)). This shift would not change the LEED pattern provided that the two types of base layer were formed in sufficiently large domains. As noted

previously, the favored and unfavored structures at 1 ML are almost identical structurally, with the only difference being the stacking of the O atoms with respect to underlying Pt atoms: thus, the perturbation of the base layer by the islands could lead to a stronger presence of the unfavored structure, with an apparent reversal of this effect on going to 1.75 ML. That the 1.50 ML structure may be more of a mixture of base layer structures, and thus also local Fe bonding and forward scattering geometries, is also suggested by the variation in anisotropy at $\theta = 20°$, from ~48 % for 1.25 ML down to ~32 % for 1.50 ML, and then back up again to ~38 % for 1.75 ML [See Appendix F for a more detailed presentation of this data.]. Even though we do not have any quantitative estimates for the surface free energies of these two base-layer structures, the differences between them could be large enough to favor one structure near 1 ML, but small enough to favor the other at higher coverages in the 1.5 ML regime. This point needs further investigation, including a consideration of the interactions between the base layer and the islands formed on top of the base layer, in order to determine whether there is such a driving force to the unfavored FeO structure. In any case, the strongest peaks in all of the Fe XPD patterns for coverages from 0.75 to 1.75 ML are well explained as being due to O atoms sitting above Fe atoms in an FeO bilayer, with two different stacking geometries probably being present near 1.50 ML.

The O XPD patterns also start to show new features as coverage increases from 1.25 ML, beginning at 1.50 ML with two sets of six weak peaks along what is the diffuse hexagonal ring at lower coverage and with a set of six weaker peaks at higher polar angles around 53° (anisotropy ~ 12 %), plus one along the surface normal. For 1.75 ML coverage, Fe emission still shows the strongest three peaks along the Pt $<11\bar{2}>$ directions (anisotropy of ~ 38 %), as well as new peaks developed at the polar angles around 36° (~ 16 %) and 60° (~17 %). O emission at 1.75 ML coverage also shows new features at polar angles around 34° (anisotropy ~ 13 %) and 54° (~14 %). Finally, for

3.0 ML coverage, both the Fe and O diffraction patterns are even more complex, but the basic features seen are already suggested at 1.75 ML. For Fe emission, the peaks at polar angles around 36°/38° and 62° have anisotropies of ~22 % and ~ 20 %, respectively, and for O emission, the peaks at polar angles around 34° and 54° have anisotropies of ~ 18 % and ~ 26 %, respectively. These peaks are all present at the lower coverages, but they produce lower anisotropies as described above, indicating the development of more short-range order in the oxide as 3.0 ML is approached. The generally lower anisotropies for Fe emission data in this coverage range as compared to data for one ML regime is no doubt due to the presence of more than one type of emitter in the thicker overlayers, since each structurally-inequivalent emitter contributes a different modulation to the overall XPD pattern; this summing over inequivalent emitters will be included in the theoretical modeling or our results to be done in the next section.

We will first discuss our overall XPD data for thicker oxide layers from a qualitative point of view, before going on to compare experiment with theoretical simulations. First, the Fe diffraction patterns for coverages up to at least 1.75 ML exhibit the strongest peaks along Pt $<11\bar{2}>$ azimuths and at a polar angle of 20°. These are clearly assignable to simple forward scattering in an FeO bilayer, as shown in our prior comparisons of experiment and theory for XPD patterns from ~ 1.0 ML FeO/Pt(111). The likely presence of a second type of oxygen orientation in the bilayer causes additional peaks to form along Pt $<\bar{1}\,2\bar{1}>$ azimuths at 60° away from those of the favored structure for 1.50 ML, but peaks associated with the favored structure are nonetheless present over the full range up to at least 1.75 ML. The base layer of FeO and its superlattice are evident in LEED, STM, and XPD up to 1.75 ML coverage, but is not visible when the coverage reaches to 3.0 ML. Second, both the Fe and O XPD patterns develop additional features at higher photoelectron takeoff angles on going to higher coverages, unlike the corresponding LEED patterns, which remain relatively

constant up to 1.75 ML. These new features in the XPD patterns can be easily explained in a qualitative way as being due to the multilayer stacks of oxide islands that are seen in STM to be forming on top of the flat base layer of FeO. Thus, both Fe and O can now have additional scatterers between them and the detector, producing more strong peaks in the XPD patterns at higher takeoff angles. Third, the overall XPD patterns change from being threefold symmetric in the 1 ML regime to being sixfold symmetric as the coverages increase. This suggests the equal presence of two domains of threefold oxide islands rotated by 180° with respect to one another. Interestingly, the O diffraction patterns for all higher coverages, including even 3.0 ML, are still at least slightly threefold in character, with a difference in anisotropy of the two sets of three peaks at a polar angle of around 54° of ~ 3 %; this was verified by doing full 360° azimuthal scans of both Fe and O intensities [See Appendix G]. This further suggests that the two threefold domains are not quite equally present. We will return to the question of azimuthal symmetries for both Fe and O later in comparing experiment with theoretical simulations. However, this symmetry change from threefold to sixfold indicates that the structure(s) of the multilayer stacks of oxides is(are) different from the simple one favored in the one ML oxides, involving both another crystal structure and stoichiometry (as already indicated by our XPS analyses), and threefold-symmetric oxide structures present in two domains with unequal coverage on the surface. Finally, as coverage increases, Fig. 4.6 clearly shows that both the Fe and O XPD data develop in a continuous way toward the pattern seen for 3.0 ML, even though more radical changes in long-range order (LEED) and topography (STM) are seen in passing from 1.75 ML to 3.0 ML. For example, there are six Fe XPD peaks at polar angles of about 56°-64° that are clearly present over the full coverage range from 1.50 ML to 3.0 ML, with only the polar angles changing slightly with coverage: peaks are centered at ~58/60° at 1.50 ML, ~62° at 1.75 ML, and ~62° at 3.0 ML. These six peaks are also already present weakly

at even 1.25 ML, at a polar angle of 58°. This aspect of the XPD patterns reveals that the short-range structure of the oxide islands for coverages above about 1 ML is already developing toward that of 3.0 ML. Because XPD inherently averages over all possible bonding sites, we will thus in the next section focus on analyzing the 3.0 ML XPD data as a limiting model for the internal structure of the islands seen by STM, and then comment qualitatively on the implications of this for the thinner oxide layers.

XPD-Theoretical Simulations:

We have carried out theoretical simulations of photoelectron diffraction patterns within a single scattering cluster (SSC) model [21] and also for one test case in a multiple scattering cluster (MSC) model [22]. For such thin layers and the high kinetic energies involved, we do not expect multiple scattering effects to be strong, as there are no long chains of scatterers for multiple forward scattering [23]. We comment at the end of this section on the MSC results, and they are presented in more detail in Appendix H. Both the Fe $2p_{3/2}$ and O 1s diffraction patterns have been considered for different possible structural models of a 3.0 ML iron oxide film on Pt(111), although any conclusions concerning short-range structure will also be expected to apply to the internal structure of the oxide islands above about 1.50 ML coverage. Due to computational time limitations, we have only in a few cases considered thicker or thinner oxide layers, even though STM suggests that they are present in the various island heights. The 3.0 ML calculations on which we finally focus for Fe_3O_4 thus are intended to represent the average seen in XPD. Due to the weakness of backscattering at such high kinetic energies [24] as discussed in Chapter 3, Pt atoms have not been included as scatterers in our calculations. All of the input parameters for the calculations are the same as discussed in Chapter 3. But unlike the case of an FeO(111) bilayer, where there

are only one Fe and one O atom in a (1x1) unit cell, treating thicker oxides of different stoichiometries and structures requires that all Fe and O atoms within the two-dimensional unit cell and in different layers inward from the surface which have different near-neighbor geometries be considered as emitters. For example, $Fe_3O_4(111)$ and α-$Fe_2O_3(0001)$ have (2x2) and ($\sqrt{3}$x$\sqrt{3}$) bulk unit cells, respectively, as shown in Fig. 4.1. In the unit cells of these three iron oxides, if only the outermost Fe and O bilayer is considered, there is one Fe emitter and one O emitter for FeO(111), three Fe emitters and four O emitters for $Fe_3O_4(111)$, and two Fe emitters and three O emitters for α-$Fe_2O_3(0001)$ [See detailed drawings in Appendix I.]. In general, each distinct emitter has a different local scattering geometry, as can be seen for the different emitters in Fe_3O_4 in Fig. 4.1. To reduce computation times, both Fe and O intensities were calculated over only 120° in azimuth, and then the full 2π intensity map was completed by exploiting the threefold symmetry of the structure in the same way as the experimental data.

We tested three different forms of multilayer iron oxide structures: FeO(111), α-$Fe_2O_3(0001)$, and $Fe_3O_4(111)$. All the structures tested have a bottom Fe layer next to Pt (although the Pt atoms were not present in the calculations) as in the case of one ML FeO/Pt(111). A first test group among the possible structures was different numbers of layers of FeO(111), up to 5 bilayers of Fe and O, a reasonable choice since we have conclusively shown in Chapter 3 that the first monolayer grows as an inwardly relaxed FeO(111) bilayer. Among the structural models tested in this group are: (1) two bilayers of FeO with the bulk interlayer distances between all layers, (2) two bilayers of Fe and O with the bottom bilayer relaxed inward as for 1 ML FeO/Pt, (3) the same as structure (2) but with the topmost O rotated 60° from Pt $<11\bar{2}>$ as in the case of the unfavored structure in Fig. 3.9(b), and (4) five bilayers of FeO with bulk interlayer distances. The structures from (1) to (3) were tested in order to see if they fit experiment for coverages

less than 3.0 ML, while (4) was aimed at the thick-island limit of a 3.0 ML oxide. The second group tested represented α-Fe_2O_3(0001) with 2 bilayers of Fe and O (AB stacking of O layers) and 3 bilayers of Fe and O (ABA stacking of O layers). The final group among the tested structures consists of several different structures for Fe_3O_4(111), including a detailed structure reported recently on the basis of a LEED IV analysis using multiple scattering theory [12,14].

The structures tested for Fe_3O_4(111) were the most complex, and we review their geometries here briefly. Fig. 4.7 shows the general type of structure that finally best fit our data for 3.0 ML oxide on Pt(111): it consists of three bilayers of Fe and O (with ABC stacking of the O layers). In this figure, the surface is shown to be terminated with 1/4 ML of Fe (as measured with respect to O), as suggested by a recent LEED structural analysis [12,14], but we comment later on whether adding this terminating layer best fits our XPD data. The bottom bilayer is almost the same as the bilayer of FeO(111) discussed in the prior section, but it differs in having 1/4 ML of Fe missing and a shorter vertical interlayer distance z_3 compared to bulk FeO(111). And the middle bilayer is quite different from those of FeO and α-Fe_2O_3(0001) in showing tetrahedral, octahedral, and tetrahedral sites of Fe as we go from the bulk towards to the surface. The third bilayer from the bottom is just a repeat of the bottom bilayer but with a horizontally-translated stacking sequence, with a more pronounced periodic rumpling of oxygen along the rows perpendicular to the plane of the figure, and with vertical spacings z_1 and z_2 that were varied in our analysis to yield best agreement with experiment.

The main features of the prior LEED structure for Fe_3O_4(111) on Pt(111) are [14]: one O surface atom in the unit cell (which is not bonded to the topmost Fe atoms) that is moved upward by ~0.4 Å with respect to the remaining three O atoms (which are in turn bonded to the topmost Fe atoms) and O-Fe-O interlayer spacings that are significantly different from bulk Fe_3O_4(111): z_1 = 0.83 Å (1.19 Å for bulk) and z_2 = 1.42 Å (1.19 Å

for bulk). Other relative Fe and O positions and lateral reconstructions present in this structure are discussed in detail in this LEED study [14]. Among the $Fe_3O_4(111)$ structural models tested are two sets of three different structures of $Fe_3O_4(111)$ with and without the topmost 1/4 ML of Fe. The major difference among the three structures in each set is different interlayer spacings in the O-Fe-O layers as indicated below. The three structures with topmost 1/4 ML Fe are: (1) the bulk vertical spacings (z_1 = 1.19 Å, z_2 = 1.19 Å), (2) the full surface reconstructed structure of LEED study (z_1 = 0.83 Å, z_2 = 1.42 Å), and (3) a structure modified for better fit to the XPD data (z_1 = 0.83 Å, z_2 = 1.07 Å), with all other surface reconstruction parameters as given in the LEED analysis. The remaining structures (4)-(6) tested for $Fe_3O_4(111)$ are the same as (1)-(3) above, respectively, but without the topmost 1/4 ML (i.e., they are O terminated). And these latter three structures do not include the surface O relaxation discussed earlier, since the presence of the topmost 1/4 Fe is thought to be the driving force for such relaxation.

The three different oxide structural models tested show threefold symmetric XPD patterns because the crystal structures themselves have threefold symmetry. Since our experimental XPD data for 3.0 ML show sixfold symmetry for Fe and nearly sixfold symmetry for O, we must assume the existence of two almost equally present domains with a 180° rotation between them, and in comparing with experiment, have thus summed equal populations of these two domains. In fact, these two domains can be thought of as growing from the base monolayer of FeO discussed in the Chapter 3 with either the favored or unfavored geometry for 1.0 ML.

In deciding which model best fits our data, all the experimental and theoretical XPD patterns are plotted and compared as normalized chi intensities rather than straight intensities, as discussed in Chapter 3. We have also used several criteria for deciding on the goodness of fit between theory and experiment: visual comparison of diffraction patterns, comparison of directions and anisotropy for various strong forward scattering

features, and R-factor calculations over the full hemisphere of experiment and theory. The results of the R-factor analysis are discussed in Appendix J.

We first summarize our experiment/theory comparisons for different structures of FeO(111) and Fe_2O_3(0001). All theoretical XPD patterns in Fig. 4.8 are obtained by calculating over only one third of the hemisphere and then threefold symmetry data folding and finally adding these folded data to the patterns with 180° rotated ones in order to simulate two equally populated domains. The first group, two and five bilayers of FeO(111) with different interlayer spacings and O stacking as described above, did not give good agreement for the structure, as shown in Figs. 4.8(a)-(c) for three of the cases tried. In particular, the theoretical simulations for two bilayers of FeO (Fig. 4.8(a) for FeO structure model (2) and Fig. 4.8(b) for structure model (3)), which might have been a reasonable description of oxide structures from 1.25 to 1.75 ML, do not explain the additional features in the experimental XPD patterns. Neither does a calculation for five bilayers (Fig. 4.8(c)) agree well with the 3.0 ML data. Thus, we conclude that the internal structure of the islands formed on top of the base layer is different from that of FeO. Poor agreement between experiment and theory was also found in simulations for Fe_2O_3(0001) XPD patterns, with typical theoretical results for two bilayers (AB O stacking) and three bilayers (ABA O stacking) of Fe_2O_3(0001) being shown in Figs. 4.8(d) and (e).

For the case of Fe_3O_4, the overall fit between the experiment and theory is much improved compared to the other two case of FeO and Fe_2O_3, suggesting that the internal structure of the islands for 3.0 ML is close to Fe_3O_4. Among them, Fig. 4.9 shows two-domain averaged O XPD data for four structural models tested: the full surface relaxed structure from LEED including a topmost 1/4 ML of Fe in Fig. 4.9(a), the same structure without the 1/4 ML of Fe in Fig. 4.9(b), our improved structural model yielding a better fit to the XPD experimental data and including the 1/4 ML of Fe in Fig. 4.9(c), and the

same improved model without the 1/4 ML of Fe in Fig. 4.9(d) (which yields the overall best fit to experiment). (We should note however, that the LEED study used a different iron oxide growth mode by repeating 1 ML Fe deposition and oxidation eight times to yield a thicker 8 ML film.) The predictions for Fe XPD for these models are not shown here, since they do not show noticeable differences between them. For O XPD, the major difference between the LEED structures shown in Figs. 4.9(a) and 4.9(b) and the structures derived in this study shown in Figs. 4.9(c) and 4.9(d) is the polar angle positions of the six strongest forward scattering peaks: these peaks, which are found at a polar angle of 34° in the experimental O XPD patterns, are shifted by a large amount of about 6° to a polar angle of 40° with the LEED structural parameters. An R-factor analysis including data over the full hemisphere further supports these structural conclusions [see Appendix J]: the R-factors are less for O-terminated structures without the topmost 1/4 ML of Fe, and they are also less for our structural models as compared to the LEED structures. The minimum R-factor over all of the cases we have tried is for our improvment of the LEED structure and without the topmost 1/4 ML of Fe (Fig. 4.9(d)). The lack of an extra 1/4 ML of Fe at the surface is also supported by an analysis of the polar-angle dependence of the O 1s:Fe $2p_{3/2}$ peak intensity ratio, as averaged over the full-hemisphere XPD data for both 1.0 ML and 3.0 ML oxide films. These θ-dependent O:Fe peak intensity ratios are very similar for both a 1.0 ML film (which we know has an O- terminated structure, as discussed previously) and a 3.0 ML film, and do not show for the 3.0 ML case any noticeable decrease in the O:Fe intensity ratio at low takeoff angles that would be expected in this more surface sensitive region of emission. Further details of this analysis are given in Appendix D.

In deciding which structural model best fits our experimental data for a 3.0 ML film of iron oxide on Pt(111), we have also carried out two azimuthal scan MSC calculations (one for Fe emission at a polar angle of 38° and one for O emission at a polar angle of 34

°) where strong forward scattering and other peaks are present for each case. As discussed in detail in Appendix H, the MSC results actually give a somewhat worse fit to the experimental data as far as predicting relative peak intensities for both cases. It is not clear why MSC does not provide a better description of our data than the less accurate SSC, but it could be due to the presence of some disorder in these thicker iron oxide films (as suggested by the fuzzy LEED spots) and/or the multilayered structure of the oxide film (as seen in the STM image), that tends to reduce or distort any chains of forward scattering atoms and thus also multiple scattering.

Figs. 4.10 and 4.11 now directly compare our experimental data for 3.0 ML of oxide and both Fe and O emission with the final best fit theoretical results for the structure described earlier (general cluster as shown in Fig. 4.7, but without topmost 1/4 ML Fe). In Figs. 4.10 and 4.11, the measured XPD patterns obtained for 3.0 ML coverage are shown in (a), the theoretical calculations for one of the two threefold domains are shown in (b), the final theoretical calculations adding two possible equally-populated domains with 180° rotation between them are shown in (c), and the simple forward scattering directions for the cluster used to calculate the single-domain XPD pattern of (b) are shown in (d). In Figs. 4.10(d) and 4.11(d), each circle represents a possible forward scattering direction in the cluster, with the diameter of each circle being proportional to 1/(distance from a given emitter). The threefold symmetry of the crystal structures implicit in these clusters is evident in Figs. 4.10(b), 4.10(d), 4.11(b), and 4.11(d), and even before summing over two domains, we see that these calculations well reproduce all of the main peaks (actually half of the peaks) as to positions and relative intensities. The positions of these strongest peaks also agree with directions along which several strong forward scattering events are expected, as illustrated in Figs. 4.10(d) and 4.11(d). For example, the peaks at the polar angles around 36° (34°) and 62° (56°) are well reproduced for Fe (O) emission. This agreement is better illustrated in Figs. 4.10(c) and

4.11(c) with sixfold symmetry, where theory reproduces all of the strong peaks seen in the experimental data, as well as most of the fine structure for both Fe and O emission, including the dark bands in between various peaks. The experimental patterns do not exhibit as much fine structure, and are somewhat smeared out compared to theory, but the STM image in Fig. 4.4(d) makes it clear that the actual surface consists of many different kinds of emitters in the several layers of islands formed, and it is thus not at all surprising for experiment to show less dramatic XPD structure. What is remarkable is that the agreement between experiment and theory is as good as it is, suggesting that the average oxide surface is well described by our structural model. An at-first-sight negative aspect of the fit between experiment and theory in the Fe data can be seen in certain features at polar angles less than about 16°, for which the 2-domain calculation shows six double bands of intensity and 6 sharp peaks that are not obvious in the experimental data. However, the double bands are in fact suggested in the actual azimuthal scans for these polar angles, but with smaller relative intensities and thus anisotropies than in theory, making them difficult to see in Fig. 4.10 [see Appendix F]. Anisotropies at such low takeoff angles are also expected to be reduced in the experiment due to the multilayered structure of the thick iron oxide films, which will result in effectively smaller grain sizes for these grazing takeoff angles. The six sharp peaks at the edge of the theoretical diffraction pattern we would not expect to see clearly in the experiment for the same reason, and they could also be obscured by surface refraction effects not properly included in the theory. With regard to threefold versus sixfold symmetry, we also note that full 360° azimuthal scans of O and Fe intensities show that O is overall in a threefold symmetric environment (albeit weakly): the anisotropies of the two sets of six peaks in O 1s emission at polar angles of 34 - 38° and 54 - 58° indicate that one set of three in each case has higher peak-minus-background intensities than the other three by about 3 %. By contrast, the data for Fe emission are

sixfold symmetric within our experimental error of about 1%. This small deviation from sixfold symmetry we explain as being due to having two domains of oxide structures that are not equally populated, with the O forward scattering peaks being somehow more sensitive to this non-equality than those of Fe.

Our final structural model for the predominant species present in a 3.0 ML iron oxide film grown on Pt(111) is thus $Fe_3O_4(111)$, as shown in Fig. 4.7, but without a topmost 1/4 ML of Fe. In the latter respect, our model is thus different from the structure proposed in the prior LEED study of this system [12,14]. Also, in order to adequately describe the angular positions of certain forward scattering peaks and fully minimize R-factors, the Fe-O interlayer spacing is found to be 1.07 Å, while the O-Fe interlayer spacing of z_1 = 0.83 Å is the same as found in the LEED study; our z_2 value thus corresponds to an inward relaxation compared to the bulk by 0.12 Å (~ 10 %), whereas the LEED study found an outward relaxation by 0.23 Å (~ 20 %). The relaxation that we find is also qualitatively similar to the case of 1 ML FeO/Pt , where an inward relaxation of 0.6 Å (~ 48 %) was found. Although our differences with the LEED structure as to surface termination and Fe-O interlayer separation could be due to the different one-step preparation procedure used for the oxide in our study, it seems reasonable that the local structure near the surface of the oxide film should not be that sensitive to the method of preparation. The oxide layers formed in this LEED study did seem to have better long-range order however, leading to sharper diffraction spots than seen in Fig. 4.3. It would thus certainly be of interest to carry out XPD measurements on films prepared by this other procedure.

Finally, we discuss the structure of the base layer underlying the oxide islands for higher coverages. Although the base layer of 1 ML of FeO(111) with its superlattice is clearly present in between the oxide islands for coverages between 1.25 and 1.75 ML, and is seen in all of LEED, STM, and XPD, we cannot unambiguously tell whether the

oxide islands form over this base layer without disturbing it, or simply incorporate it into the oxide structure and in the process destroy the superlattice. Our results are most consistent with the latter conclusion, since the strong diffraction features at polar angles higher than 20° in both Fe and O emission from a 3.0 ML coverage are also found in the XPD data for 1.75 ML, as well as to a large degree also for 1.50 ML. Another way to see this is to subtract out the strongest peaks at a polar angle of 20° in Fe emission for 1.75 ML, which are not seen for the case of 3.0 ML and are well explained as being due to the persistence of the base layer without islands on top, as seen also by LEED and STM. In fact, if we do not consider these strong peaks at polar angles around 20° for the 1.75 ML oxide, both Fe and O XPD data are almost identical to the corresponding results for 3.0 ML, leading to the final conclusion that the internal atomic structure of the islands is $Fe_3O_4(111)$ with the reconstructions indicated earlier.

4.4. CONCLUSIONS

Three complementary surface structure probes, LEED, STM, and XPD, have been applied to the growth of iron oxides on Pt(111) for iron coverages from 1.25 ML to 3.0 ML. We have shown that the growth mode of these oxides is essentially Stranski-Krastanov: iron oxide islands form on top of a 1 ML FeO(111) superlattice whose presence is clearly seen by all three techniques. For iron oxide films of 3.0 ML thickness, the XPS-derived Fe $2p_{3/2}$ binding energy and stoichiometry are found to indicate the presence of Fe_3O_4, and a detailed analysis of the XPD results proves it to be $Fe_3O_4(111)$-magnetite in two almost equally populated domains with a 180° rotation between them. The structural parameters for this differ from those of a previous LEED study [12,14] in the first Fe-O interplanar spacing as well as in not requiring a topmost 1/4 ML of Fe to terminate the surface. Our XPD data for the lower coverages, taken

together with the results for ≤ 1 ML in Chapter 3, also suggest that oxide islands consisting largely of Fe_3O_4 are present over the full coverage range from 1.25 to 3.0 ML. Our combined LEED, STM, and XPD results for this system thus make it clear that each of these three techniques is sensitive to different aspects of surface structure, and that using any one of them by itself can lead to erroneous or partial conclusions. For example, using LEED alone to determine coverages via that for which the FeO superlattice is most ideal could lead to an error of 25-50%, since the pattern is sharpest for 1.25-1.50 ML. On the other hand, most of the details of the structure of $Fe_3O_4(111)$ in thicker films has been correctly determined by a prior LEED analysis on this system. With STM, it was possible in prior work to propose a fundamentally correct model for the FeO superlattice, but not to determine its termination, interlayer spacing, or oxygen domain orientations. STM is also of course unique in directly sensing changes in surface topography, short-range order, and long-range order. XPS and XPD as atom-specific probes of composition, chemical state, and short-range-order structure thus complement these two techniques beautifully, as we believe is illustrated in this study. Future epitaxial growth studies should thus benefit by the *in situ* combination of these three techniques.

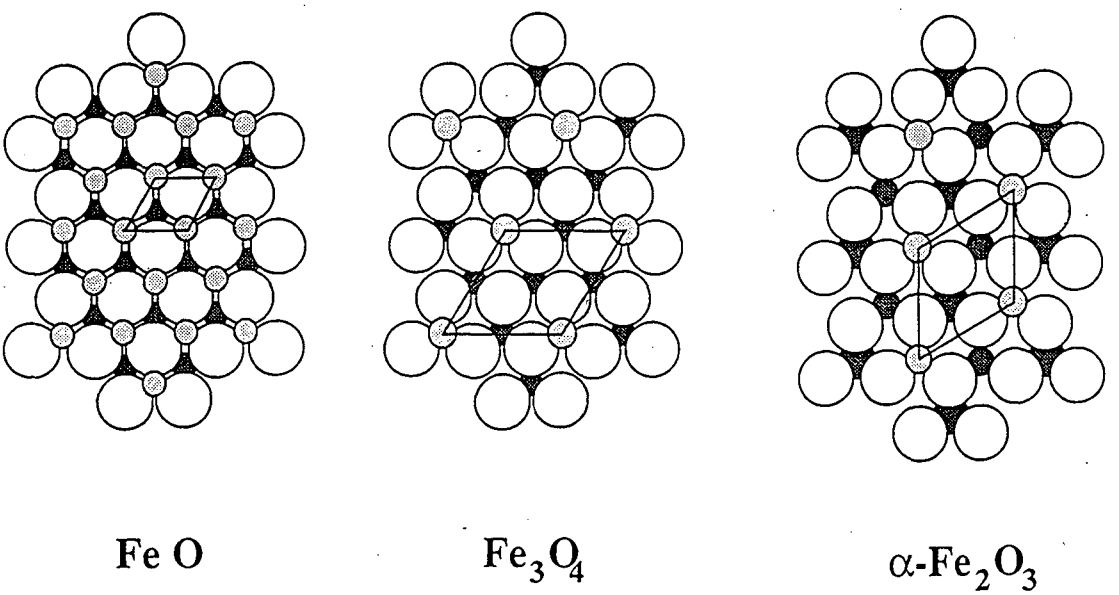

Figure 4.1. View of three different iron oxides, with (111) termination for FeO and Fe_3O_4, and (1000) termination for α-Fe_2O_3. One oxygen layer (oxygen anions are indicated by large open circles) and iron layers on both sides of it (shown with light or dark shading) are shown in each case. The lateral periodicities are indicated by the different two-dimensional unit cells. The darker circles repressent Fe atoms above and below the O layer while the larger darker circles represent the Fe atoms only below the O layer.

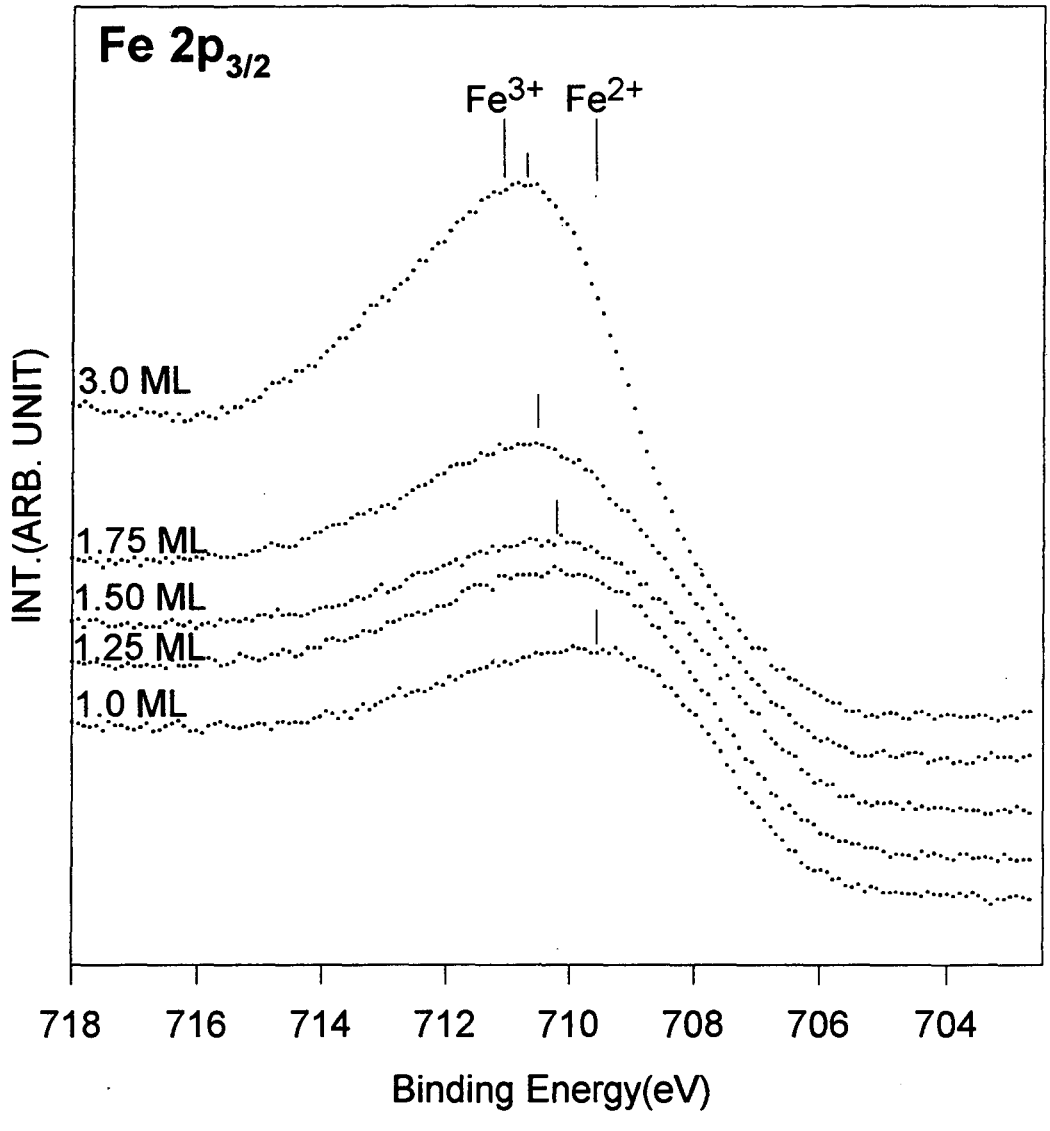

Figure 4.2. Fe $2p_{3/2}$ XPS spectra obtained for iron oxide coverages from 1.0 ML to 3.0 ML. Al Kα (1486.7 eV) was used for excitation. The binding energy moves toward higher binding energy as the coverage increases.

Figure 4.3. LEED patterns at a 53.5 eV incident energy for different iron oxide coverages from 1.25 ML to 3.0 ML. The LEED pattern of the 1 ML FeO superlattice structure (cf. Fig. 3.2) persists with only small changes until 1.75 ML and has disappeared by 3.0 ML.

1.25 ML

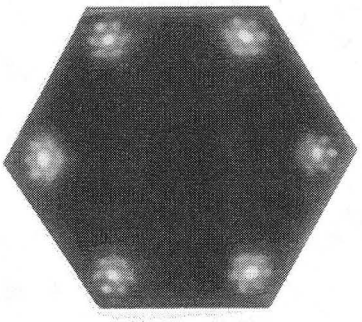

1.50 ML

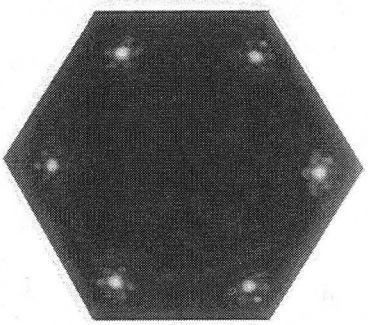

1.75 ML

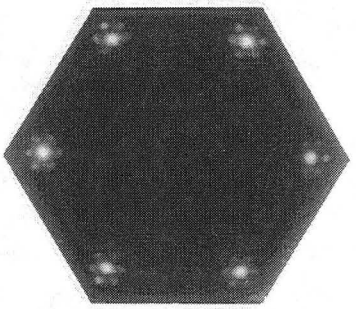

3.00 ML

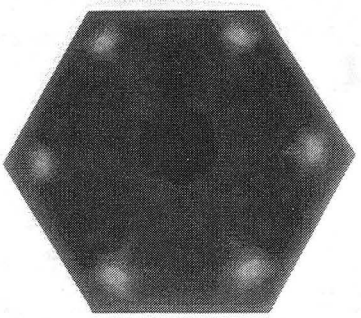

Figure 4.4(a) and 4.4(b). STM images taken in constant-current mode for the same surfaces and iron oxide coverages considered in Fig. 4.3: (a) 1.25 ML-- This 264 nm x 264 nm image shows preferential growth of small islands (~5 nm diameter) near a step edge. The current was 2.9 nA and the sample bias voltage was 460 mV. (b) 1.50 ML-- This 400 nm x 400 nm image shows a mix of small and large islands (up to ~25 nm diameter) growing on top of a flat base layer. The current was 2.2 nA and the sample bias voltage was 460 mV.

(a) 1.25 ML

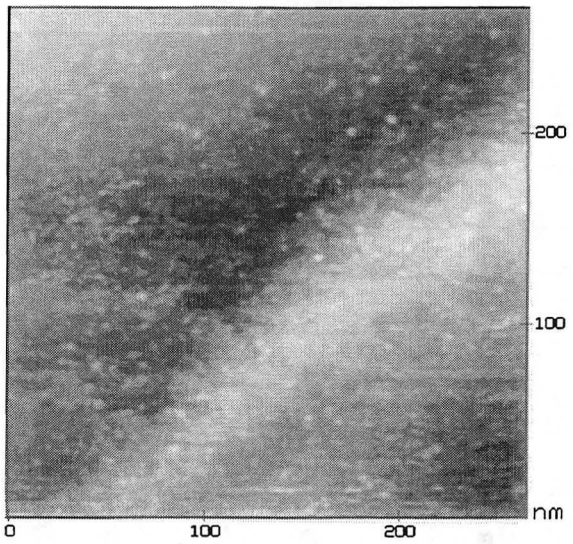

(b) 1.50 ML

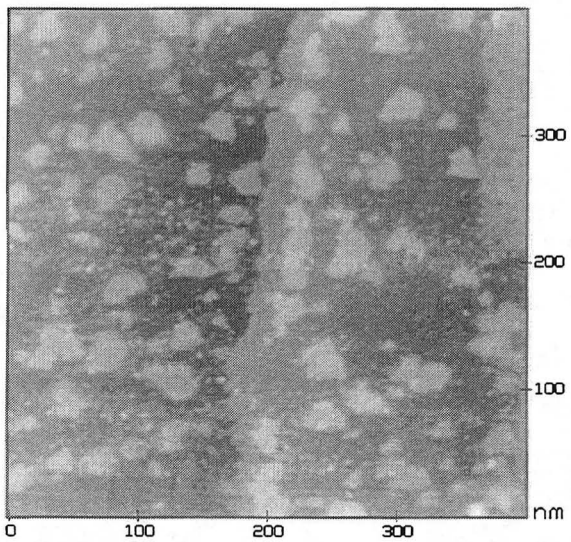

Figure 4.4(c) and 4.4(d). STM images taken in constant-current mode for the same surfaces and iron oxide coverages considered in Fig. 4.3: (c) 1.75 ML-- This 800 x 800 nm image shows a higher coverage by islands compared to 1.50 ML, and shapes indicating extensive coalescence. The current was 3.0 nA and the sample bias voltage was 460 mV. (d) 3.0 ML-- This 460 x 460 nm image shows mulitlayer growth terminating in smaller islands with smaller topmost island sizes as compared to the lower coverages. The flat base layer is not visible at this coverage. The current was 3.0 nA and the sample bias voltage was 460 mV.

(c) 1.75 ML

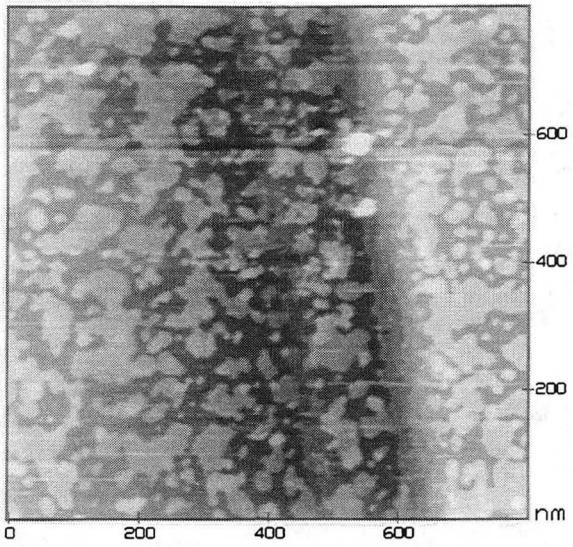

(d) 3.00 ML

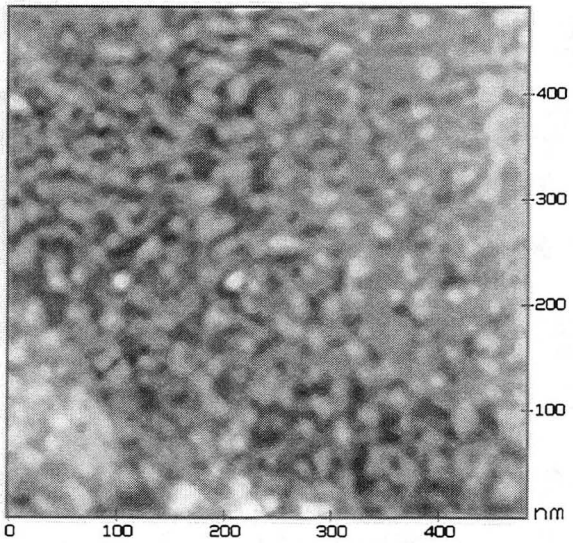

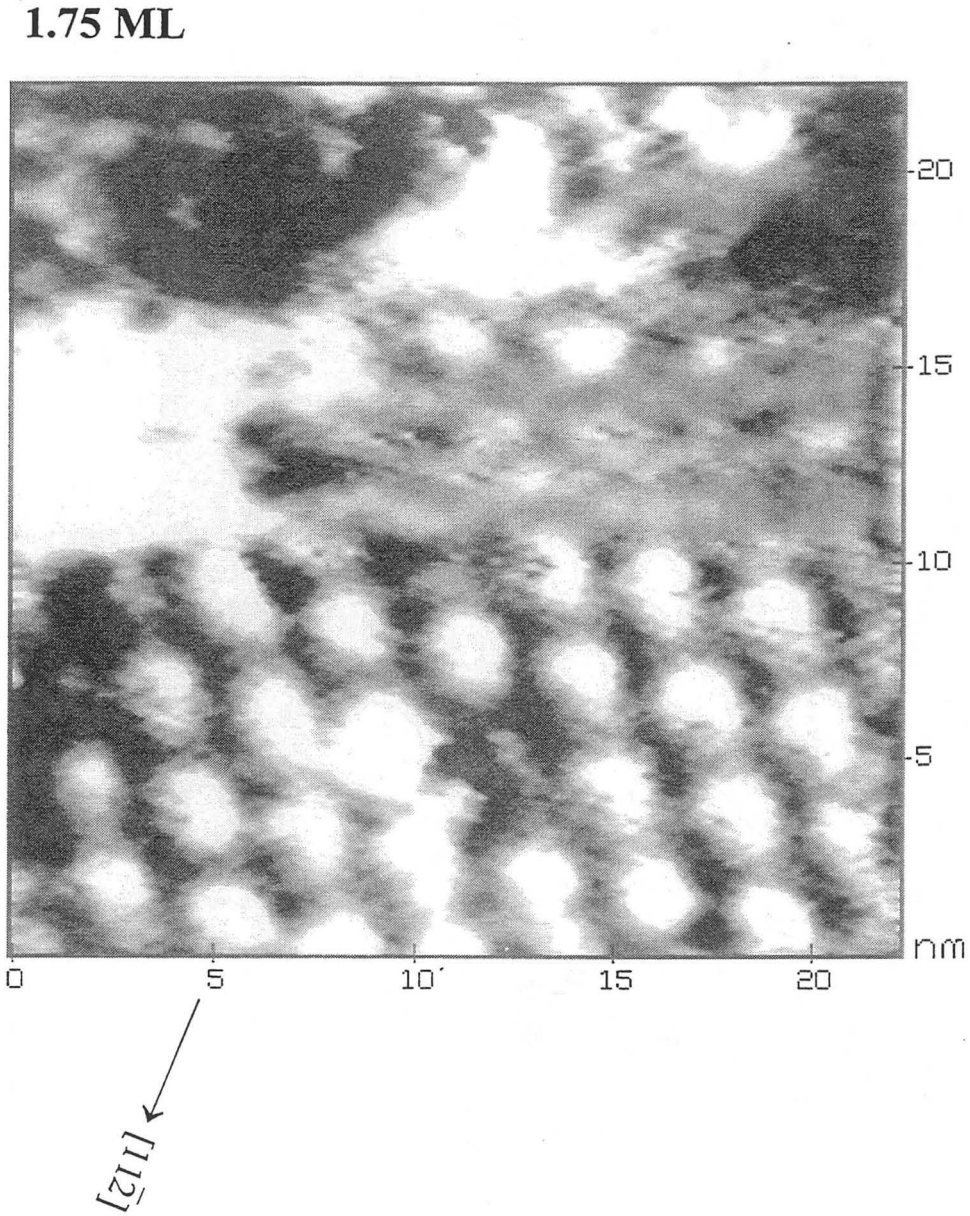

Figure 4.5. A constant-height STM image of a 1.75 ML iron oxide layer on Pt(111). Oxide islands (top half of image) form on top of a superlattice of 1 ML FeO/Pt(111) with 26 Å periodicity (lower half of image). The image is 22 x 22 nm, the average current was 2.22 nA and the sample bias voltage was 460 mV.

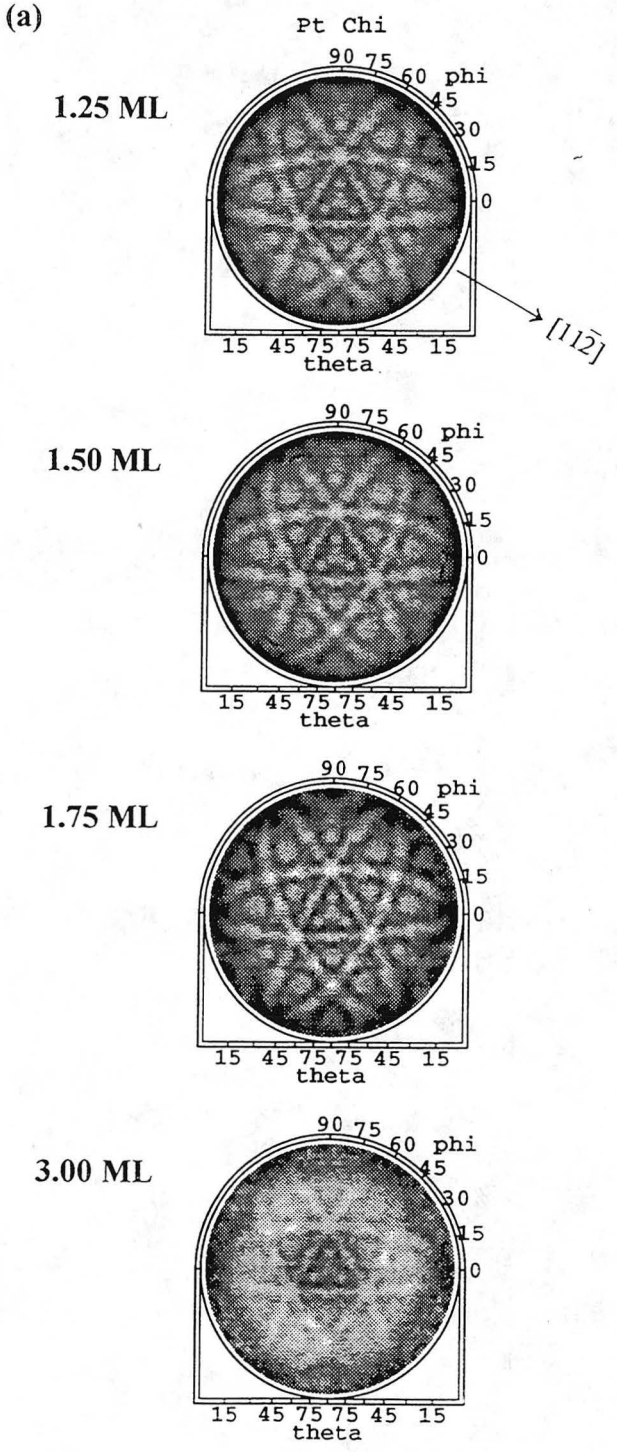

Figure 4.6(a). Pt 4f full-solid-angle XPD patterns in stereographic projection for the same surfaces and iron oxide coverages as Figs. 4.3 and 4.4. Al Kα (1486.7 eV) was used for excitation. Intensities here are normalized chi functions.

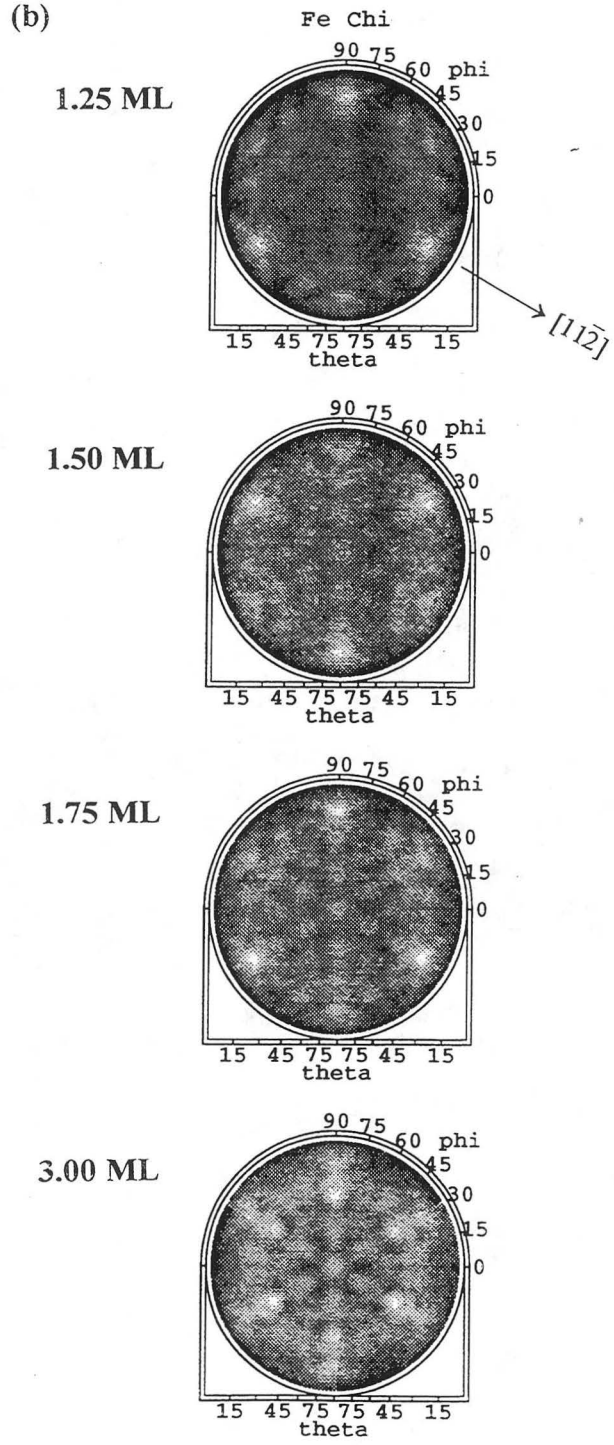

Figure 4.6(b). Fe $2p_{3/2}$ full-solid-angle XPD patterns in stereographic projection for the same surfaces and iron oxide coverages as Figs. 4.3 and 4.4. Al Kα (1486.7 eV) was used for excitation. Intensities here are normalized chi functions.

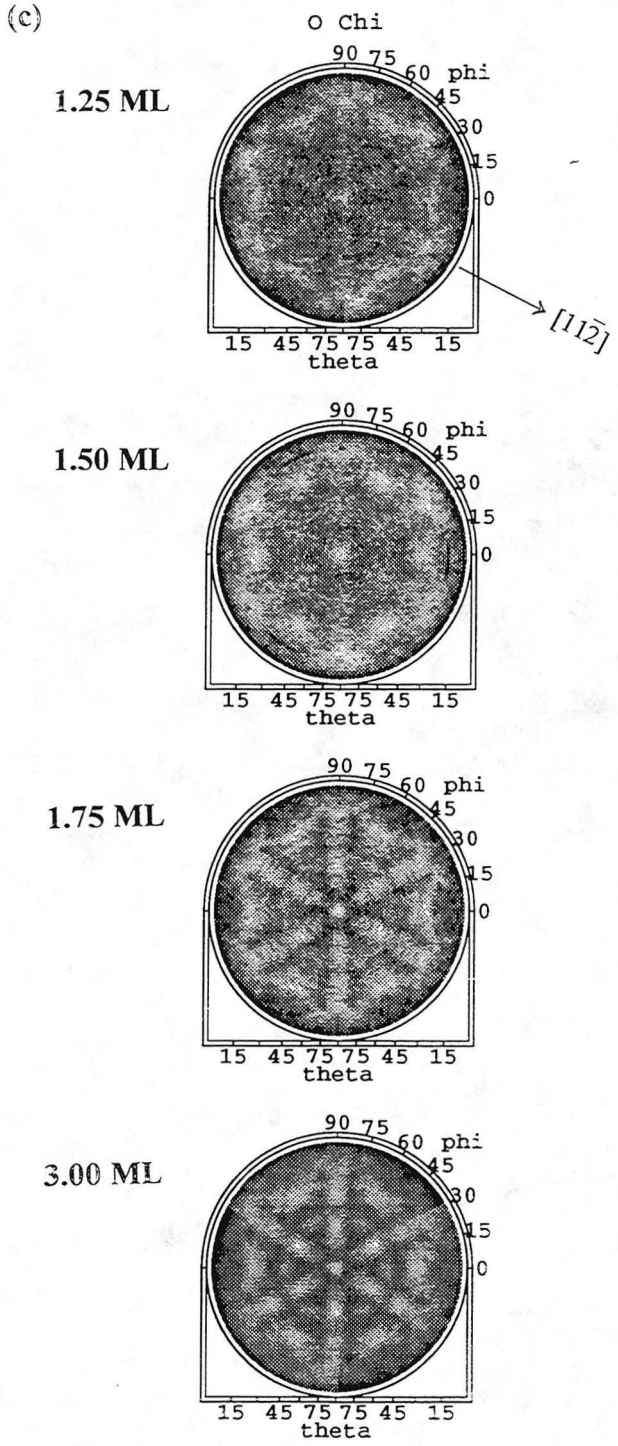

Figure 4.6(c). O 1s full-solid-angle XPD patterns in stereographic projection for the same surfaces and iron oxide coverages as Figs. 4.3 and 4.4. Al Kα (1486.7 eV) was used for excitation. Intensities here are normalized chi functions.

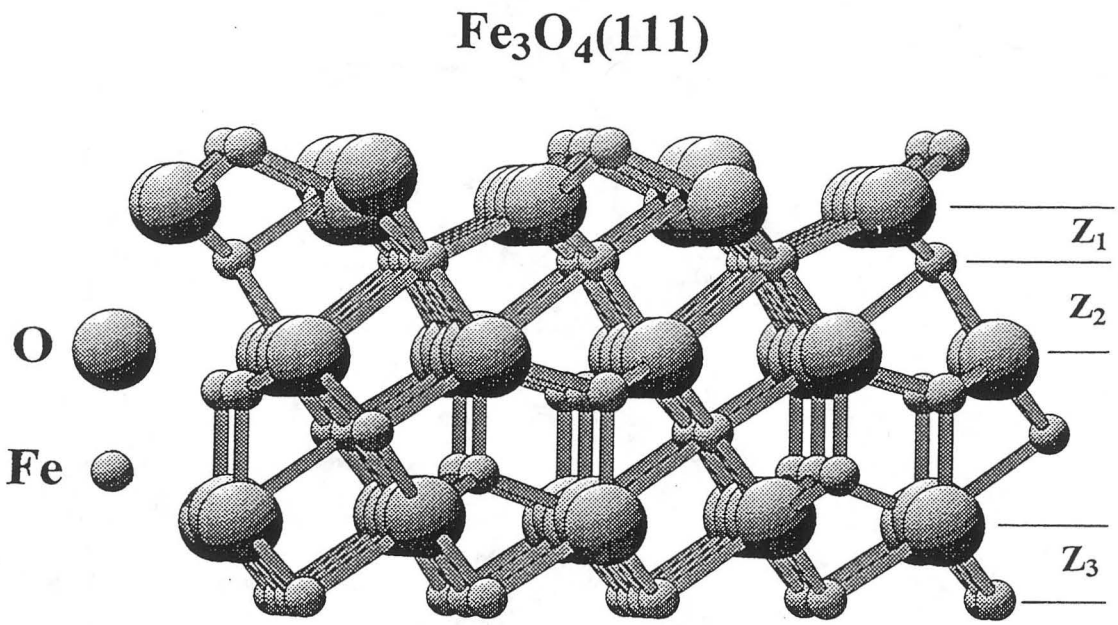

Figure 4.7. The atomic cluster used to model XPD from a 3.0 ML coverage of $Fe_3O_4(111)$. The surface is shown here terminated with 1/4 ML of Fe, but calculations have been performed with and without this termination. Note the vertical relaxation of one O atom compared to the remaining three O atoms within the unit cell, as well as possible relaxations in the O-Fe-O interlayer spacings ($z_1$and z_2).

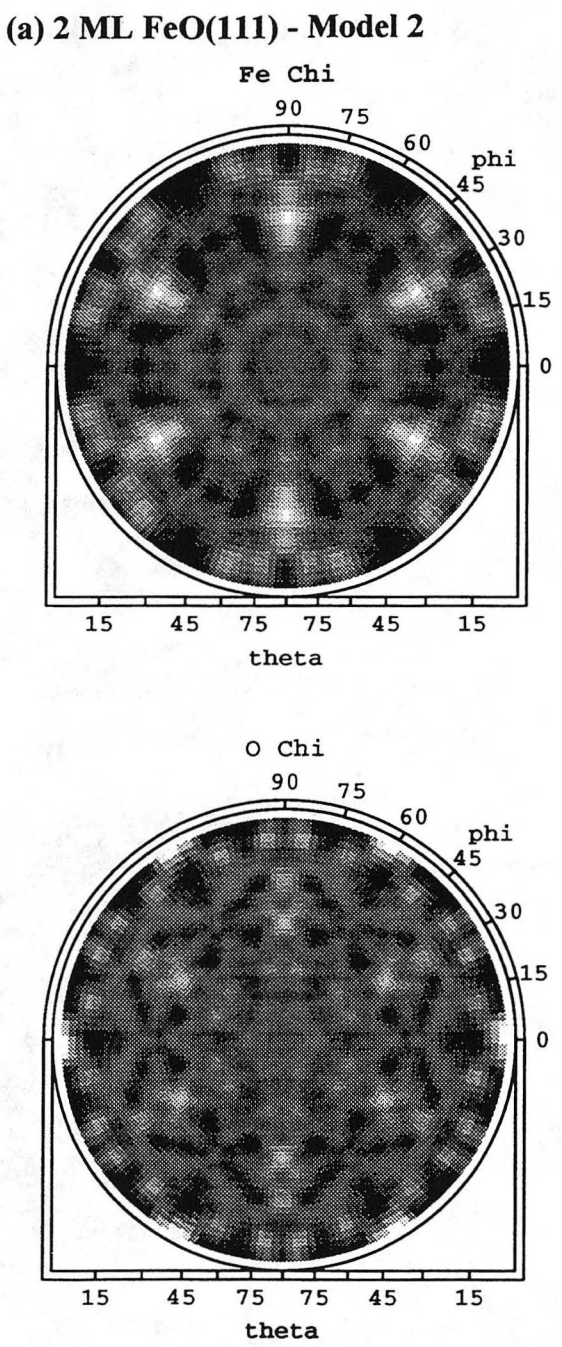

Figure 4.8(a). Theoretically calculated XPD chi modulations of Fe $2p_{3/2}$ (top) and O 1s (bottom) for FeO and Fe_2O_3, again in stereographic projection. (a) two bilayers of Fe and O in the FeO(111) configuration, with the bottom bilayer relaxed inward as for 1 ML FeO/Pt (structure model 2).

(b) 2 ML FeO(111) - Model 3

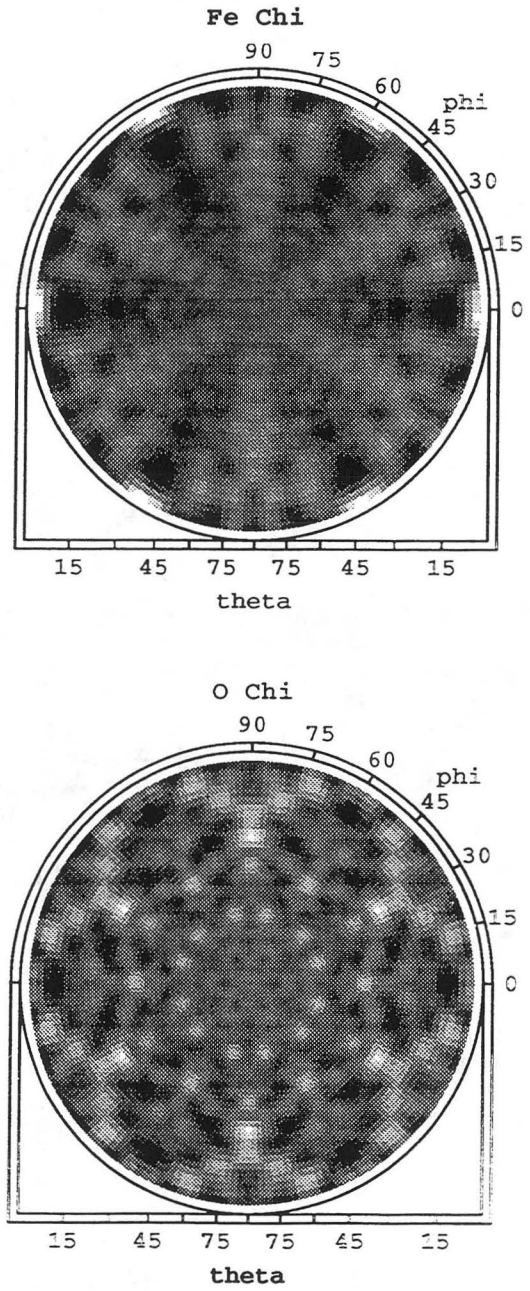

Figure 4.8(c). Theoretically calculated XPD chi modulations of Fe $2p_{3/2}$ (top) and O 1s (bottom) for FeO and Fe_2O_3, again in stereographic projection. (c) five bilayers of FeO(111) (structure model 4).

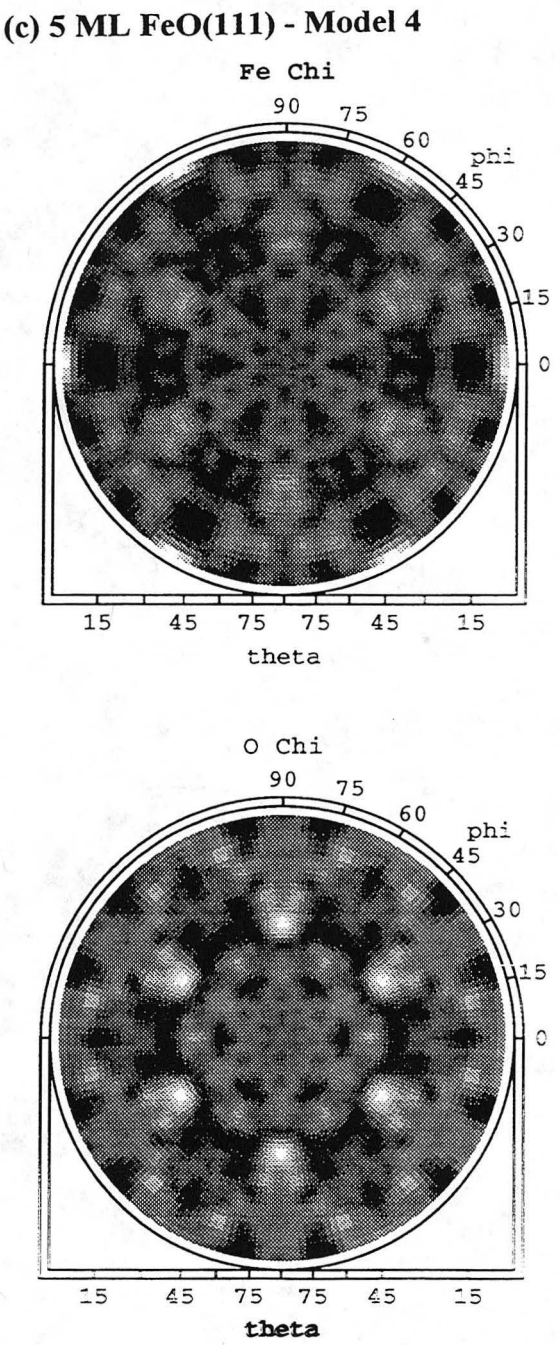

Figure 4.8(c). Theoretically calculated XPD chi modulations of Fe $2p_{3/2}$ (top) and O 1s (bottom) for FeO and Fe_2O_3, again in stereographic projection. (c) five bilayers of FeO(111) (structure model 4).

(d) 2 ML Fe_2O_3

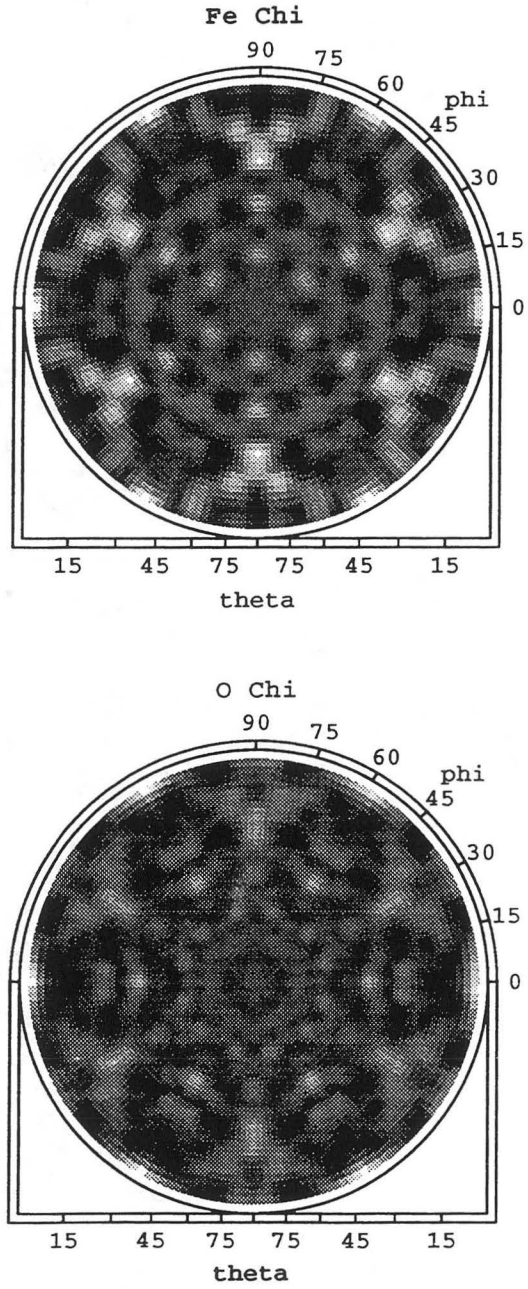

Figure 4.8(d). Theoretically calculated XPD chi modulations of Fe $2p_{3/2}$ (top) and O 1s (bottom) for FeO and Fe_2O_3, again in stereographic projection. (d) 2 bilayers of $Fe_2O_3(0001)$.

(e) 3 ML Fe_2O_3

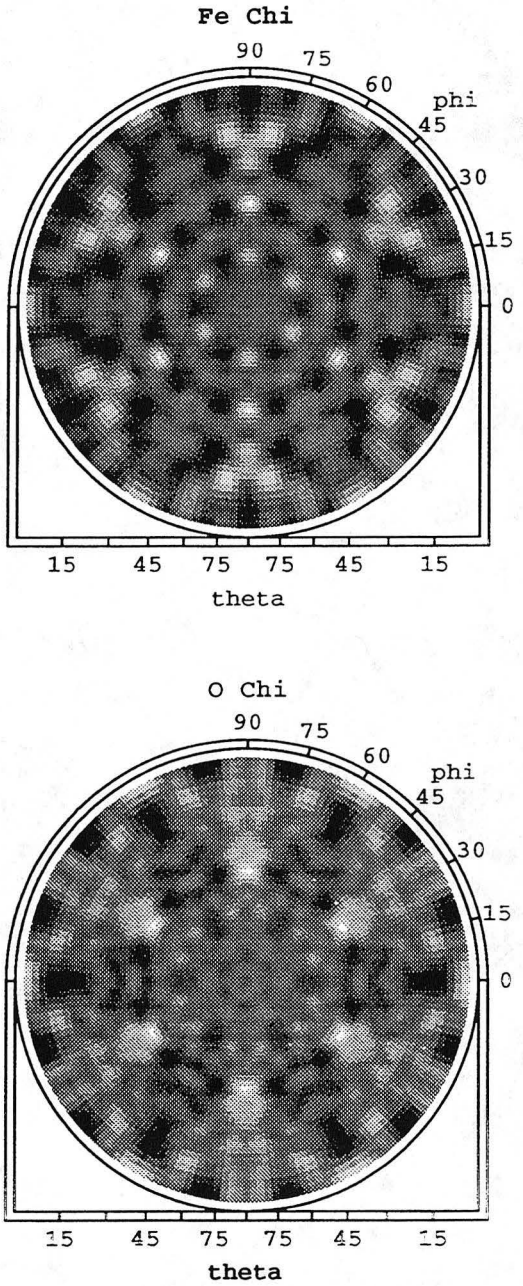

Figure 4.8(e). Theoretically calculated XPD chi modulations of Fe $2p_{3/2}$ (top) and O 1s (bottom) for FeO and Fe_2O_3, again in stereographic projection. (e) 3 bilayers of Fe_2O_3 (0001).

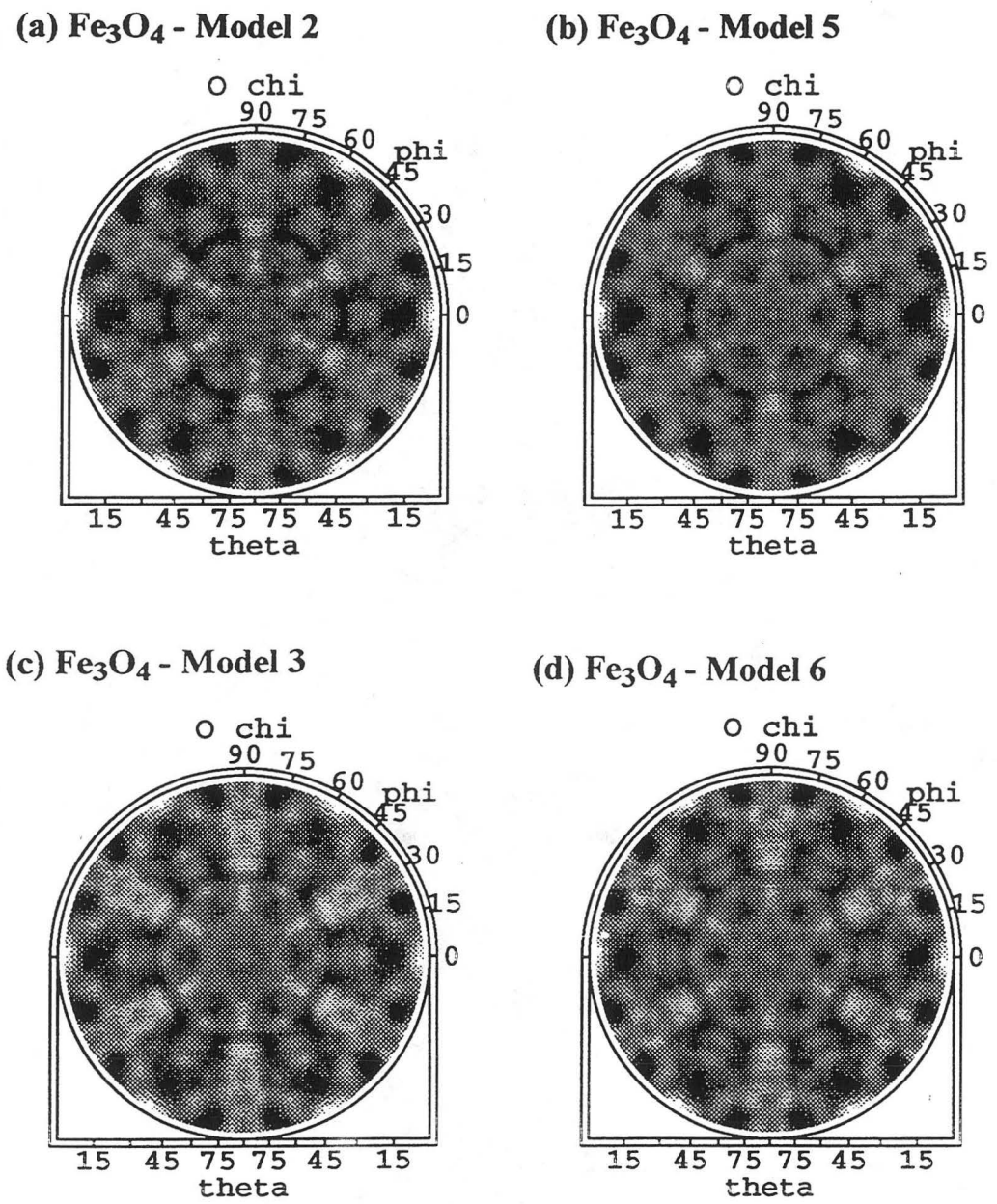

Figure 4.9. Theoretically calculated XPD chi modulations of O 1s for four different structural models of $Fe_3O_4(111)$ tested, again in stereographic projection. Calculations for the fully relaxed structure determined in a recent LEED study (z_1 = 0.83 Å, z_2 = 1.42 Å) is shown in (a) with a topmost 1/4 ML of Fe terminating the surface and in (b) without this terminating Fe. Calculations for our optimized structural model (z_1 = 0.83 Å, z_2 = 1.07 Å) are shown in (c) with the topmost 1.4 ML of Fe, and in (d) without it.

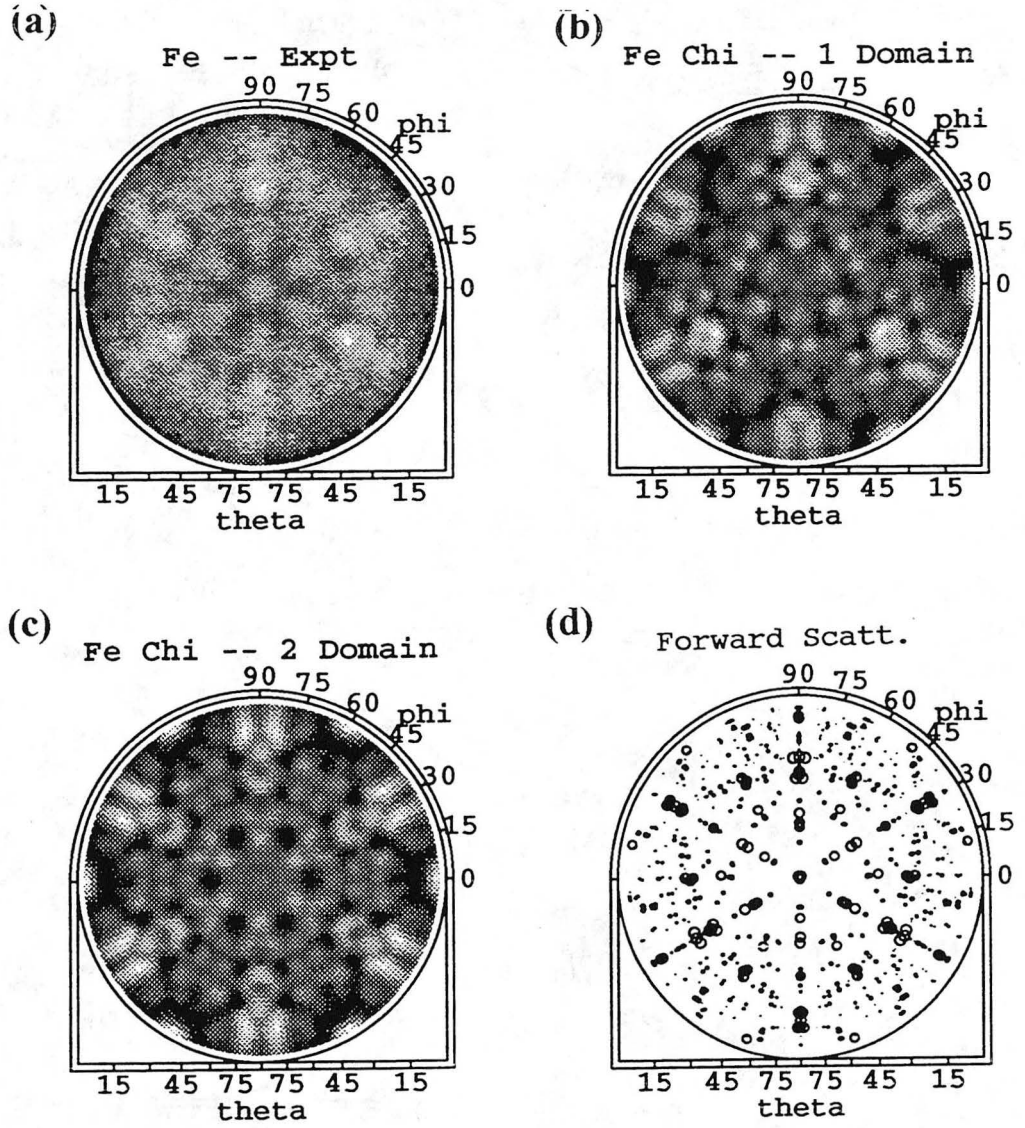

Figure 4.10. Full-solid-angle XPD patterns for Fe $2p_{3/2}$ emission from 3.0 ML iron oxide on Pt(111), again in stereographic projection, are compared to theoretical simulations for our optimized model for $Fe_3O_4(111)$: (a) experimental data, (b) single-domain calculation, (c) two-domain calculation involving the sum of (b) and a similar pattern rotated by 180°, (d) illustration of the various forward scattering events possible in the cluster utilized, with circle size being inversely proportional to distance from a given emitter. The cluster used was based on the geometry of Fig. 4.7, but without the topmost 1/4 ML of Fe, and with $z_1 = 0.83$ Å and $z_2 = 1.07$ Å.

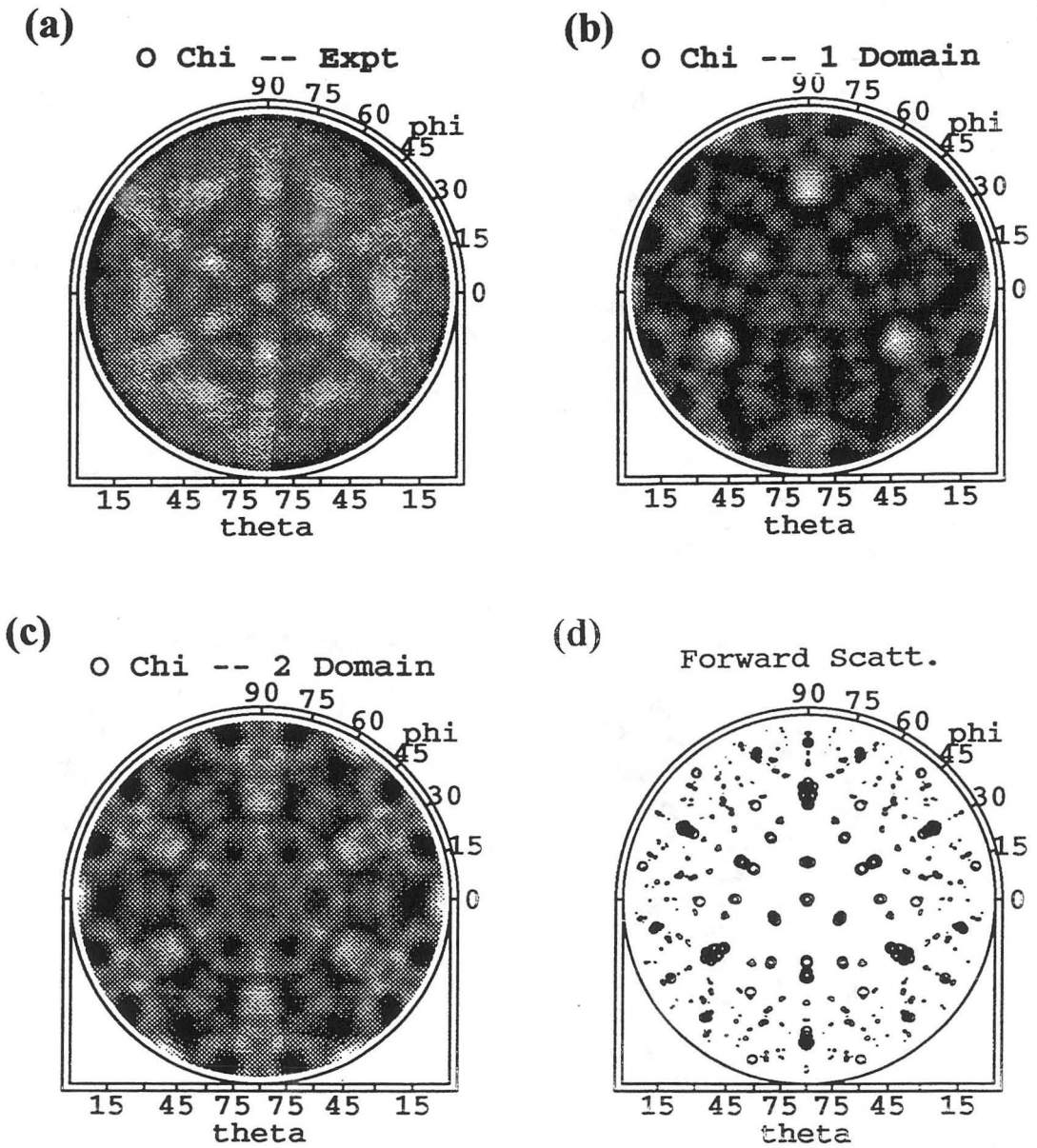

Figure 4.11. As Fig. 4.10, but for O 1s emission.

REFERENCES

[1] A. Zangwill, Physics at Surfaces, Cambridge University Press, Cambridge, 1988

[2] T.B. Massalski, J.L. Murray, L.H. Bennet, and H. Baker, Binary Alloy Phase Diagrams, American Society for Metals, Metals Park, OH 1986 p. 1807

[3] R.G. Wyckoff, Crystal Structures, Interscience, New York 1963

[4] V.E. Henrich and P.A. Cox, The Surface Science of Metal Oxides, Cambridge University Press, Cambridge, 1994

[5] D. Alder, in Solid State Physics, edited by H. Ehrenreich, F. Seitz, and D. Turnbull, Vol. 21, Academic, New York, 1968

[6] C.R. Brundle, T.J. Chuang, and K. Wandelt, Surf. Sci. 68, 459 (1977)

[7] M. Muhler, R. Schlogl, and G. Ertl, J. Catal. 126, 339 (1990)

[8] M. Muhler, R. Schlogl, and G. Ertl, J. Catal. 138, 413 (1992)

[9] R.J. Lad and V.E. Henrich, Surf. Sci. 193, 81 (1988)

[10] R.L. Kurtz and V.E. Henrich, Surf. Sci. 129, 345 (1983)

[11] N.G. Condon, P.W. Murray, F.M. Leibsle, G. Thornton, A.R. Lennie, and D.J. Vaughan, Surf. Sci. 310, L609 (1994)

[12] A. Barbieri, W. Weiss, M.A. Van Hove, and G.A. Sormojai, Surf. Sci. 302, 259 (1994)

[13] G. Tarrach, D. Bürgler, T. Schaub, R. Wiesendanger, and H.-J. Güntherodt, Surf. Sci. 285, 1 (1993)

[14] W. Weiss, A. Barbieri, M.A. Van Hove, and G.A. Sormojai, Phys. Rev. Lett. 71, 1884 (1993)

[15] H.C. Galloway, J.J. Benitez, and M. Salmeron, J. Vac. Sci. Technol. A 12, 2302 (1994)

[16] C.R. Brundle, T.J. Chuang, and K. Wandelt, Surf. Sci. 68, 459 (1977)

[17] T.J. Chuang, C.R. Brundle, and D.W. Rice, Surf. Sci. 59, 413 (1976)

[18] G.C. Allen, M.T. Curtis, A.J. Hooper, and P.M. Tucker, J. Chem. Soc. Dalton Trans. 1525 (1974)

[19] C.R. Brundle and A.F. Carley, Chem. Phys. Lett. 31, 423 (1975)

[20] D.P. Woodruff and T.A. Delchar, Modern Techniques of Surface Science, Cambridge University Press, Cambridge (1986)

[21] D.J. Friedman and C.S. Fadley, J. Electron Spectrosc. and Relat. Phenom. 51, 689 (1990)

[22] A.P. Kaduwela, D.J. Friedman, and C.S. Fadley, J. Electron Spectrosc. and Relat. Phenom. 57, 223 (1991)

[23] C.S. Fadley in Synchrotron Radiation Research: Advances in Surface Science, R.Z. Bachrach, Ed. (Plenum, New York) (1992)

[24] M. Sagurton, E.L. Bullock, C.S. Fadley, Surf. Sci. 182, 287 (1987)

CHAPTER 5

CONCLUDING REMARKS

"The surface was invented by the devil," said the physicist Wolfgang Pauli. Pauli's frustration was based on the simple fact that the surface of a solid serves as the boundary between the solid and the outer world. Surface structures are thus more complex and differ from those of the interior because an atom at a surface has a different surrounding environment. A number of surface structure probes have thus been developed in recent years in an attempt to determine the structures at a surface, as well as other properties of a surface (e.g., magnetic susceptibility). While it is true that no single technique can yet provide a definitive description of the complexities of the surface, a combination of several techniques along with their respective experimental data and theoretical analyses may permit a consensus to be reached on models to describe them. In this dissertation, a particularly powerful set of three complementary surface structure probes - XPD, STM, and LEED - have, for the first time, been combined in the same experimental system and applied to the example case of epitaxial oxide growth on a metal substrate. Some of our essential conclusions and their relationship to prior work are as follows.

For the first monolayer of iron oxide formed on Pt(111), XPD shows a topmost oxygen layer relaxed significantly inward by 0.6 Å compared to bulk FeO(111), while STM and LEED show an incommensurate oxide film with short-range and long-range periodicities of 3.1 Å and 26 Å, in agreement with prior work. Our combined XPD, STM, and LEED results also unambiguously show that the stacking of O atoms in the FeO(111) bilayer is dominated by one of two possibilities, with oxygen atoms sitting along Pt $<11\bar{2}>$ directions as viewed from their nearest-neighbor Fe atoms. This possibility of two oxygen orientations lead to a second type of oxide domain that is in fact consistent with our data for thicker oxide layers.

For thicker layers of iron oxide on Pt(111), STM shows the growth mode of the iron oxide to be Stranski-Krastanov in nature: a first base monolayer with good two-dimensional order on which three-dimensional oxide islands grow, while LEED continues to indicate the structure of the base monolayer, showing almost identical patterns over the coverage range from 1.00 to 1.75 ML. In addition, XPS quantitative analyses, Fe core binding energies, and XPD combine to show that the islands formed on top of the base layer are composed of Fe_3O_4 (magnetite) in (111) orientation. This Fe_3O_4 is present in two domains rotated by 180°with respect to one another. We also conclude that the surface is terminated by an O layer instead of the 1/4 ML of Fe proposed previously, and that the near-surface Fe-O interlayer spacings are different from a previously-proposed model.

Overall, the work presented here makes it clear that XPD, STM, and LEED are a particularly useful and powerful set of surface structure probes when used in the same experimental system to study a given surface. LEED in the simplest form used in most laboratories is primarily sensitive to long-range order, but is not very sensitive to changes in the topography of surfaces, whereas STM is the current technique of choice for studying surface topography, as well as short-range and long-range order. XPD by contrast probes the short-range structure around each type of emitter, including simple-to-interpret forward scattering effects in some diffraction features, and it also has the advantage over the other two techniques of being atom-specific. This study beautifully confirms the need for complementary surface structure probes in such epitaxial growth studies.

Looking to possible future areas of study suggested by this thesis, we point out that many epitaxial growth problems could fruitfully be studied with the experimental system that was constructed as part of this thesis. Indeed, various aspects of the FeO_x/Pt(111) system studied here are worthy of further investigation: for example, comparing oxide

layers grown as we have done and by the layer-by-layer method, and studying more carefully the columnar oxide growth for coverages less than one monolayer. Beyond the exciting prospects opened up by this instrumentation, new high-brightness synchrotron radiation sources and higher resolution electron spectrometers yield energy resolutions at least 10 times better than those achieved here. This could permit the deconvolution of the two different Fe oxidation states involved in these oxides, provided that the natural width of the Fe peak is not too large, and then chemical-state specific XPD would provide a much more precise understanding of the structures in this system. Another desirable development would be the addition of the surface magneto optic Kerr effect (SMOKE) as yet another complementary technique to this new instrument to permit directly measuring the magnetization in these iron oxide films. The application of this kind of instrumentation to a wide variety of other problems in the epitaxial growth of metal oxides and other surface structure problems should certainly be fruitful as well.

APPENDIX A

XPS QUANTITATIVE ANALYSES

We begin by introducing standard XPS quantitative analytical expressions and applying them to the coverage of Fe as initially deposited, and then consider the Fe:O stoichiometry of the various iron oxides on Pt(111). The initial amount of Fe deposited can be determined to a very good approximation by using well-known formulas applicable to the case of a semi-infinite substrate with uniform overlayer thickness t. From Eq. (3) of ref. [1], the dependence of the substrate and overlayer intensities on polar angle θ can be expressed as:

Peak k from substrate with $E_{kin} \equiv E_k$:

$$N_k(\theta) = I_o\Omega_o(E_k)A_o(E_k,\theta)D_o(E_k)\rho_k(d\sigma_k/d\Omega)\Lambda_e(E_k)\exp(-t/\Lambda_e'(E_k)\sin\theta)$$
$$= N_k^{\infty}(\theta)\exp(-t/\Lambda_e'(E_k)\sin\theta), \quad (1)$$

Peak l from overlayer with $E_{kin} \equiv E_l$:

$$N_l(\theta) = I_o\Omega_o(E_l)A_o(E_l,\theta)D_o(E_l)\rho_l(d\sigma_l/d\Omega)\Lambda_e'(E_l)[1-\exp(-t/\Lambda_e'(E_l)\sin\theta)]$$
$$= N_l^{\infty}(\theta)[1-\exp(-t/\Lambda_e'(E_l)\sin\theta)] \quad (2)$$

where

I_o = the incident x-ray flux

Ω_o = the kinetic-energy-dependent effective solid angle seen by the spectrometer

A_o = the kinetic-energy- and angle- dependent effective specimen area seen by the spectrometer

D_o = the kinetic-energy-dependent efficiency of the detector

$d\sigma_{k,(l)}/d\Omega$ = the differential cross section, which depends on the subshell k(or l) and the photon energy

Λ_e = the inelastic attenuation length in the substrate

Λ_e' = the inelastic attenuation length in the overlayer

ρ_k = an atomic density in the substrate associated with subshell k

ρ_l = an atomic density in the overlayer associated with subshell l, and

N_k^∞ and N_l^∞ = the absolute peak intensities at a certain θ resulting from atomically clean and semi-infinite specimens of the substrate and overlayer material, respectively (in our case N_k^∞ for Pt, N_l^∞ for Fe), and given by:

$$N_k^\infty = I_o\Omega_o(E_k)A_o(E_k,\theta)D_o(E_k)\rho_k(d\sigma_k/d\Omega)\Lambda_e(E_k) \quad (3)$$

$$N_l^\infty = I_o\Omega_o(E_l)A_o(E_l,\theta)D_o(E_l)\rho_l(d\sigma_l/d\Omega)\Lambda'_e(E_l). \quad (4)$$

It is also convenient to rearrange the above equations so as to deal with peak ratios in which the x-ray intensity I_o and any purely instrumental variations with θ cancel:

Overlayer/substrate ratio:

$$R(\theta) \equiv \frac{N_l(\theta)}{N_k(\theta)} = \frac{N_l^\infty}{N_k^\infty}[1-\exp(-t/\Lambda'_e(E_l)\sin\theta)]\exp(t/\Lambda'_e(E_k)\sin\theta) \quad (5)$$

where $N_k(\theta)$ and $N_l(\theta)$ are the measured peak intensities of substrate and overlayer at a certain coverage, respectively. Eq. (5) can be used as to experimentally calibrate the determination of initially-deposited Fe coverages by plotting $N_l(\theta)/N_k(\theta)$ versus t after N_k^∞ and N_l^∞ are determined either experimentally or theoretically.

We first discuss the experimental results for thick films and compare them with theoretically determined ones to calibrate our method of measuring peak intensities. We first deposited a thick Fe film (~ 40 ML) on a Pt(111) substrate so as to measure N_l^∞, the absolute intensity of Fe $2p_{3/2}$ from an effectively semi-infinite sample of Fe. No Pt signal was seen from this overlayer, verifying that it was effectively semi-infinite for photoelectron emission. Immediately afterward, the Fe was flashed off to leave an atomically clean Pt(111) surface, and N_k^∞ was measured through Pt 4f spectra. In order to minimize possible errors in the Pt intensity due to photoelectron diffraction effects, both the Pt 4f and Fe $2p_{3/2}$ intensities were measured at an emission direction (θ,ϕ) for which the Pt 4f peak intensity is equal to the average over a full azimuthal scan data for

that particular polar angle. Photoelectron diffraction effects in the Fe overlayer could be ignored, as this overlayer produced a featureless LEED pattern indicating no long-range order and a polycrystalline film.

Fig. A.1 shows typical spectra taken in this calibration process: Fe $2p_{3/2}$ in (a), Pt 4f in (b), and O 1s in (b). For all cases, a simple linear background has been subtracted from the spectra to obtain the Fe $2p_{3/2}$:Pt 4f or :O 1s intensity ratios for determining the coverage of the initially deposited Fe, or the Fe:O stoichiometry for the oxide overlayers after oxidation of Fe. The Fe $2p_{3/2}$ "area" shown in this figure is clearly somewhat arbitrary in definition, as the entire $2p_{1/2,3/2}$ region has lying under it a significant background extending over about 50 eV, and the intensities of the two members of this doublet no doubt overlap one another appreciably in this region. The Fe $2p_{3/2}$ intensity measured in this way is thus no doubt an underestimate, but this can easily be adjusted for with the present calibration procedure. The areas for Pt 4f and O 1s shown in Fig. A.1(b) are closer to representing true intensities. However, the calibration procedure we will use only requires that the areas we measure for both Fe and Pt be proportional to the true intensities. The experimental N_l^∞/N_k^∞ ratio determined by measuring the Fe $2p_{3/2}$ and Pt 4f peak intensities as described above is found to be 0.539. Using this value together with Λ_e' (Fe $2p_{3/2}$) in Fe of 13.42 Å and Λ_e' (Pt 4f) in Fe of 21.06 Å, as obtained from theoretical data in ref. [A.6], the initially-deposited Fe coverages can be determined from Eq. (5) by plotting $N_l(\theta)/N_k(\theta)$ versus t. The results obtained for Fe layer thicknesses in this way are in very good agreement with those from the quartz crystal monitor, as shown in Table 3.1. Only for the thickest nominal 3.0 ML layer there is about 20% disagreement between the QCM and XPS results; this can possibly be explained as due to diffraction effects. As the Fe coverage increases, diffraction effects can be more pronounced due to the possible short-range order and island formation even though LEED patterns at this coverage indicate no long-range order.

Now we discuss the theoretical determination of the N_l^∞/N_k^∞ ratio as both a cross-check, but more as a calibration, of the experimentally determined one. By contrast with the experimental determination, in which any purely instrumental variations were canceled out for the substrate and the overlayer, there are a few terms we have to take into account in a theoretical determination of the absolute peak intensity ratio. The two terms, I_o and A_o, are canceled out because the incident x-ray flux and the effective specimen area can be assumed to be identical for the substrate and the overlayer peaks. However, the kinetic energy dependent instrumental transmission function $T(E_{kin})$, which is represented by the combined product $\Omega_o(E_{kin})D_o(E_{kin})$, has to be determined with the same spectrometer optical parameters (in this case, a ± 3.0° tube-array angular baffle [A.3] and a 2 mm x 20 mm curved entrance slit) for the two different photoelectron peaks and kinetic energies involved. It is also well known that $T(E_{kin})$ is simply proportional to $(E_{kin})^{-q}$ [A.4]. The exponent q in the latter expression was experimentally determined and found to be 0.74 by measuring the Pt 4f peak intensities as the analyzer pass energy was varied from 5 eV to 100 eV, using a procedure described previously [A.4]. This value of 0.74 agrees well with the previously determined ones on the same spectrometer which range from 0.70 (with ± 3.0° aperture angular baffle) to 0.78 (with ± 1.5° tube-array angular baffle). The ratio of $T = \Omega_o D_o$(Fe $2p_{3/2}$:Pt 4f) determined with the above calibration is ~1.557 (The proportional values for Pt 4f and Fe $2p_{3/2}$ are $4.63\text{x}10^{-3}$, and $7.21\text{x}10^{-3}$, respectively). The remaining factors to be determined are the differential cross sections of Fe $2p_{3/2}$ and Pt 4f for unpolarized radiation. These can be calculated from a knowledge of the total subshell cross section σ_k and the asymmetry parameter β_k via

$$\frac{d\sigma_k}{d\Omega} = \frac{\sigma_k}{4\pi}[1+\beta_k(\frac{3}{2}\sin^2\alpha - 1)].$$

The σ_k and β_k values for the calculations are obtained from ref. A.5 and the calculated differential cross sections for Pt 4f and Fe $2p_{3/2}$ with $\alpha = 48°$ are 1.165 $x10^{-2}$ and 1.030 x 10^{-2} Mbarns, respectively. The remaining parameters are the attenuation lengths for Pt 4f in Pt: 11.36 Å [A.2], and for Fe $2p_{3/2}$ in Fe:13.42 Å [A.6]. The IMFP's are based on experimental data for Pt and theoretical calculations for Fe. Finally, the atomic concentration in 10^{22} cm^{-3} of Pt (6.62) and Fe (8.50) are used for the calculation. With these inputs, the theoretically determined N_l^∞/N_k^∞ ratio is found to be 1.47 which is 2.73 times larger than the experimentally determined ratio using the area determination procedure in Fig. A.1. Although this is at first sight a large deviation between experiment and theory for nominally the same ratio, we have already noted that the Fe 2p spectral region has an anomalous background under it over an extended region, and this has been seen in prior studies of elemental iron in other laboratories [e.g., the Physical Electronic Handbook of XPS Spectra-A.7]. Our simplistic area determination procedure also clearly does not allow for the overlap of peak-plus-background between the $2p_{1/2}$ and $2p_{3/2}$ intensities, thus underestimating the latter by a significant amount. In addition, the background under both regions of the spectrum seem to at least partially be due to many-electron satellite excitations related to the Doniach-Sunjic lineshape [A.8], and thus represent intensity that is properly associated with the primary photoelectron excitation. This intensity thus should be included in measuring a ratio for comparison to the theoretical number above, and is another reason for the factor of 2.73 between experiment and theory.

As noted above, the coverage determination of initially deposited Fe before oxidation by XPS quantitative analysis is in very good agreement with the results of QCM because any spurious reduction of the Fe $2p_{3/2}$ peak area, as well as other possible errors, are calibrated away, as discussed above. In now proceeding to determine the Fe:O stoichiometry of the oxide films, we can use a somewhat simpler approach due to the

weak attenuation in the overlayer. Here, we have used equations appropriate for a semi-infinite substrate with a thin, weakly-attenuating overlayer. The fractional coverage of Fe and O with respect to Pt can be expressed [from ref. 1]:

$$\left[\frac{s'}{s}\right] = \frac{N_l(\theta)}{N_k(\theta)} x \frac{D_o(E_k)\Omega_o(E_k)A_o(E_k)(d\sigma_k/d\Omega)\Lambda_e(E_k)\sin\theta}{D_o(E_l)\Omega_o(E_l)A_o(E_l)(d\sigma_l/d\Omega)d} \exp(t/\Lambda'_e(E_k)\sin\theta) \quad (6)$$

where [s'/s] is the fractional monolayer coverage of atomic species in which peak *l* originates (Fe and O in this case) and d is the mean separation between layers on the substrate (2.26 Å for the case of the (111) planes of Pt). All of the other factors are the same as explained above. We have here added a first-order correction factor of $\exp(-t/\Lambda'_e(E_k)\sin\theta)$ to a more standard result for a non-attenuating overlayer in order to allow for the weak attenuation of Pt 4f in the iron oxide overlayer at these high kinetic energies.

The same input parameters given above are still valid except that we now need new attenuation lengths in iron oxide films instead of in pure Fe films, as well as new parameters to describe the O 1s intensity, which are: $\Omega_o D_o$(O 1s) = 6.18 x 10^{-3}, $d\sigma_k/d\Omega$ (O 1s) = 2.612 x 10^{-3} Mbarn [from ref. 5], Λ'_e (Pt 4f in the oxide) = 39.1 Å, Λ'_e (O 1s in the oxide) = 33.1 Å, Λ'_e (Fe $2p_{3/2}$ in the oxide) = 30.3 Å [A.6]. The attenuation lengths were calculated from formulas by Tanuma et al [A.6] that can be applied to a material with arbitrary stoichiometry and density, and we here assumed an FeO stoichiometry, although changing the latter choice to Fe_3O_4 is expected to make little difference. This calculated value is in good agreement with the experimental value [A.9,10]: the only available IMFP experimental data for an iron oxide film, to our knowledge, is 23 Å for an O Auger kinetic energy of 515 eV in a ferro-alloy surface and the calculated IMFP for the electron kinetic energy of 515 eV in an FeO film is about 25 Å. With these input

parameters substituted into Eq. 6, the Fe:O stoichiometry [s'(Fe)/s'(O)] can be expressed as:

$$\left[\frac{s'(Fe)}{s'(O)}\right] = 0.218x\frac{N_{Fe}(\theta)}{N_O(\theta)} \tag{7}$$

where $N_{Fe}(\theta)$ and $N_O(\theta)$ are the measured intensities for Fe $2p_{3/2}$ and O 1s, respectively, with the assumption that all processes resulting from the primary photoelectron excitation have been included. However, our calibration of actual experimental intensity ratios against the limit of thick Fe and clean Pt indicates that the experimental ratios need to be multiplied by a factor of 2.73, provided we assume that both the Pt and O intensities in the denominator are being correctly measured, so that this correction factor deals with Fe alone, yielding a final empirically-corrected formula for stoichiometry of

$$\left[\frac{s'(Fe)}{s'(O)}\right] = 0.595x\frac{N_{Fe}(\theta)}{N_O(\theta)}.$$

Using the first formula without correction in fact yields Fe:O stoichiometries of ~1:3 to ~1:4 for all of our oxide films that are not consistent with any known iron oxide! With the second corrected formula, the Fe:O stoichiometries of the 1.0 ML and 3.0 ML iron oxide films are found to be very close to 1:1 (FeO) and 1.0:1.33 = 3:4 (Fe_3O_4), respectively. These results are summarized in Table 3.1.

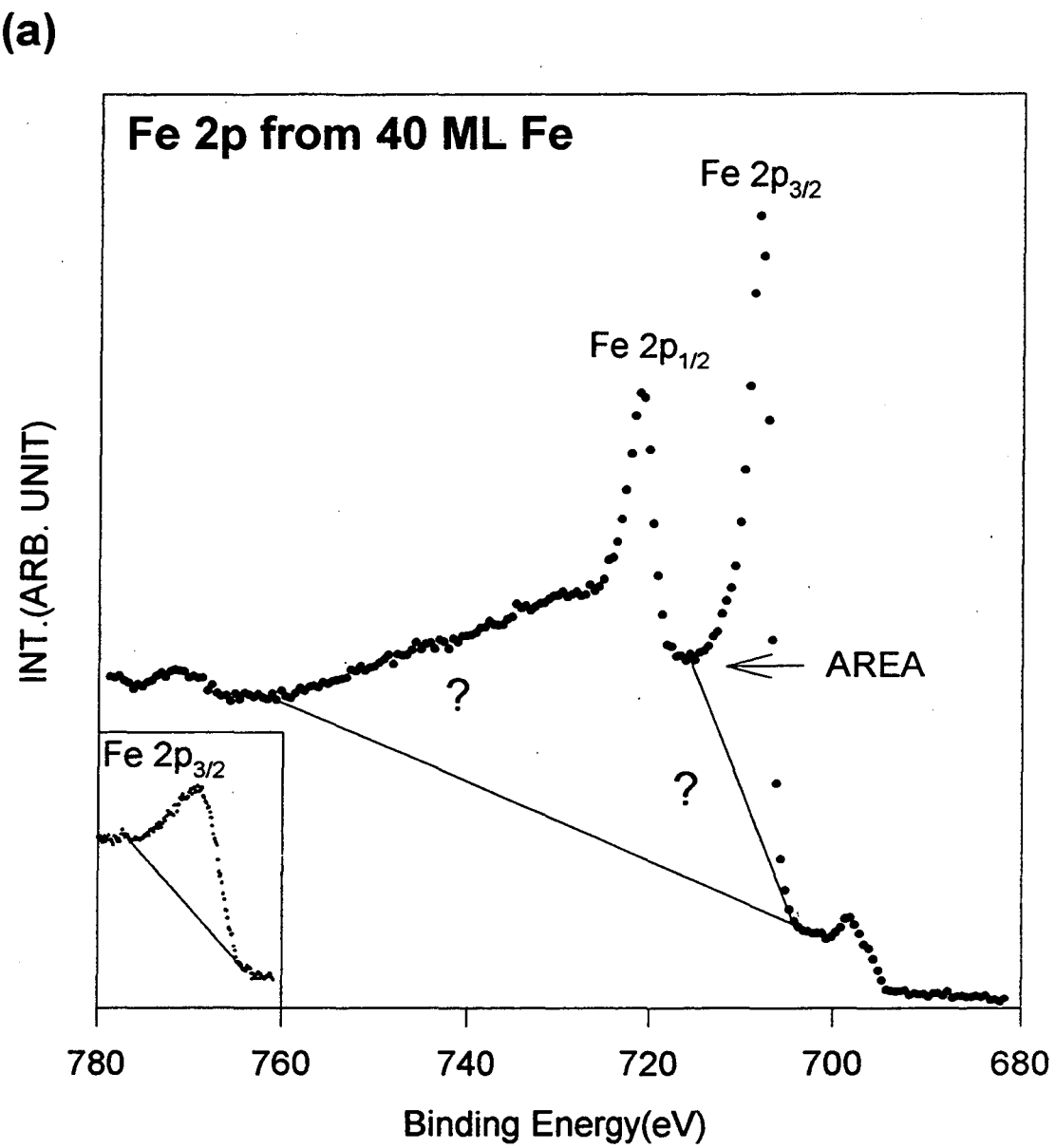

Fig. A.1. (a) Fe 2p XPS spectra of obtained from a 40 ML-thick clean Fe film. The Fe $2p_{3/2}$ peak area as we measured it is shown above the linear background. Note the high background under both components of the Fe 2p doublet, some of which represents primary photoelectron excitation rather than purely inelastic losses. The inset shows just the Fe $2p_{3/2}$ peak and its assumed linear background as obtained from an iron oxide film of 1.0 ML thickness.

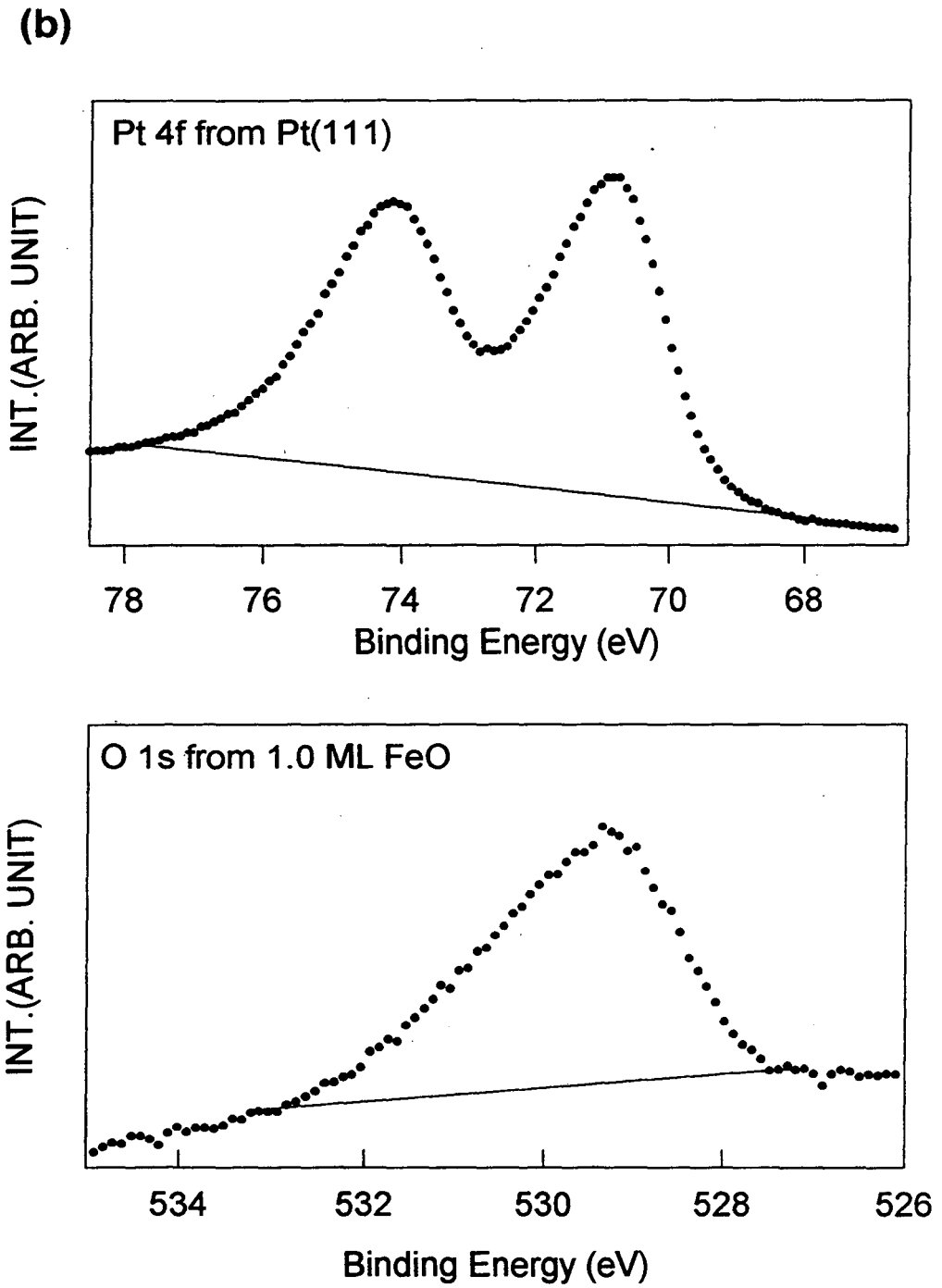

Fig. A.1. (b) Pt 4f and O 1s XPS spectra obtained from an iron oxide film of 1.0 ML thickness. Note the cleaner background characteristics compared to the Fe 2p spectral region.

REFERENCES

[A.1] C.S. Fadley, Prog.in Surf. Sci. 16, 275 (1984)

[A.2] B. Lesiak, A. Jablonski, Z. Prussak, and P. Mrozek, Surf. Sci. 223, 213 (1989)

[A.3] R.C. White, C.S. Fadley, R. Trehan, J. Electron Spectrosc. Relat. Phenom. 41, 95 (1986)

[A.4] J. Osterwalder, M. Sagurton, P.J. Odrers, C.S. Fadley, B.D. Hermsmeier, and D.J. Friedman, J. Electron Spectrosc. Relat. Phenom. 48, 55 (1989)

[A.5] Yeh and I. Lindau, Atomic Data and Nuclear Data Tables 32, 1 (1985)

[A.6] S. Tanuma, C.J. Powell, and D.R. Penn, Surf. Interface Anal. 17, 911 (1991)

[A.7] J.F. Moulder, W.F. Stickle, P.E. Sobol, and K.D. Bomben, Handbook of X-ray Photoelectron Spectroscopy, Perkin-Elmer Corporation, (J. Chastain, ed.) (1992)

[A.8] S. Doniach and M. Sunjic, J. Phys. C3, 285 (1970)]

[A.9] P.B. Needham, Jr., T.J. Driscoll, and N.G. Rao, Appl. Phys. Lett. 21, 10 (1972)

[A.10] P.B. Needham, Jr. and T.J. Driscoll, J. Vac. Sci. Technol. 11, 278 (1974)

APPENDIX B

XPD THREEFOLD DATA FOLDING

The validity of the threefold-symmetry data folding used to yield the full 2π XPD patterns reported in this dissertation was checked for each case by comparing the individual 120° intensity scans in the large data set to selected full 360° azimuthal XPD scans. As one example of this, a selected full 360° scan and a threefold-folded scan are shown in Fig. B.1 for the case of Fe $2p_{3/2}$ emission from ML FeO/Pt(111). The full azimuthal XPD data clearly show the same threefold symmetry as the folded data, illustrating the excellent alignment of the specimen in the goniometer and justifying the use of this procedure.

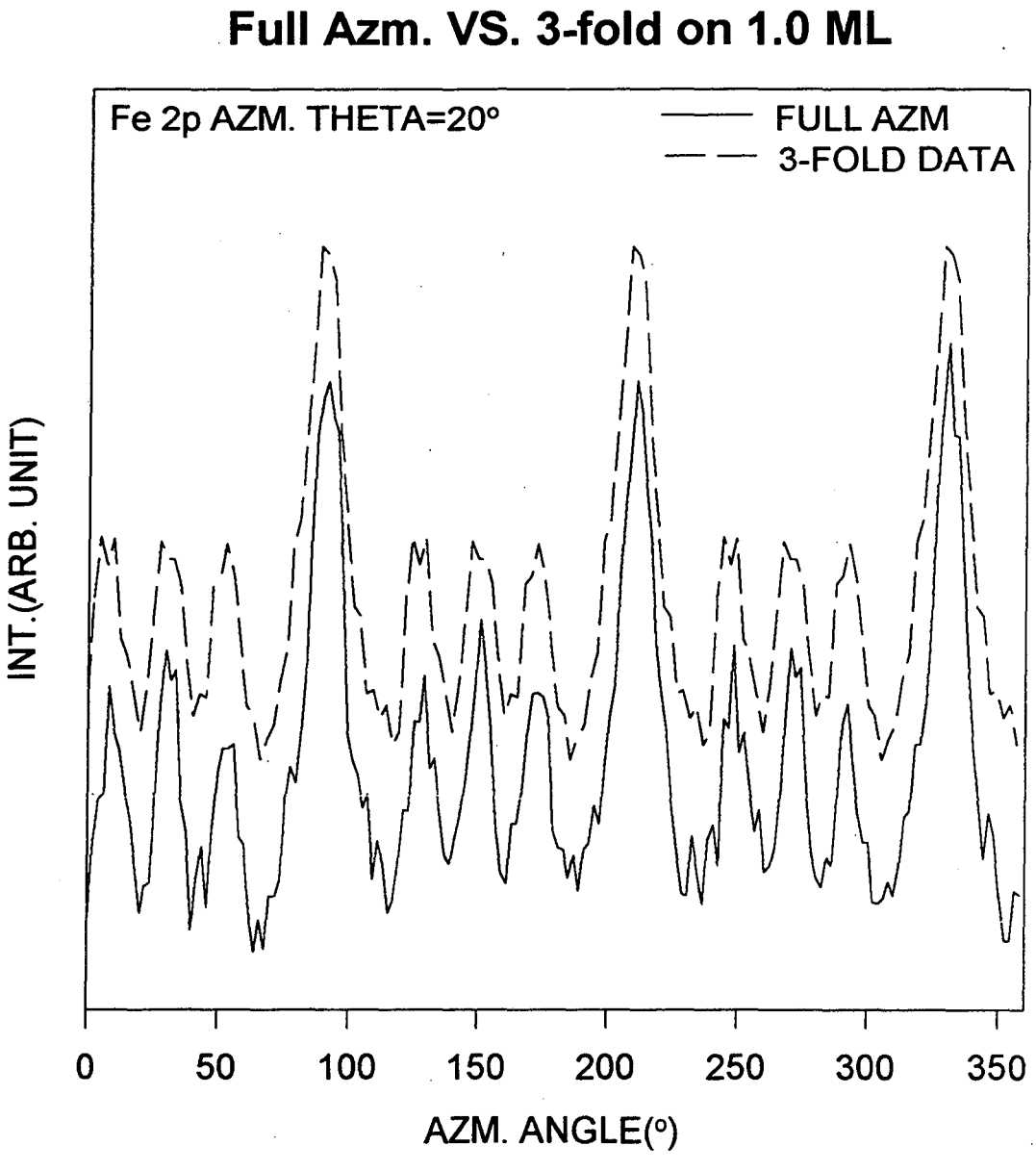

Figure B.1. The selected full and threefold data folded Fe $2p_{3/2}$ emission XPD data are shown for the case of 1 ML FeO/Pt(111).

APPENDIX C

SIMULATIONS OF LEED PATTERNS

For a well ordered surface, a LEED pattern consists of a set of spots, each of which can be associated with one of the reciprocal lattice vectors describing the periodicity of the surface. The LEED pattern for ~1 ML FeO/Pt(111) exhibits a three-fold symmetric hexagonal pattern where each of the six main spots is surrounded by a rosette of six satellite spots, as shown in Fig. 3.2. These six satellite spots, originating from the longer-range periodicity of the iron oxide overlayer discussed in Chapter 3, are somewhat streaked in the regime of ≤ 1 ML compared to those of the higher coverages.

The goal of our LEED simulation is to semi-quantitatively understand these streaked six satellite spots, as well as to use the calculated patterns to better understand the real-space atomic distances involved. However, exact simulations of LEED spot patterns for such large unit cells, including a quantitative prediction of the intensity ratios of the spots, are beyond our computational capabilities. This is because of the large cluster size and the fact that multiple scattering effects must be included in order to adequately reproduce the LEED patterns, especially the six satellite spots that are associated with multiple scattering between the overlayer and the substrate. In fact, we know of no program for carrying out such calculations in a fully quantitative way in a finite amount of time. In order to overcome this limitation, we have employed a phenomenological model in which the various atomic scattering factors in the Fe layer and the first Pt substrate layer are modulated in the same way as the superlattice modulations seen in the STM. The O layer was not included for simplicity. If the reciprocal lattice vectors describing the superlattice unit cell are given by $\mathbf{A}^*$ and $\mathbf{B}^*$ (and calculable from the equation to LEED given in the Introduction), this modulation F was taken to have the form:

$$F = \left\{1 + \frac{f}{2}\left[\cos(\mathbf{A}^* \cdot \mathbf{r}_i) + \cos(\mathbf{B}^* \cdot \mathbf{r}_i)\right]\right\},$$

where $0 \leq f \leq 1$ and was adjusted to about 1.0 to yield easily discernible superlattice effects on the predicted LEED patterns, F thus can be varied by a maximum of from 2 to 0 over the modulation, and $\mathbf{r}_i$ is the position vector of the i^{th} scatterer in the cluster, whether Fe or Pt for this case. The LEED intensity simulation was then carried out within a single scattering model (ref. [21] in Chapter 4).

Fig. C.1 shows the calculated LEED spot patterns for this Fe/Pt(111) superlattice with the registry of Fig. 3.2(c) and for different cluster sizes, as threefold symmetrized in the final step: (a) a circular cluster of 200 Å diameter to include about 8 superlattice repeat units in both of the lateral directions x and y; (b) a rectangular cluster 200 Å long in x and 26 Å wide in y to simulate the columnar oxide growth of 0.75 ML as seen in the STM image of Fig. 3.3(a) and with ~ 8 and ~2 superlattice repeating units on x and y directions, respectively; and (c) a cluster with diameter of 30 Å and only about 2 superlattice cells in both directions. Only a band of intensity spanning the most intense spots and their satellites was calculated due to the computer-intensive nature of these calculations. The calculated LEED pattern for (a), a simulation for the case of long-range order over fairly large area, reproduces the six main spots as well as the six satellite spots. Furthermore, the distances between the main spots and the satellite spots well reproduce the experimental ones, and further confirm the large periodicity of ~ 26 Å seen by LEED and STM. A minor point of disagreement is that the outermost six spots associated also with Pt(111) are brightest, whereas in experiment, the six spots in the center of the satellite ring and associated with FeO(111) are the brightest. However, for a calculation at this simple and phenomenological level, such minor disagreements are not surprising. For the simulation of oxide columnar growth shown in (b), the six satellite spots are still

apparent, although a little weaker compared to the case of (a) and with streaking between them that is qualitatively like that in the experimental data of Fig. 3.2(a), but not as strong in theory as experiment. The least ordered case as shown in (c), and here the satellite spots are still visible but much broader and streaked compared to the other cases. The satellites here begin to look more like those in experiment for $\leq$ 1.0 ML. Interpreting these LEED simulations qualitatively, we can thus say that the streaked satellite spots seen in the experimental data are probably due to diminished long range order in the oxide overlayers. Although multiple scattering calculations for similar clusters including also a topmost O layer and possible surface rumpling would be necessary to analyze these LEED results more quantitatively, the present simple simulations serve to further support the structural model discussed in Chapter 3.

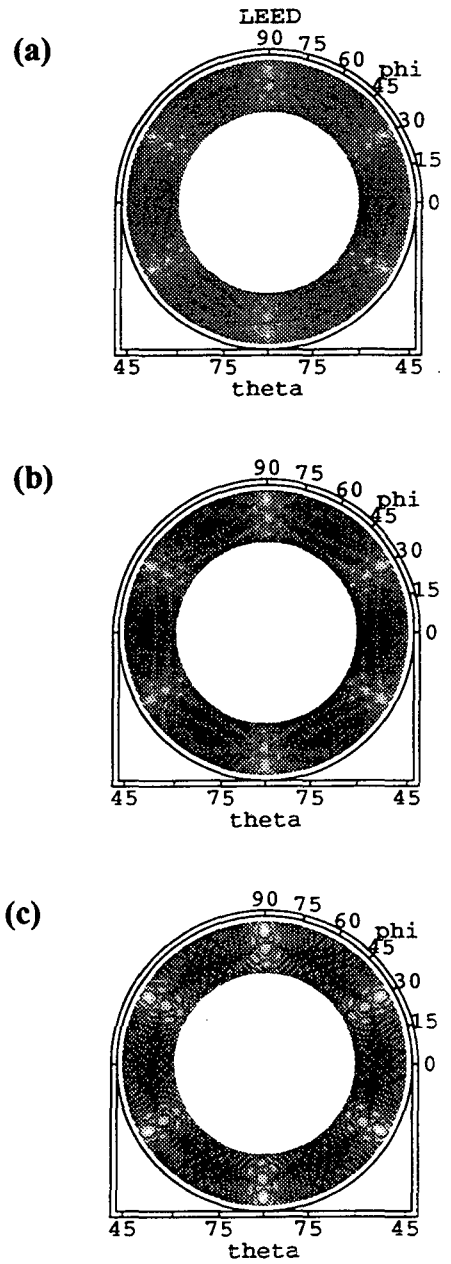

Figure C.1. Calculated LEED patterns for a cluster consisting of Fe on Pt(111) in the same registry as in the FeO(111) superlattice structure of Fig. 3.2(c). (a) is from a large cluster with long-range order, (b) is from a rectangular cluster simulating the columnar oxide growth seen for a coverage less than one monolayer, and (c) is from a small circular cluster simulating minimal long-range order. Further details for each case are given in the text.

APPENDIX D

THETA-DEPENDENT O:Fe PEAK INTENSITY RATIOS: QUANTITATIVE ANALYSIS OF OXIDE SURFACES AND NATURE OF SURFACE TERMINATION

We consider here how the θ-dependent O 1s:Fe $2p_{3/2}$ peak intensity ratios used for quantitatively analyzing oxide stoichiometries were derived from experiment, using as examples the cases of 1.0 and 3.0 ML. These O:Fe peak intensity ratios were derived from each 2π intensity map, as introduced in Chapter 3. At each polar angle, the intensity $I(\theta,\phi)$ was averaged to yield $I_{ave}(\theta)$ for both Fe and O, leading to curves like those shown as solid lines in Fig. D.1(a) for the 1.0 ML case with much reduced, but still non-zero, diffraction modulations in them. Then a spline curve ($I_o(\theta)$) was fit to each of these azimuthally-averaged curves so as to yield the best experimental estimate of: an intensity with minimally diffraction effects in it.

In Fig. D.1(b), we now show two such θ-dependent I_o(O 1s)/I_o(Fe 2p3/2) curves for Fe and O for both the 1.0 ML and 3.0 ML cases. The higher O:Fe peak intensity ratios of 3.0 ML compared to 1.0 ML over the full angle range clearly show the changes in stoichiometry of the iron oxides in going from FeO (1.0 ML) to Fe_3O_4 (3.0 ML). The average ratio over the more error-free range near the surface normal of $60°\leq\theta\leq90°$ was then used with Eq. 7 in Appendix A to derive our best estimate of stoichiometry.

An additional aspect in Fig. D.1(b) of significance is that both curves show the same sort of variation for very low takeoff angles going down to 6°. This suggests an oxygen terminating surface layer in both cases, as an extra 1/4 ML of Fe would be expected to make the ratio for the 3.0 ML case decrease somewhat for low takeoff angles with more surface sensitivity.

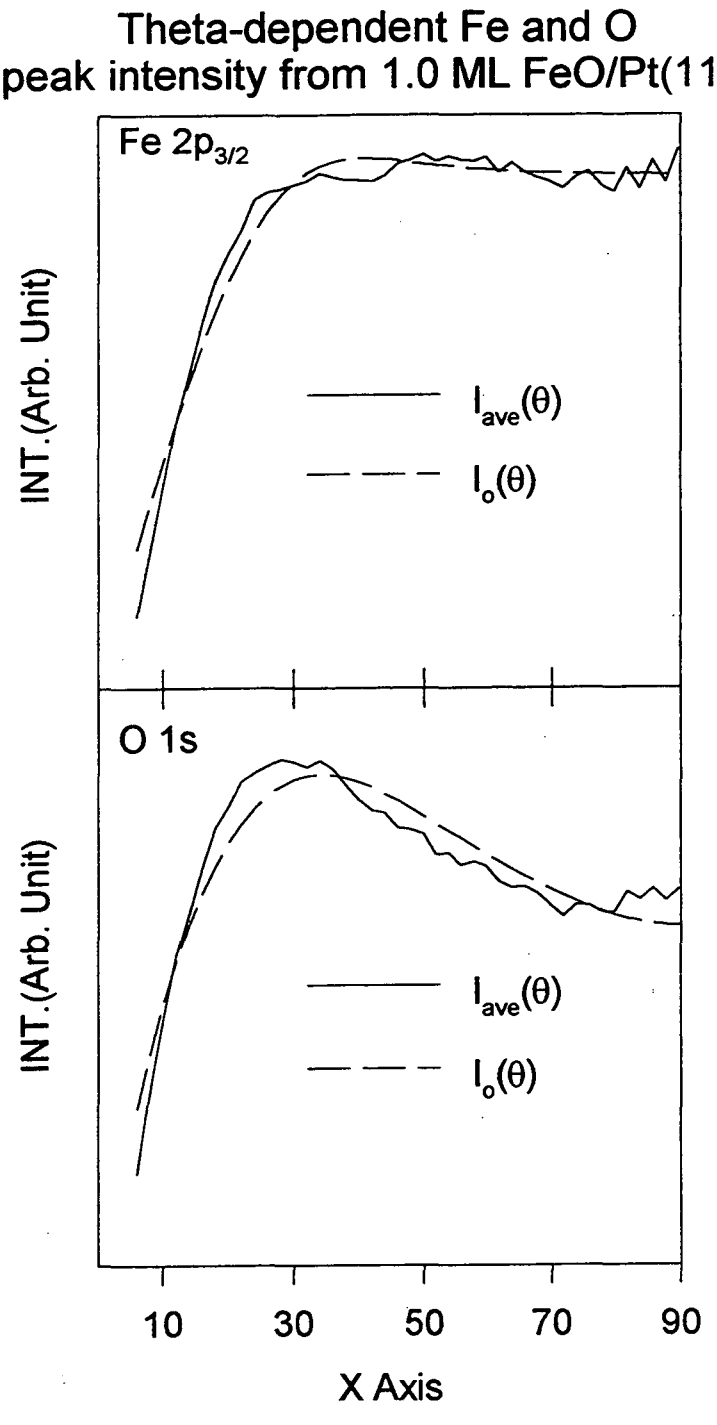

Figure D.1. (a) Azimuthally-averaged O 1s and Fe $2p_{3/2}$ intensities $I_{ave}(\theta)$ for 1.0 ML of iron oxide are shown with the spline fits to this data that are our final estimates of $I_o(\theta)$.

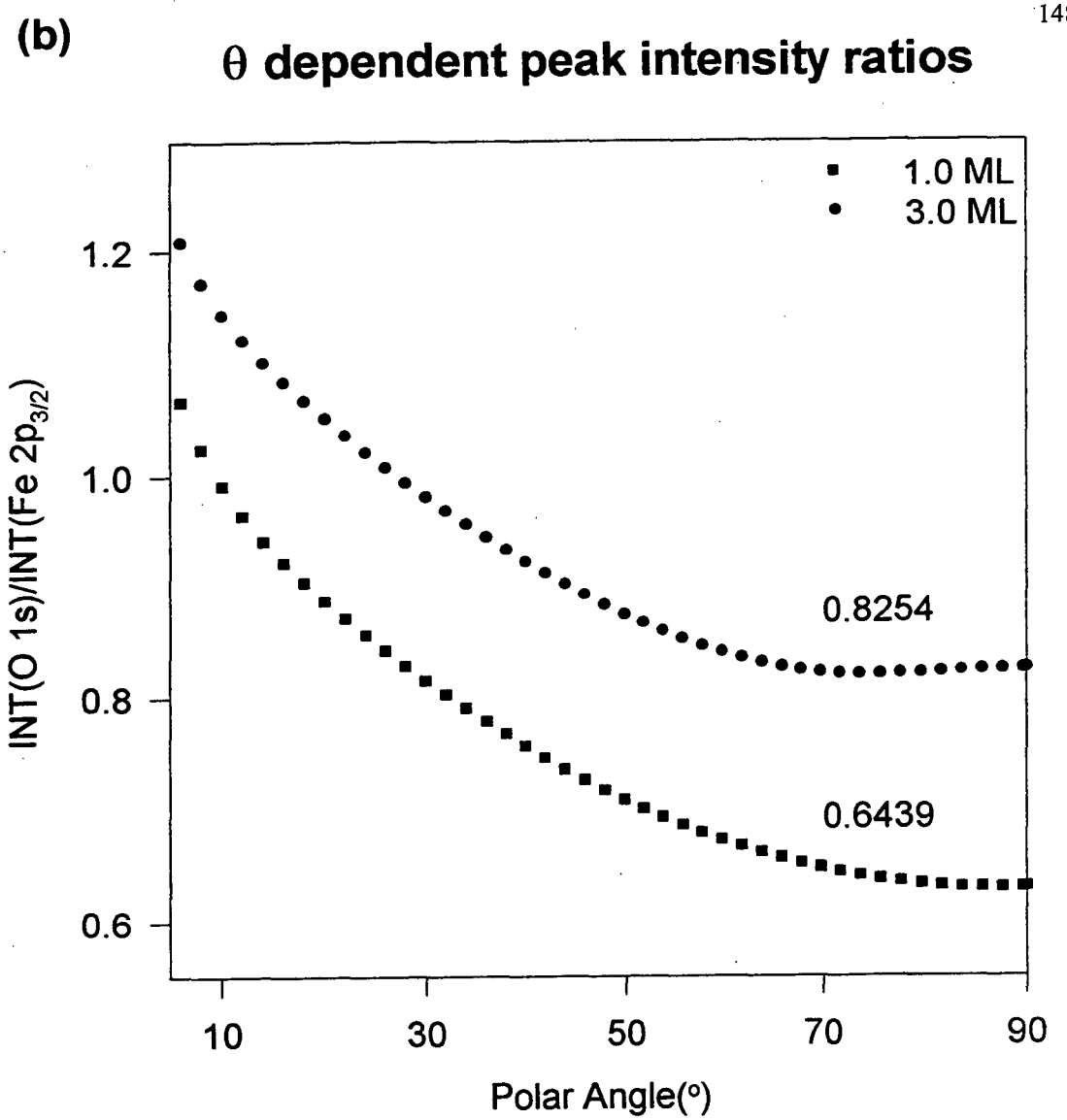

Figure D.1. (b) The θ-dependent O:Fe intensity ratios for 1.0 ML and 3.0 ML of oxide as derived from spline fits such as those in (a). Also the average peak intensity ratios over the most reliable data range of $60° \leq \theta \leq 90°$ are indicated. Note the same trend on both 1.0 ML and 3.0 ML not showing noticeable decreases in O:Fe intensity ratios at the low take-off angles (most surface sensitive regions) in 3.0 ML compared 1.0 ML.

APPENDIX E

STM DATA ANALYSIS

STM images and STM data analysis reported in this dissertation were obtained using the standard Nanoscope II software. Here, two typical features of the software used in calibration of STM piezoes, measurement of vertical and horizontal distances, and determination of the area occupied by islands are illustrated in detail. The most commonly used feature is the display of the cross sectional profile along the chosen line on the STM images which enables us to measure the islands/step heights, for the example case of 0.75 ML oxide, as shown in Fig. E.1.

In Fig. E.1, the line-cut passing across the image clearly shows alternating higher and lower regions and the height difference is found to be ~ 2 Å after the vertical heights (z piezo) are calibrated by factor of 0.63.

The other feature is the display of surface height histograms and bearing ratio curves for the chosen areas on the images which is used to determine the area occupied by islands. The histograms are referenced from the highest point on the area. The bearing ratio curve is the integral of the surface height histogram and plots the total percentage of the surface above a reference plane as a function of the depth of that plane below the highest point.

Figs. E.2 shows the example cases of these features obtained from 1.75 ML oxide. In Figs. E.2, the image of chosen areas are shown in (a), the histograms in (b), and the bearing ratio curve in (c). The histograms clearly shows that there are islands of at least two levels (shows a hint of the third layer growth). Furthermore, the bearing curve provides the following: a topmost islands about 5.0 Å in height as measured from the islands just below and occupying about ~5.5 % of the total area, and a lower set about

9.7 Å in height as measured from the flat base layer and occupying about ~50 % (~58 % if averaged over from wider areas) of the total area.

(a) 0.75 ML

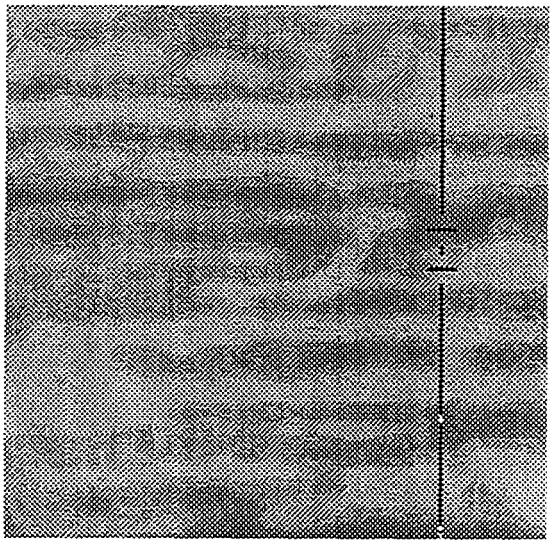

(b)

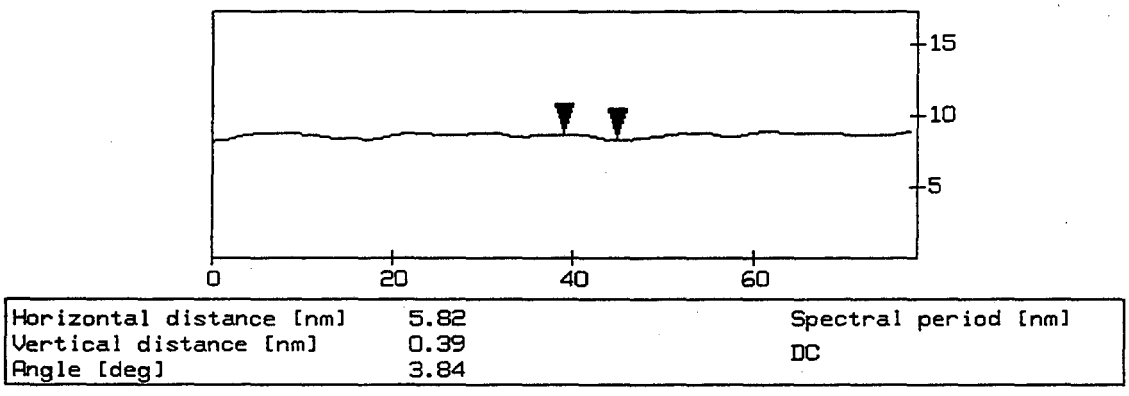

Figure E.1 (a) The STM image obtained from 0.75 ML. (b) The cross sectional profile of the selected line on the image.

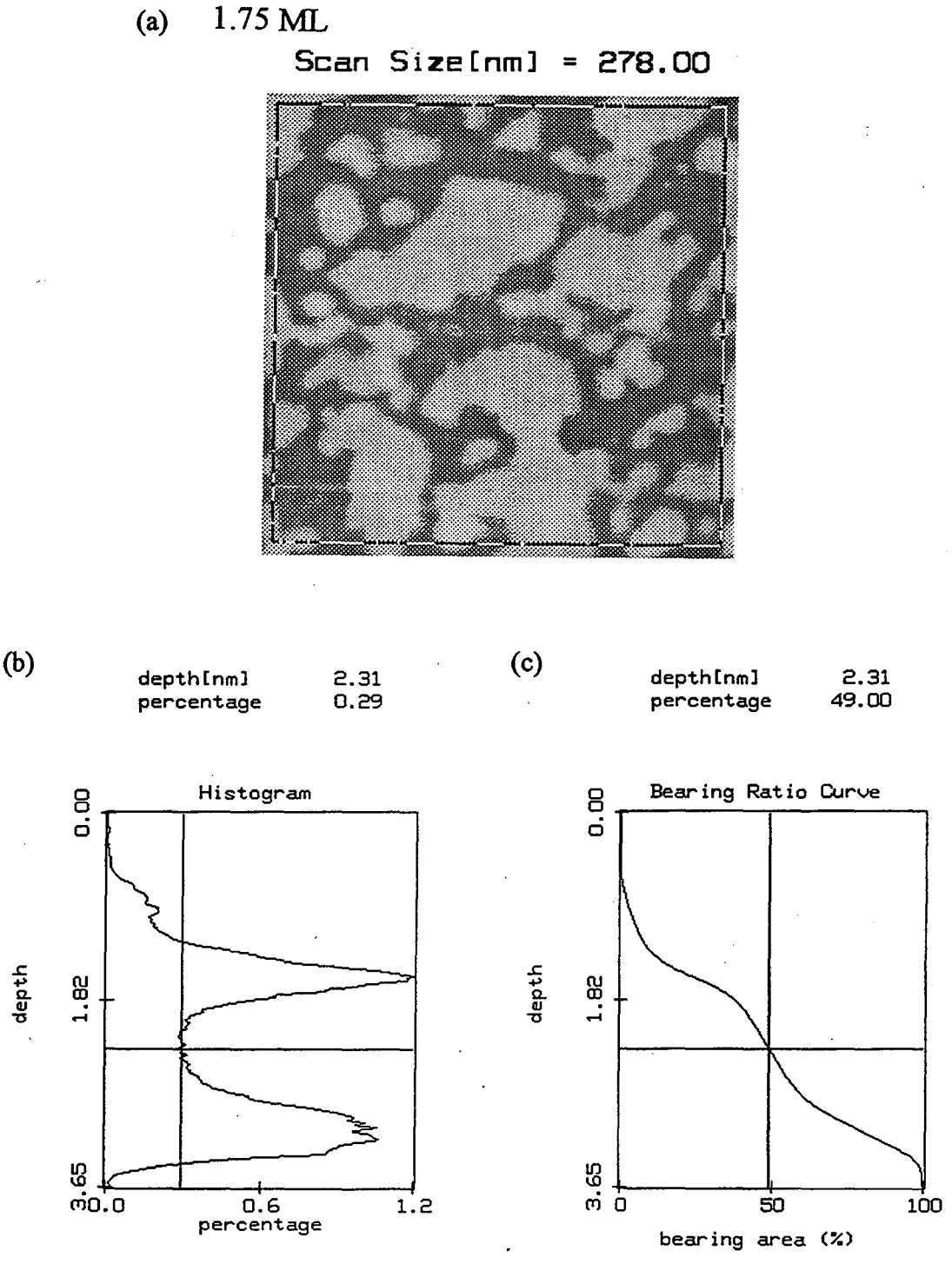

Figure E.2 Illustrating analysis of the occupied area by islands. (a) STM image obtained from 1.75 ML. (b) The surface height histogram on the area of image (a). (c) The bearing ratio curve calculated from the histogram of (b). The vertical heights (z piezo) should be multiplied by a calibration factor of 0.63.

APPENDIX F

AZIMUTHAL XPD SYMMETRIES FOR OXIDE COVERAGES FROM 1.25 ML TO 1.75 ML

Chi curves at a takeoff angle of 20° in Fe $2p_{3/2}$ emission where the strongest forward scattering peaks are present are shown in Fig. F.1 for coverages from 1.25 ML to 1.75 ML. It is clear that the strongest peaks at 1.50 ML are rotated by 60° from $<11\bar{2}>$ azimuths and also show decreased anisotropy compared to those of other two coverages. This we argue could be due to an enhanced importance of another rotated oxide domain for the 1.50 ML case.

In addition, the experimental curves from 3.0 ML of oxide and the theoretical curves from our final optimized model for Fe $2p_{3/2}$ emission at the polar angle of 16° are directly compared in Fig. F.1(b). The theoretical curve well reproduces the positions of the main peaks in the experimental data but with much higher anisotropies. The higher anisotropies in theory can be explained as due to the multilayered structure of the thick iron oxide films at this low takeoff angle, which should result in lower anisotropies in experiment, as discussed in Chapter 4. This expected lower anisotropies in experiment may cause the double bands of intensity to be not as pronounced as in theory, but the experimental curves do in any case show a hint of this double band in one of the two 60° segments repeated in this plot.

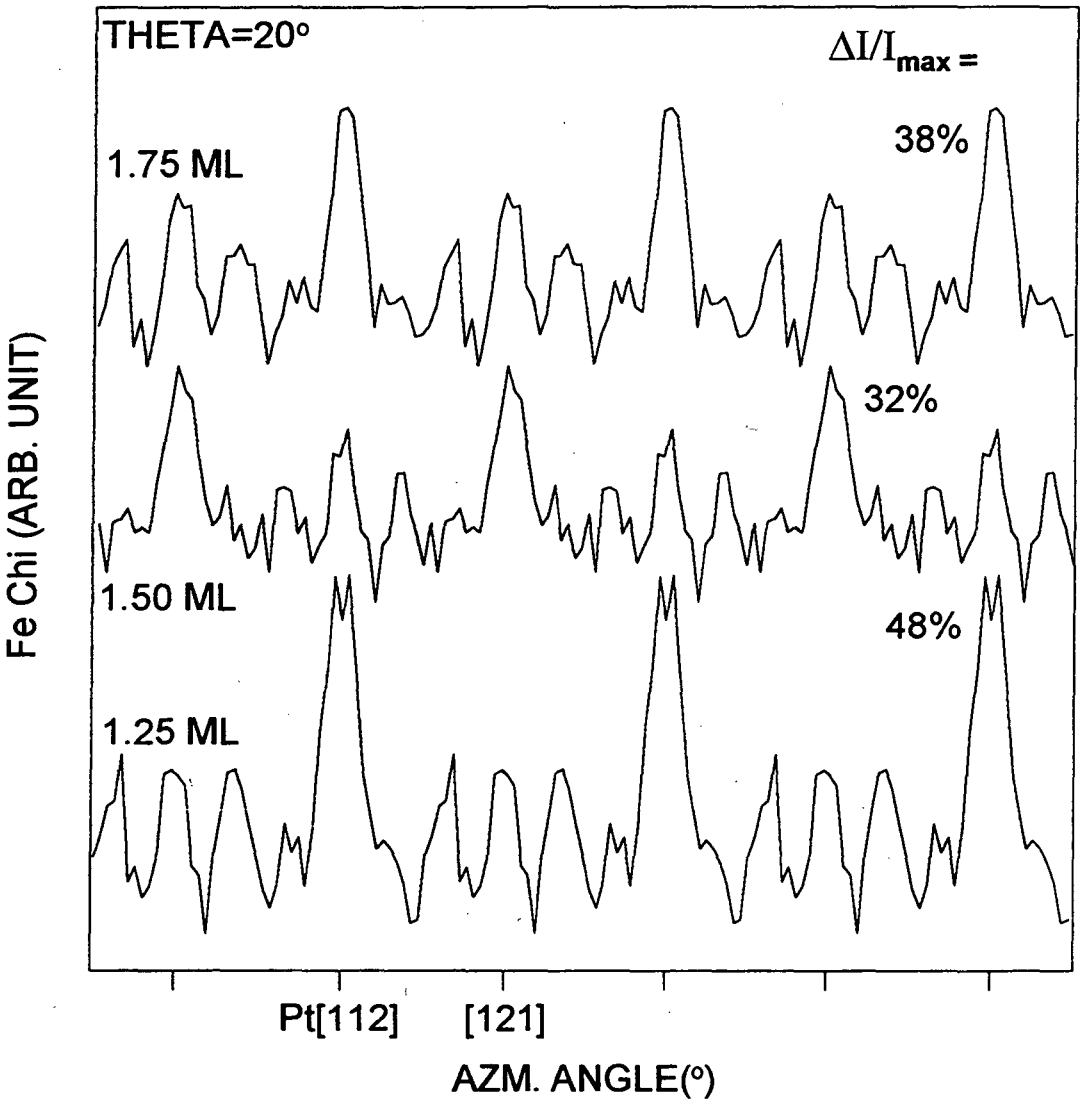

Figure F.1 (a) Fe $2p_{3/2}$ azimuthal chi curves for 1.25 ML, 1.50 ML, and 1.75 ML iron oxide films on Pt(111) at a polar takeoff angle of 20°. Note that the strongest peaks at 1.50 ML are shifted by 60° from $<11\bar{2}>$ azimuths and also show decreased anisotropy compared to the others.

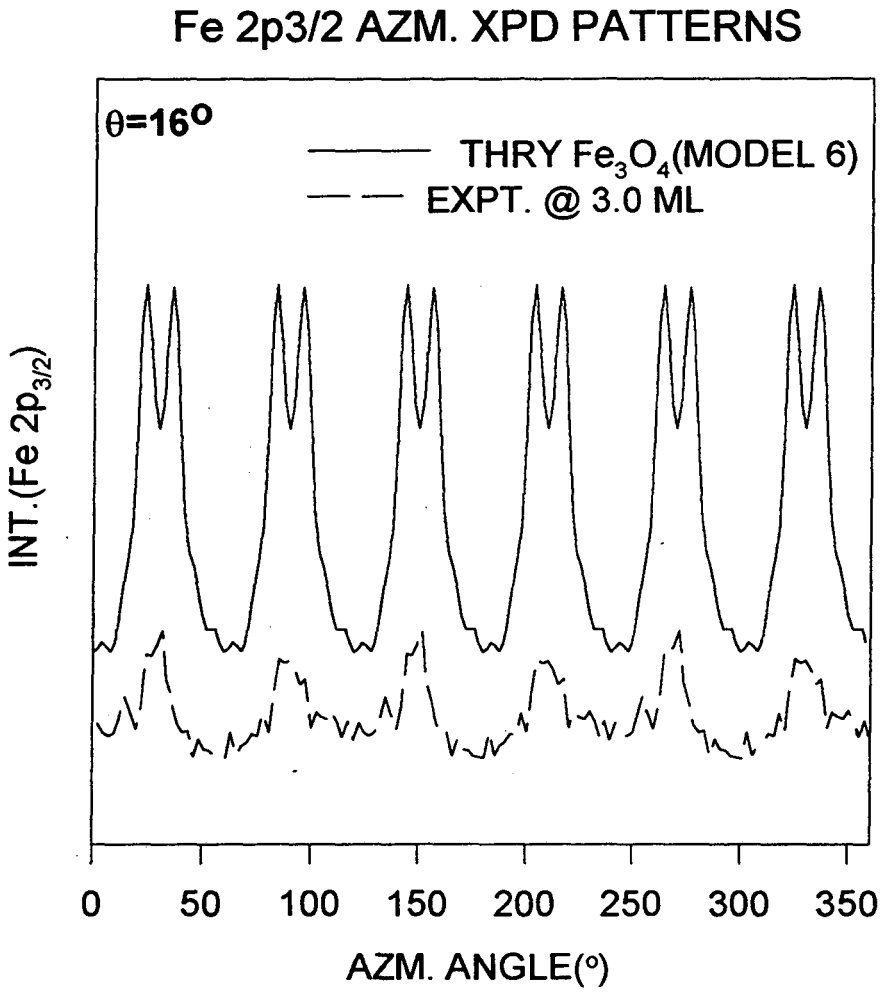

Figure F.1 (b) The experimental and theoretical Fe chi curves obtained from 3.0 ML iron oxide and our proposed structure model (Fe_3O_4 - structure model 6) for an emission angle of $\theta = 16°$.

APPENDIX G

THREEFOLD DATA FOLDING VERSUS FULL AZIMUTHAL SCAN AT 3.0 ML

O 1s and chi curves from selected full and threefold data folded azimuthal scan data obtained from 3.0 ML oxides are shown in Figs. G.1(a) and (b), respectively. For O 1s, both curves show the symmetry being very close to sixfold but slightly threefold in character, with a difference in anisotropy of the two sets of three peaks at the polar angle of about 55° of about 3 %. For Fe $2p_{3/2}$, the two corresponding curves are much more nearly threefold.

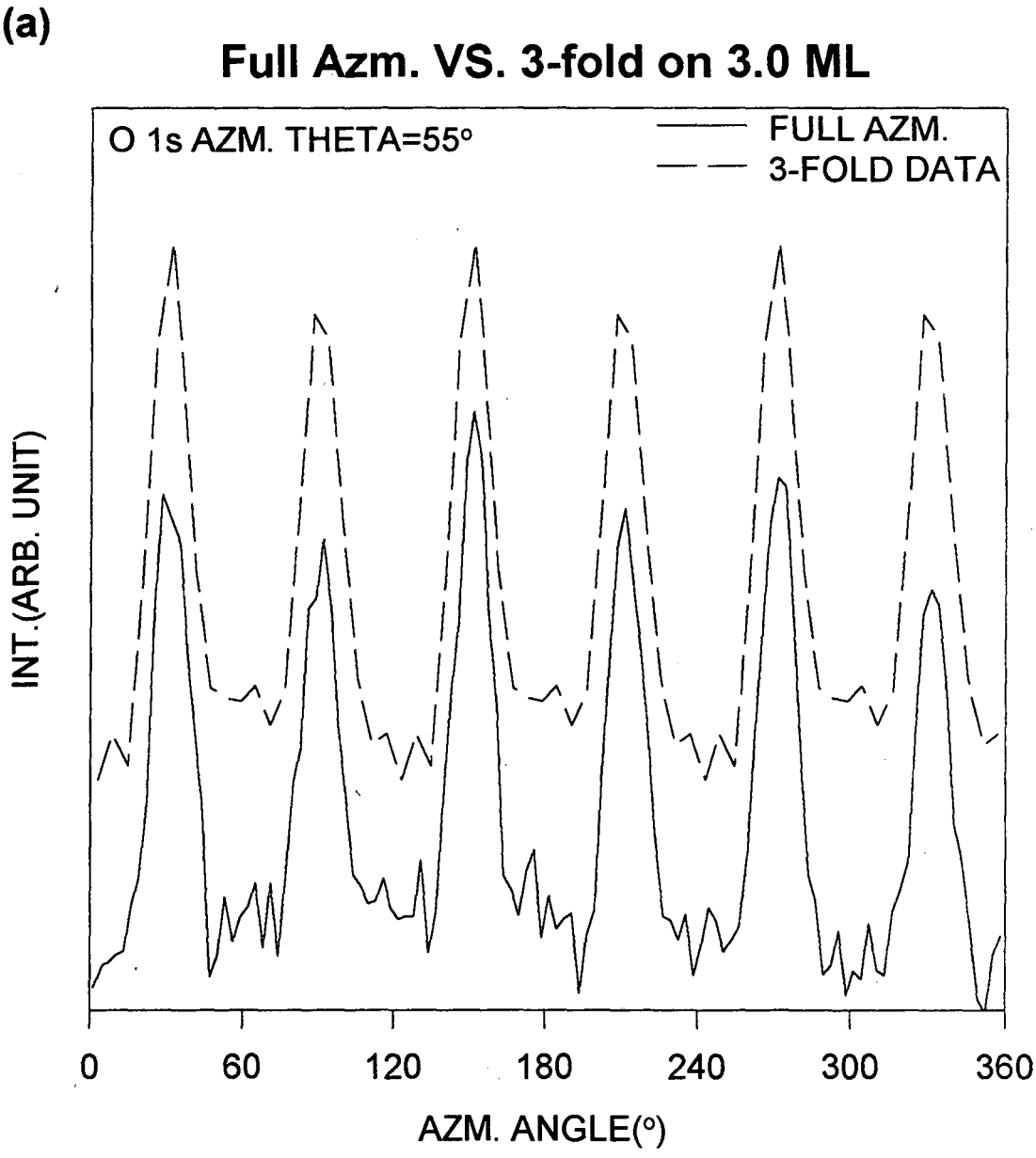

Figure G.1. (a) The O 1s chi curves obtained from 3.0 ML iron oxide on Pt(111) at a polar angle of about 55°. The anisotropy of two sets of three peaks differ from each other by about 3 % resulting in an overall threefold symmetry of the XPD pattern.

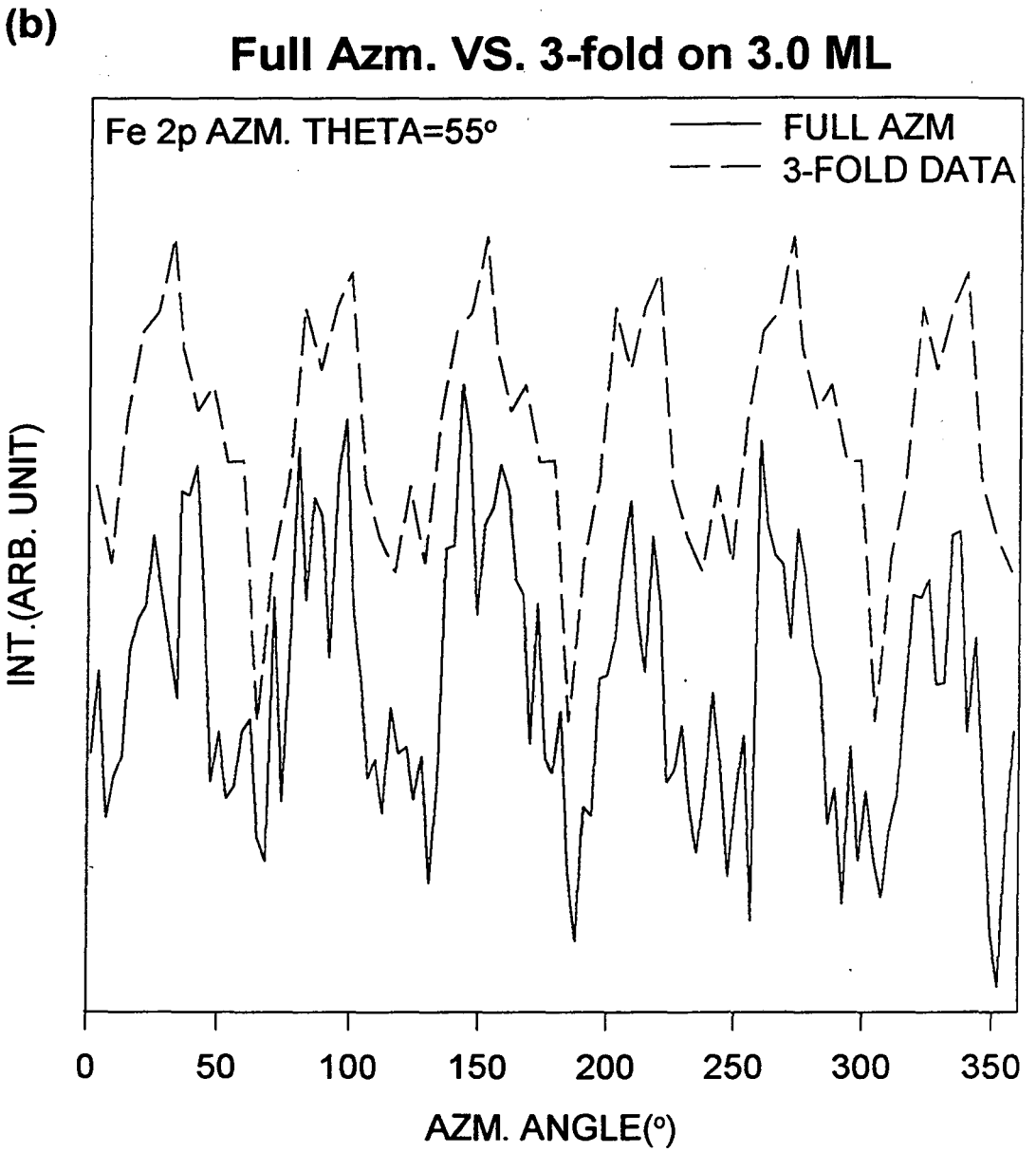

Figure G.1. (b) As (a), but for Fe $2p_{3/2}$, for which both curves are much closer to sixfold.

APPENDIX H

SINGLE SCATTERING VERSUS MULTIPLE SCATTERING

In deciding which structural model best fits our experimental data for a 3.0 ML film of iron oxide on Pt(111), we have also assessed the possible effects of multiple scattering in our theoretical analysis by carrying out simulations of photoelectron diffraction patterns for a test case within both a single scattering cluster (SSC) model and a multiple scattering cluster (MSC) model. The MSC program was that developed by Kaduwela et al. (ref. [22] in Chapter 4). The test case considered was the fully reconstructed structure for Fe_3O_4 determined by LEED (ref. [12] in Chapter 4, structure model (2) for the Fe_3O_4 cases in Chapter 4). Because of the very time consuming nature of the MSC calculations, particularly in view of the many types of emitters involved, only two azimuthal scans instead of full 2π XPD patterns were calculated in multiple scattering, one for Fe emission at a polar angle of 38° and one for O emission at a polar angle of 34° . These are polar angles for which strong forward scattering and other peaks are present for each case, and one might thus expect more pronounced multiple scattering effects to arise. The MSC calculations were done over only one third of the full azimuthal angles to reduce the cluster size, and the final full azimuthal data were obtained by exploiting threefold data folding and then averaging over two domain structures with a 180° rotation between them, as described in Chapter 3. These results are shown in Figs. H.1 (Fe emission) and H.2 (O emission) along with the SSC results and experimental data. For both Fe and O, both the SSC and MSC curves well reproduce the positions of the main peaks in the experimental data. However, the MSC results actually give a somewhat worse fit to the experimental data as far as predicting relative peak intensities. It is not clear why MSC does not provide a better description of our data than the less accurate SSC, but it could be due to the presence of some disorder in these thicker iron

oxide films (as suggested by the fuzzy LEED spots) and/or the multilayered structure of the oxide film (as seen in the STM image), that tends to reduce or distort any chains of forward scattering atoms and thus also multiple scattering.

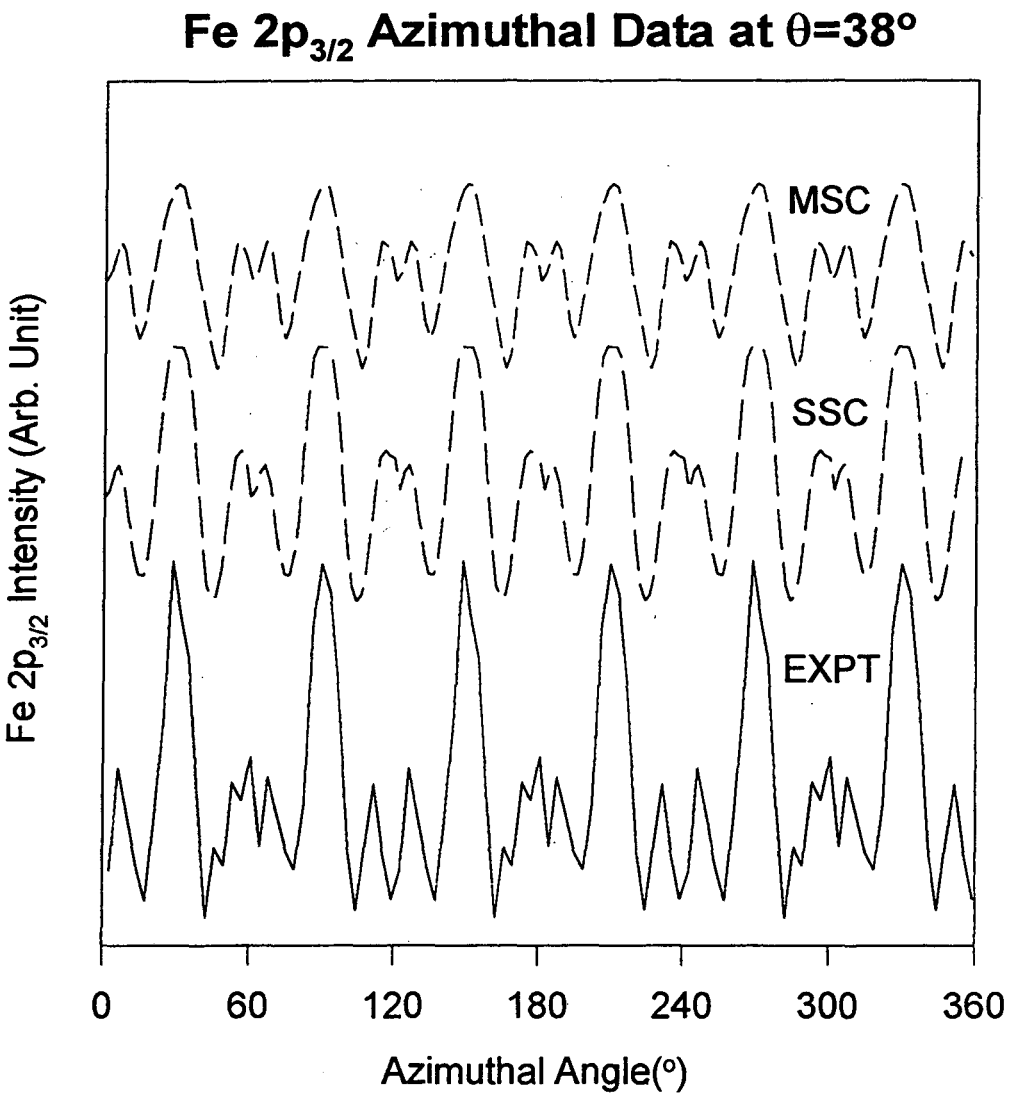

Figure H.1. SSC and MSC calculations for Fe $2p_{3/2}$ emission at a polar angle of 38° for the fully reconstructed Fe_3O_4 (111) LEED structure of ref. [12] in Chapter are compared to experiment for a 3.0 ML film of iron oxide.

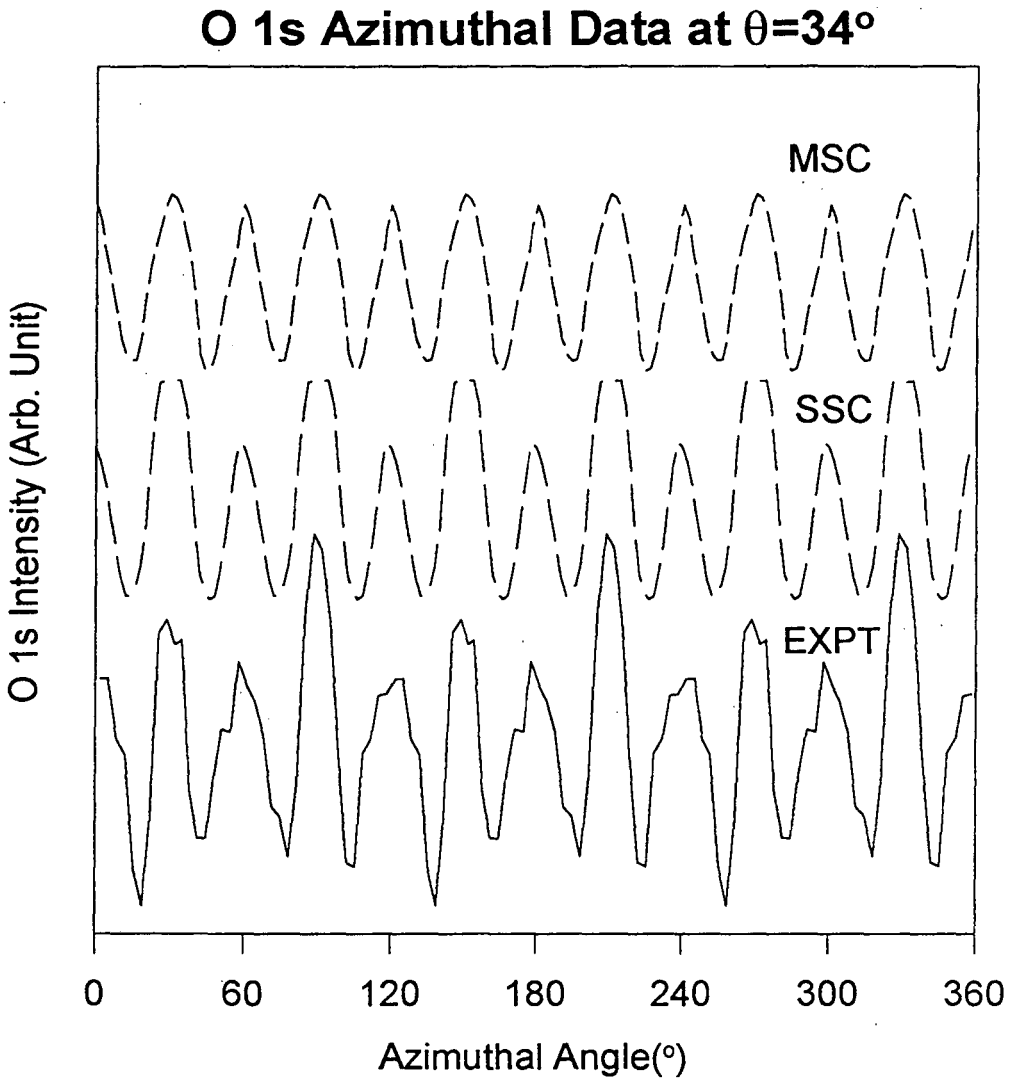

Figure H.2. As Fig. H.1, but for O 1s emission at a polar angle of 34°.

APPENDIX I

CLUSTERS FOR $Fe_2O_3(0001)$ AND $Fe_3O_4(111)$

The three dimensional cluster of $Fe_2O_3(0001)$ used to model XPD patterns is shown in Fig. I.1. Only 2 bilayers of Fe-O are shown with AB O stacking. Note Fe atoms are octahedrally coordinated and also that 1/3 ML of Fe atoms (compared to O) is absent in each layer to maintain the stoichiometry.

A similar view of the three dimensional cluster used to model $Fe_3O_4(111)$ has already been presented in Fig. 4.7. In Fig. I.2, we show in more detail the exact layer-by-layer makeup of this cluster over all of the Fe and O atoms present, and with all of the types of emitters (crossed) indicated. As noted previously, this cluster was meant to adequately span only 120° of azimuthal scanning, so that some scatterers beyond this region are included as well in each layer.

$Fe_2O_3(0001)$

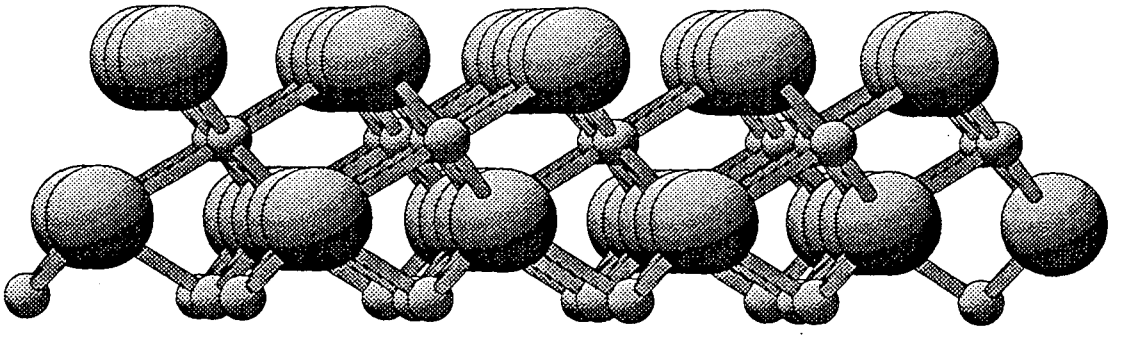

Figure I.1 The $Fe_2O_3(0001)$ atomic cluster with only 2 bilayers of Fe-O shown. The larger circles represent O atoms and smaller ones Fe atoms.

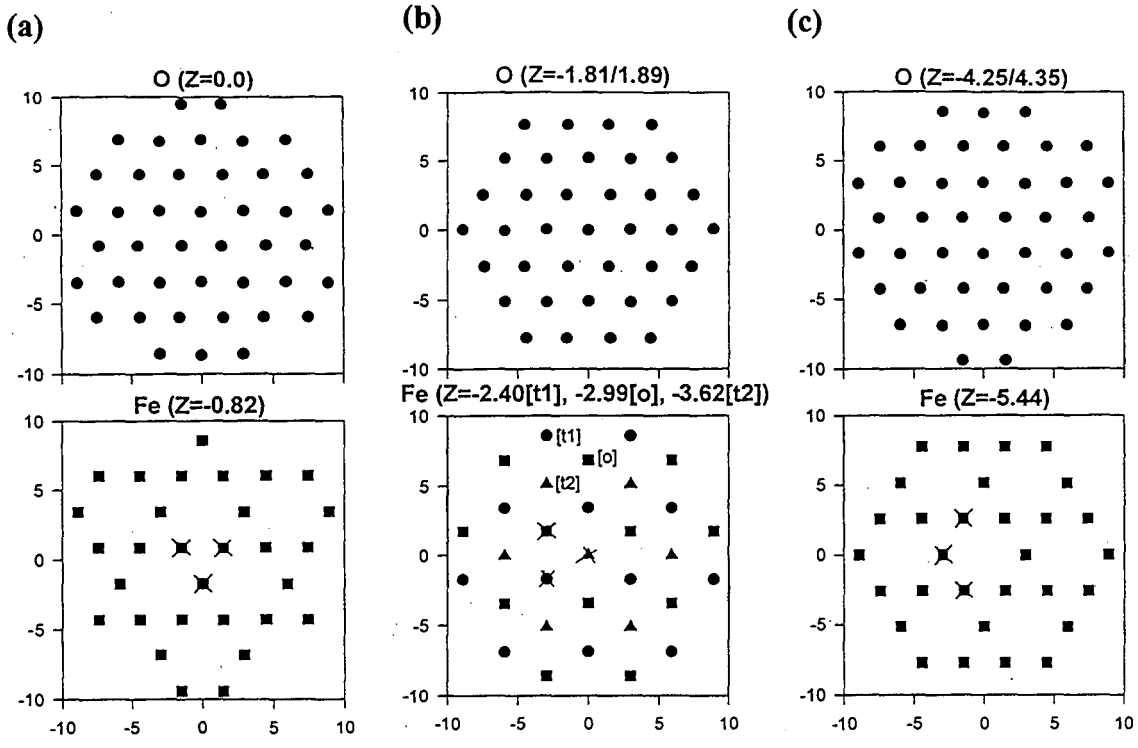

Figure I.2. The layer-by-layer makeup of the $Fe_3O_4(111)$ cluster used for our optimized structure: (a) topmost O-Fe bilayer, (b) middle O-Fe bilayer, and (c) bottom O-Fe bilayer. The Fe emitters (Fe emission) only are indicated in each layer and the interlayer distances are indicated as referenced to the surface layer.

APPENDIX J

R-FACTOR COMPARISON OF EXPERIMENT AND THEORY

The five R-factors (R1-R5) used to judge the goodness of fit between our experimental XPD data and theory are described in great detail elsewhere [J.1,2]. Biefly, these are factors are: R1--sum of absolute values of differences between experiment and theory, R2--sum of absolute values squared of differences between experiment and theory, R3--fraction of the data range over which experiment and theory have the same slope, R4--sum of absolute values of differences between the slopes of experiment and theory, and R5--sum of absolute values squared of differences between the slopes of experiment and theory. Intensities are normalized in a special way so as to be more applicable to XPD data [J.2]. In order to determine the best structural model for the case of 3.0 ML of iron oxide on Pt(111), we have carried out an R-factor analysis as summed over the full hemispherical XPD data for various structural models. The results of this analysis are summarized in Figs. J.1 (for Fe emission) and J.2 (for O emission), with the cases being listed from left to right in general order of decreasing R-factors. First, we note that all 5 R-factors generally show the same trends as structures are varied from left to right. The Fe R-factors are slightly more sensitive to changes in structure, with somewhat greater negative slopes in going from left to right.

Taking these results for Fe and O in their totality, we can first rule out the two Fe_2O_3 (0001) structural models 1 and 2, as these show a much worse fit to the data than the various structures of Fe_3O_4. Among the Fe_3O_4 structures, those with bulk Fe-O-Fe interlayer spacings (3 and 4) also show significantly reduced agreement with experiment, especially for Fe. Now comparing the structural model of a prior LEED I-V study [J.3] and our proposed model, the structures with a topmost 1/4 ML of Fe (5 and 7) have larger values for all five R-factors than the ones without this 1/4 ML of Fe (6 and 8) for

both structural models, suggesting an O-terminated structure. Between the structural models of 6 and 8, three out of five R-factors for the case of O emission favor our proposed structure (8), while there is no noticeable difference in the R-factors for Fe emission.

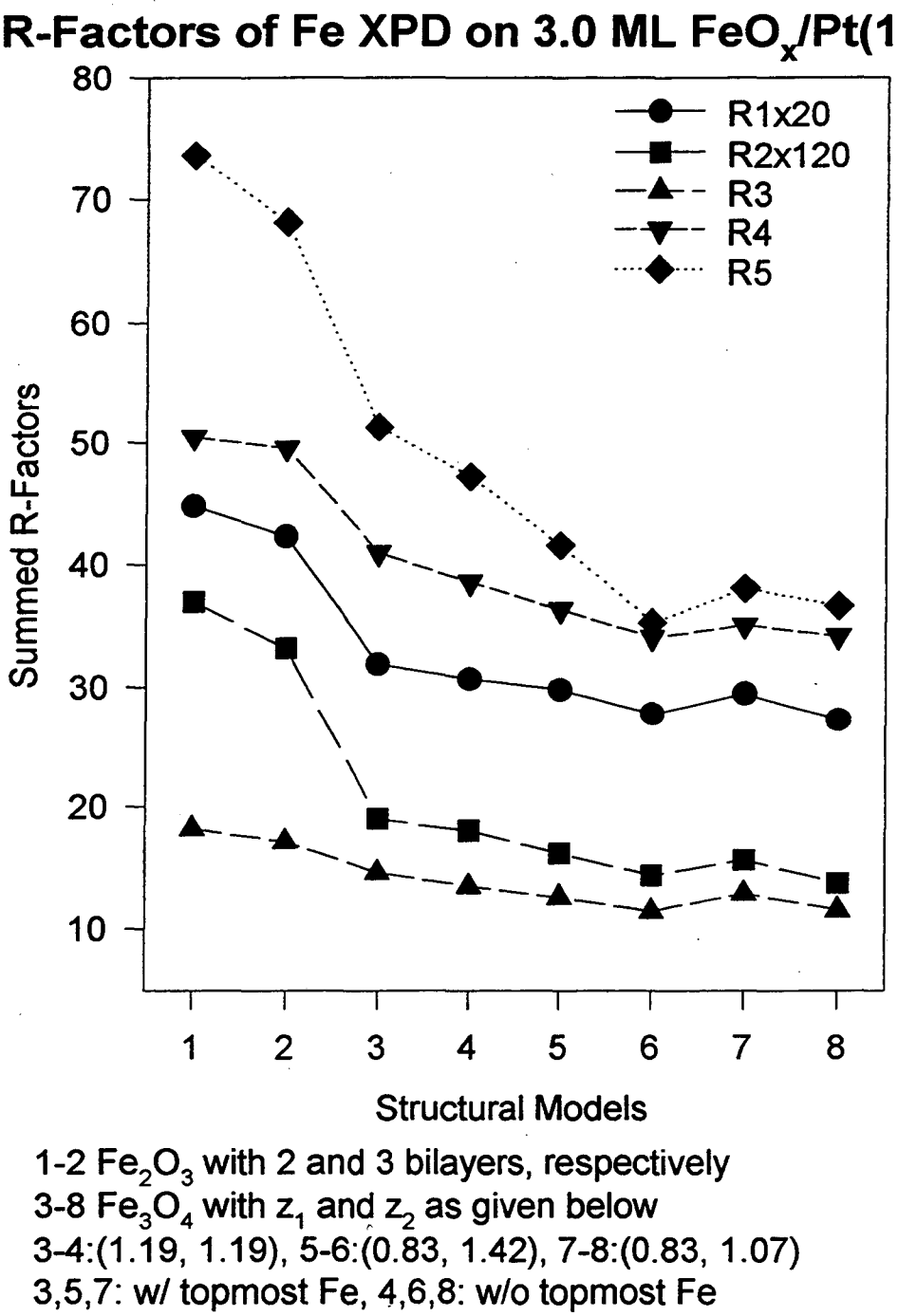

Figure J.1. R-factor analysis for the case of Fe $2p_{3/2}$ emission from 3.0 ML of iron oxide on Pt(111). The 8 structural models considered (see text for details) are in approximate order of decreasing R-factor.

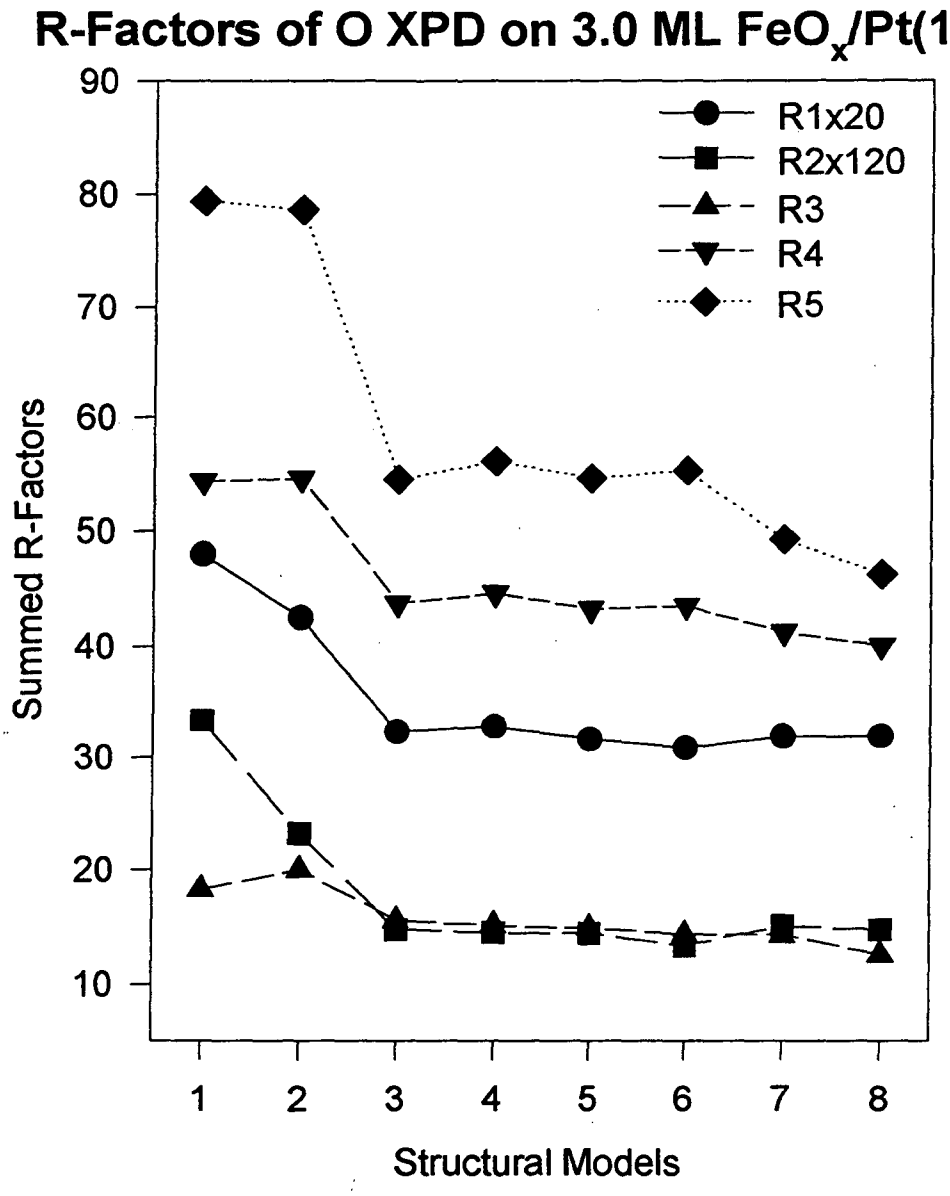

Figure J.2. As Fig. J-1, but for O 1s emission.

REFERENCES

[J.1] M.A. Van Hove, S.Y. Tong, and M.H. Elconin, Surf. Sci. 64, 85 (1977)

[J.2] R.S. Saiki, A.P. Kaduwela, M. Sagurton, J. Osterwalder, D.J. Friedman, C.S. Fadley, and C.R. Brundle, Surf. Sci. 282, 33 (1993)

[J.3] A. Barbieri, W. Weiss, M.A. Van Hove, and G.A. Sormojai, Surf. Sci. 302, 259 (1994)

LAWRENCE BERKELEY LABORATORY
UNIVERSITY OF CALIFORNIA
TECHNICAL INFORMATION DEPARTMENT
BERKELEY, CALIFORNIA 94720